INFORMATION TO USERS

This manuscript has been reproduced from the microfilm master. UMI films the text directly from the original or copy submitted. Thus, some thesis and dissertation copies are in typewriter face, while others may be from any type of computer printer.

The quality of this reproduction is dependent upon the quality of the copy submitted. Broken or indistinct print, colored or poor quality illustrations and photographs, print bleedthrough, substandard margins, and improper alignment can adversely affect reproduction.

In the unlikely event that the author did not send UMI a complete manuscript and there are missing pages, these will be noted. Also, if unauthorized copyright material had to be removed, a note will indicate the deletion.

Oversize materials (e.g., maps, drawings, charts) are reproduced by sectioning the original, beginning at the upper left-hand corner and continuing from left to right in equal sections with small overlaps. Each original is also photographed in one exposure and is included in reduced form at the back of the book.

Photographs included in the original manuscript have been reproduced xerographically in this copy. Higher quality 6" x 9" black and white photographic prints are available for any photographs or illustrations appearing in this copy for an additional charge. Contact UMI directly to order.

U·M·I

University Microfilms International
A Bell & Howell Information Company
300 North Zeeb Road, Ann Arbor, MI 48106-1346 USA
313/761-4700 800/521-0600

Reproduced with permission of the copyright owner. Further reproduction prohibited without permission.

Reproduced with permission of the copyright owner. Further reproduction prohibited without permission.

Order Number 9209703

Numerical modeling study of the circulation in the Gulf of Alaska

Bang, Inkweon, Ph.D.

University of Alaska Fairbanks, 1991

U·M·I
300 N. Zeeb Rd.
Ann Arbor, MI 48106

Reproduced with permission of the copyright owner. Further reproduction prohibited without permission.

Reproduced with permission of the copyright owner. Further reproduction prohibited without permission.

NUMERICAL MODELING STUDY

OF THE CIRCULATION

IN THE GULF OF ALASKA

A

THESIS

Presented to the Faculty

of the University of Alaska Fairbanks

in Partial Fulfillment of the Requirements

for the degree of

DOCTOR OF PHILOSOPHY

By

Inkweon Bang, B.S., M.S.

Fairbanks, Alaska

May 1991

Reproduced with permission of the copyright owner. Further reproduction prohibited without permission.

NUMERICAL MODELING STUDY

OF THE CIRCULATION

IN THE GULF OF ALASKA

By

Inkweon Bang

RECOMMENDED:

Advisory Committee Chair

Department Head

APPROVED:

Dean, School of Fisheries and Ocean Sciences

Dean of the Graduate School

5/1/91

Date

Reproduced with permission of the copyright owner. Further reproduction prohibited without permission.

Abstract

A series of numerical experiments are performed to simulate the Gulf of Alaska circulation and to examine the dynamical ocean response to the annual mean and seasonal forcing using a primitive equation model (Semtner 1974). The model domain encompasses the North Pacific north of 45° N and east of 180° and is surrounded by artificial walls in the south and west. Biharmonic diffusion is used in the interior to excite mesoscale eddies. A sponge layer with high Laplacian diffusion is incorporated near the western boundary. Horizontal resolution of 30′ × 20′ and 20 vertical levels are used to resolve the mesoscale topography and eddies. Wind stress computed from sea level atmospheric pressure and temperature and salinity data of Levitus (1982) are used.

A diagnostic model produces a circulation in the Gulf of Alaska which agrees with observed patterns. In a three-layer flat-bottom baroclinic model, baroclinic Rossby waves propagate at 0.8 *cm/sec* and it takes a decade for spin-up to be completed. Baroclinic models forced by the annual mean wind and thermohaline forcings show the generation of eddies by baroclinic instability. The eddies in the flat-bottom model have a period of 75 days and are interpreted as barotropic Rossby waves. In the model with topography, the period of dominant eddies is 3–4 years and they are interpreted as baroclinic Rossby waves. Anticyclonic eddies near Sitka show similar characteristics as the Sitka eddy. They propagate westward and cause meanders in the Alaska Stream near Kodiak Island. The abnormal shift of the Alaska gyre in 1981 is probably due to the presence of one of these anticyclonic eddies.

A flat-bottom model with seasonal forcing shows a large seasonal variability. When bottom topography is present, however, seasonal response is greatly reduced due to the dissipation of barotropic response by bottom topography. The seasonal baroclinic model shows a similar seasonal variability to the seasonal barotropic model indicating that the seasonal response is

Reproduced with permission of the copyright owner. Further reproduction prohibited without permission.

mainly barotropic. Eddies are also excited in the seasonal case and are almost identical to those of the annual mean case.

Reproduced with permission of the copyright owner. Further reproduction prohibited without permission.

Table of Contents

Abstract iii

List of Figures vii

List of Tables xiii

Dedication xiv

Acknowledgments xv

Chapter 1 INTRODUCTION 1

Section 1.1 Oceanography of the Gulf of Alaska 1

Section 1.2 Previous Modeling Studies 11

Section 1.3 Numerical Model 12

Section 1.4 Input Data 18

Chapter 2 DIAGNOSTIC MODEL 23

Section 2.1 Introduction 23

Section 2.2 Methods 24

Section 2.3 Results 26

Section 2.4 Discussion and conclusions 42

Chapter 3 SEASONAL BAROTROPIC MODEL 45

Section 3.1 Introduction 45

Section 3.2 Results 49

Section 3.3 Discussion and Conclusions 57

Reproduced with permission of the copyright owner. Further reproduction prohibited without permission.

Chapter 4 ANNUAL MEAN BAROCLINIC MODEL 59
Section 4.1 Introduction 59
Section 4.2 3-layer Case 63
Section 4.3 10-layer Case 70
Section 4.4 Topography Case 93
Section 4.5 Discussion and Conclusions 107
Chapter 5 SEASONAL BAROCLINIC MODEL 109
Section 5.1 10-layer Case 110
Section 5.2 Topography Case 122
Chapter 6 DISCUSSION AND CONCLUSIONS 132
Bibliography 140

Reproduced with permission of the copyright owner. Further reproduction prohibited without permission.

List of Figures

Figure 1.1 Major currents in the subarctic ocean (from Favorite et al. 1976). A, B, C, K, O, and S stand for Alaska gyre, Bering Sea gyre, California Current, Kuroshio, and Okhotsk Sea gyre, respectively. 2

Figure 1.2 Long-term mean Temperature distribution at 125 m (from Favorite et al. 1976). 3

Figure 1.3 Long-term mean Salinity distribution at 125 m (from Favorite et al. 1976). 4

Figure 1.4 Long-term mean Sigma-t distribution at 125 m (from Favorite et al. 1976). 5

Figure 1.5 Vertical sections of Long-term mean temperature, salinity, sigma-t and dissolved Oxygen distribution along 159° W (from Favorite et al. 1976). 6

Figure 1.6 Decay rates of the two-grid size motion by biharmonic (solid) and Laplacian (with marks) diffusion as a function of wavelength. 16

Figure 1.7 Bottom topography (in km) before (upper) and after (lower) smoothing. 19

Figure 1.8 Annual mean wind stress curl (upper) and seasonal range of the wind stress curl (lower). Unit is 1×10^{-8} dyn/cm^3. 21

Figure 1.9 Monthly mean wind stress curl (10^{-8} dyn/cm^3) in March, June, September, and December. Solid contour lines are for positive wind stress curl. 22

Figure 2.1 Basin-averaged kinetic energies (ergs/cm^3) of 1° diagnostic case (upper) and high-resolution case (lower). 27

Reproduced with permission of the copyright owner. Further reproduction prohibited without permission.

Figure 2.2 Contour plots of the stream function in: a) spring, b) summer, c) fall, d) winter, and e) annual mean and f) seasonal range of the stream function. 29

Figure 2.3 Particle tracks followed for one year show the fall diagnostic circulation in the upper 1000 m (the position is computed every 5 days). 33

Figure 2.4 Particle tracks followed for one year show the fall diagnostic circulation in 1000–2000 m (the position is computed every 5 days). . 35

Figure 2.5 Particle tracks followed for two years show the fall diagnostic circulation in 2000–3000 m (the position is computed every 10 days). . 36

Figure 2.6 Particle tracks followed for two years show the fall diagnostic circulation in 3000–4000 m (the position is computed every 10 days). . 37

Figure 2.7 Distribution of the sea levels (in cm) in summer defined by $\eta = p/\rho_0 g$, where ρ_0=1.02 gr/cm^3 and g=980.6 cm/sec^2. 39

Figure 2.8 Contour plots of the annual mean (upper) and the seasonal range (lower) of the stream function of the high–resolution diagnostic model. 41

Figure 3.1 Basin-averaged kinetic energy (ergs/cm^3) of the seasonal barotropic model and the average wind stress curl over the entire model domain (+). 50

Figure 3.2 Annual mean (upper) and seasonal range (lower) of the stream function. 51

Figure 3.3 Topography defined by number of layers. Seven monitoring points are marked by asterisk (VI: Vancouver Island, PP: Papa, CI: Cook Inlet, SE: Sitka Eddy, SM: Seamount, CK: Chirikof Island, and DS: Downstream) 53

Reproduced with permission of the copyright owner. Further reproduction prohibited without permission.

Figure 3.4 Contour plots of the stream functions at the middle of March, June, September, and December. 56

Figure 4.1 Time series of basin-averaged kinetic energy (ergs/cm^3). 64

Figure 4.2 Contour plot of the stream function at year 10 (upper) and the Sverdrup circulation (lower). 66

Figure 4.3 Velocity vector plots of top, middle, and bottom layers at year 10. . 67

Figure 4.4 Contour plot of the zonal velocity of the bottom layer along 48° 20′ N in longitude-time space. The chain-dotted line indicates the predicted location of baroclinic Rossby wave with a phase speed of 0.8 cm/sec. 68

Figure 4.5 Basin-averaged kinetic energy (ergs/cm^3). 72

Figure 4.6 Contour plots of the stream function at year 10 (upper) and of the perturbation field (lower) from the 2–year mean from 9–11. Contour interval of the bottom figure is 0.2 Sv. 73

Figure 4.7 Time series of the stream function (SF) at monitoring points for year 9–11 (see Figure 3.3 for the locations). 74

Figure 4.8 Time-longitude plot of perturbation stream function at 54° N. Dashed lines are 0.04 m/sec and contour interval is 0.2 Sv. 75

Figure 4.9 Meridional gradients of the total, relative, and planetary vorticities and vertically averaged zonal velocity U (upper). Phase speeds of a barotropic Rossby wave defined by (4.13) (lower). The thick bar indicates the average of C_0 over the distance which it spans. 79

Figure 4.10 Time coefficients and eigenvectors of the first two EOF modes. Zero contour lines are denoted by a thick solid line and other solid lines are for positive values and dashed lines are for negative values. . . 81

Reproduced with permission of the copyright owner. Further reproduction prohibited without permission.

Figure 4.11 Spectrum of stream function at five points along 54° N. 83

Figure 4.12 Distribution of spectrum of 80–day period. Note that contour intervals are not regular. 84

Figure 4.13 Phase (in degrees) of 80–day period signal relative to 54° N, 158° W. 85

Figure 4.14 Zonal distributions of the meridionally-averaged 2nd layer zonal velocity (U), EPE, EKE, the energy transfer terms, and dissipation terms. The averaging is done over 3 degrees from the northern boundary. 90

Figure 4.15 Time-depth plot of perturbation meridional velocity at 54° N, 156° 45′ W. Contour interval is 1 cm/sec. 92

Figure 4.16 Time series of the basin-averaged kinetic energy (ergs/cm^3). 94

Figure 4.17 Time series of stream function at seven monitoring points (see Figure 3.3 for the locations). 95

Figure 4.18 Demeaned and detrended stream function for year 16–25. Contour interval is 1 Sv and negative contour lines are denoted by dashed line. 96

Figure 4.19 Contour plot of the detrended stream function in time-longitude space along 57° 10′ N. Superimposed are lines of constant speed of 0.6 cm/sec. 97

Figure 4.20 Vertical profile of the mean σ_t in topography case and the σ_t of 3–layer case. 98

Figure 4.21 Contour plots of the detrended stream functions in time-longitude space along 50° N and in time-latitude space along 140° W. Superimposed are lines of constant speed; 0.3 cm/sec for time-latitude plot and 0.6 cm/sec for time-longitude plot. 101

Reproduced with permission of the copyright owner. Further reproduction prohibited without permission.

Figure 4.22 Time coefficients and eigenvectors of the first two EOF modes. Contour interval is 0.2. 103

Figure 4.23 Distributions of linear trend in zonal velocities over 1 year in year 23–24 at three depths. Contour intervals (CI) and depths are indicated in the upper left corner of each figure. Solid lines represent positive trends. 105

Figure 4.24 Distributions of trend in temperatures over 1 year in year 23–24 at three depths. Contour intervals (CI) and depths are indicated in the upper left corner of each figure. Solid lines represent positive trends. . . 106

Figure 5.1 Basin-averaged kinetic energies (ergs/cm^3) of 10–layer seasonal case (solid) and 10–layer annual mean case (dashed) from year 9–10 and monthly mean wind stress curl (+). 110

Figure 5.2 The energy balance of the total kinetic energy (upper: see text for details) and decomposition of T into the external ($T_e \equiv \partial \bar{E}/\partial t$) and internal ($T_i \equiv \partial E'/\partial t$) modes (lower). 113

Figure 5.3 The energy balance of the external (upper) and internal (lower) modes. 115

Figure 5.4 Contour plots of stream function in March, June, September, and December from year 9. 116

Figure 5.5 Time functions and eigenvectors of the first two EOF modes of year 9–11 before removal of the annual and semi-annual signals. 119

Figure 5.6 Time functions and eigenvectors of the first two EOF modes of year 9–11 after removal of the annual and semi-annual signals. 120

Reproduced with permission of the copyright owner. Further reproduction prohibited without permission.

Figure 5.7 Time functions and eigenvectors of the next two (3rd and 4th) EOF modes of year 9–11 after removal of the annual and semi-annual signals. 121

Figure 5.8 Basin-averaged kinetic energy (ergs/cm^3) of seasonal topography case. Kinetic energy of annual mean case is also shown for comparison. 123

Figure 5.9 Kinetic energy (ergs/cm^3) of the upper 1200 m of year 18–19 (+). Basin-averaged kinetic energy of the flat-bottom case is also shown for comparison (solid). 124

Figure 5.10 The energy balance of the total kinetic energy (upper) and decomposition of the time rate of change (T) into the external (T_e) and internal (T_i) modes (lower). 125

Figure 5.11 The energy balance of the external (upper) and internal (lower) modes. 126

Figure 5.12 The seasonal range of stream function from year 18–19. 128

Figure 5.13 Time series of raw stream function (left) and FFT-filtered (right) at monitoring points. 130

Figure 5.14 Contour plots of stream function in March, June, September, and December from year 18. 131

Reproduced with permission of the copyright owner. Further reproduction prohibited without permission.

List of Tables

Table 4.1 Temperature, salinity, sigma-t, layer thickness (d), and effective depth (h, see text for the definition) of each layer. 63

Table 4.2 Percentages explained by the first four EOF modes of stream function data of year 11. 82

Table 4.3 Basin-averaged values of the energy transfer and dissipation terms. 89

Table 4.4 Percentages explained by the first eight EOF modes of stream function from year 13 to 27. 102

Table 5.1 Percentages explained by the first three EOF modes of stream function from year 9 to 11. 117

Table 5.2 Percentages explained by the first eight EOF modes of the filtered stream function from year 9 to 11. 118

Reproduced with permission of the copyright owner. Further reproduction prohibited without permission.

Dedication

To my father

Reproduced with permission of the copyright owner. Further reproduction prohibited without permission.

Acknowledgments

This dissertation would have not been possible without the sacrifices made by my family both here in Alaska and in Korea. Especially, my wife, Kyung-Ae, and my offspring, Jae-Hoon and Klhee, have been truly patient with me during the long and dark Alaskan winters.

I would like to thank the members of my committee, Dr. David Fritts, Dr. Joe Niebauer, and Dr. Bill Reeburgh. I wish to extend special thanks to Dr. Tom Royer and my advisor Dr. Zygmunt Kowalik for their continued support, encouragement and guidance through my study and life. Discussions with Dr. Tom Weingartner and Dr. David Musgrave also improved the quality of this dissertation. There are numerous peoples who helped me with my study and life in Alaska. To all of them, I would like to give special thanks.

This work has been supported by the National Science Foundation grants OCE8608125 and OCE9012866. A generous offer of the computer time from San Diego Supercomputer Center was essential to the completion of this dissertation.

Reproduced with permission of the copyright owner. Further reproduction prohibited without permission.

Chapter 1 INTRODUCTION

The purpose of this work is to simulate and study large scale circulation and mesoscale eddies in the Gulf of Alaska using a primitive equation, high resolution, three dimensional and time dependent numerical model (Bryan 1969; Semtner 1974; Cox 1984). In this chapter, the general oceanography of the Gulf of Alaska, the numerical model to be used and problems to be addressed are described.

Section 1.1 Oceanography of the Gulf of Alaska

The Gulf of Alaska contains the eastern part of the North Pacific subarctic gyre, which, in turn, is a part of the North Pacific subarctic/subtropical circulation system. The subarctic boundary, which separates the North Pacific subarctic gyre from the subtropical gyre, lies at about 40° N (Figure 1.1). The Subarctic Current is formed near the Asia, flows eastward and divides into the Alaska Current and the California Current near the west coast of North America. The northward flowing Alaska Current becomes a narrow and swift western boundary current known as the Alaska Stream as it turns to the southwest near Kodiak Island. Thomson (1972) showed that the β-effect is sufficiently large for the Alaska Stream to be a western boundary current based on the analysis of vorticity balance in a curvilinear coordinate system. The Alaska Stream flows southwestward along the Alaska Peninsula and the Aleutian Islands until a portion of it recirculates into the gulf and rejoins the eastward flowing Subarctic Current. The remainder of the Alaska Stream continues to the west or enters the Bering Sea through the Aleutian Island passes (Figure 1.1).

Figures 1.2—1.4 are adopted from Favorite *et al.* (1976) to show the large scale horizontal distributions of water properties in the near surface (at 125 *m*) of the Subarctic Pacific ocean. They are useful to trace flow paths and in fact are the basis of the above description of the

Reproduced with permission of the copyright owner. Further reproduction prohibited without permission.

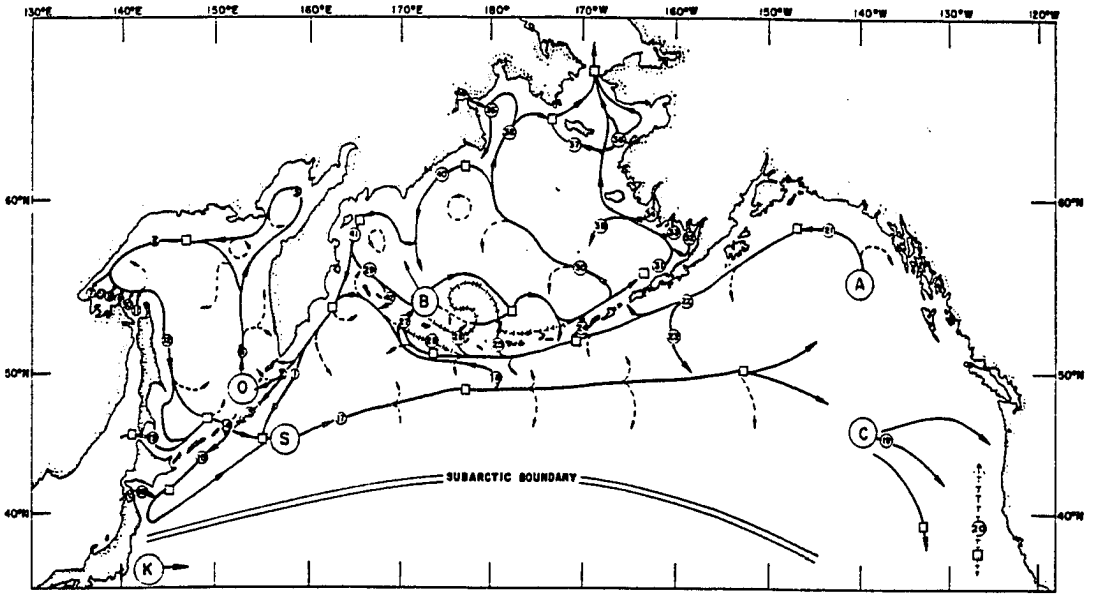

Figure 1.1 Major currents in the subarctic ocean (from Favorite *et al.* 1976). A, B, C, K, O, and S stand for Alaska gyre, Bering Sea gyre, California Current, Kuroshio, and Okhotsk Sea gyre, respectively.

current system. The nearly zonal isotherms in the open ocean, which show a gradual temperature decrease to the north, tend to follow the coastlines of North America such that high water temperatures are found near the coast and low temperatures at the center of the gulf (Figure 1.2).

Although near-surface salinity distribution is somewhat complicated in the gulf, low salinity waters are generally found along the coast of North America (north of 57° N) and Aleutian Islands to the 170° W (Figure 1.3). High salinity waters are found at the center of the gulf and also in the upwelling regions near Vancouver Island and along the Washington coast. Low salinities are occasionally seen seaward of this upwelling region (150° W-130° W south of 50° N). The near-surface distribution of sigma-t reflects high temperatures and low salinities near the coast and low temperatures and high salinities at the center of the gulf (Figure 1.4).

Reproduced with permission of the copyright owner. Further reproduction prohibited without permission.

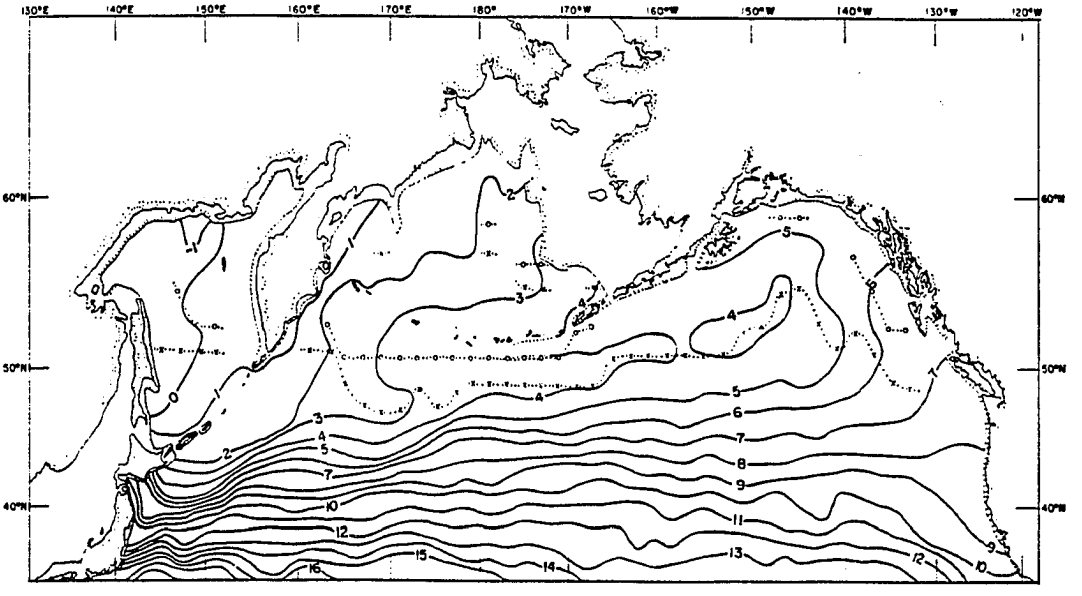

Figure 1.2 Long-term mean Temperature distribution at 125 m (from Favorite *et al.* 1976).

Therefore, high densities at the center are surrounded by low density waters in the south, east and north with the exception of the coastal upwelling region south of 50° N where the density is high. In the western gulf, the 26.4 isopycnal surrounds the center of the gulf. However, in other directions it is not closed and extends to the Bering Sea as well as to the western subarctic gyre (Figure 1.4).

The meridional cross sections of temperature, salinity, sigma-t, dissolved oxygen along the 159° W (Figure 1.5) show the vertical structure in and southwest of the gulf. A doming of low temperature, high salinity, high density, and low dissolved oxygen water (around 50° N at this longitude) is a characteristic feature of the central gulf. The isopycnals slope downward from about 50° N both to the north and south, thus supporting a westward flow to the north (Alaska Stream) and a broad eastward flow to the south (Subarctic Current). The subarctic boundary

Reproduced with permission of the copyright owner. Further reproduction prohibited without permission.

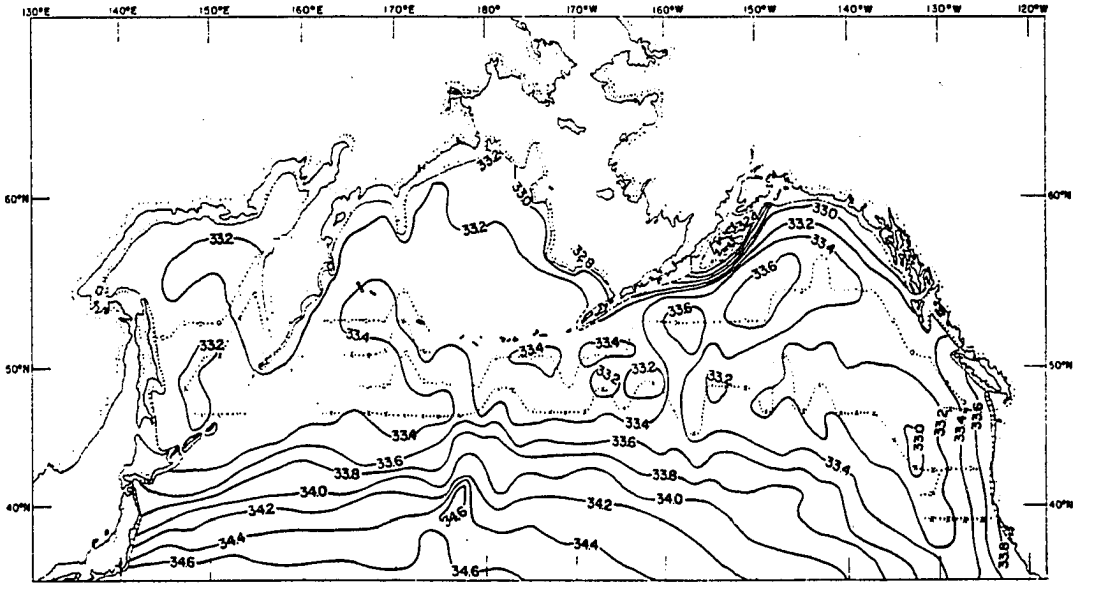

Figure 1.3 Long-term mean Salinity distribution at 125 m (from Favorite *et al.* 1976).

is located near 40° N as defined by the nearly vertical 34 psu isohaline in the upper layer. Subarctic water is characterized by an intermediate salinity minimum and is seen to extend southward at about 500 *m* depth.

The major atmospheric systems which govern the wind patterns in the Gulf of Alaska are the Aleutian Low and the Eastern Pacific High (Favorite *et al.* 1976). The Aleutian Low dominates from October through April and the Pacific High reaches its maximum in July covering all of the gulf. The annual mean position of boundary between Aleutian Low and Pacific High lies from about 50° N in the east to 35° N near Japan so that the annual mean wind-driven circulation is primarily influenced by the Aleutian Low. The Aleutian Low induces upwelling in the interior of the gulf and a southerly wind along the coast of North America and an easterly wind in the northern gulf. This alongshore wind advects the offshore water to

Reproduced with permission of the copyright owner. Further reproduction prohibited without permission.

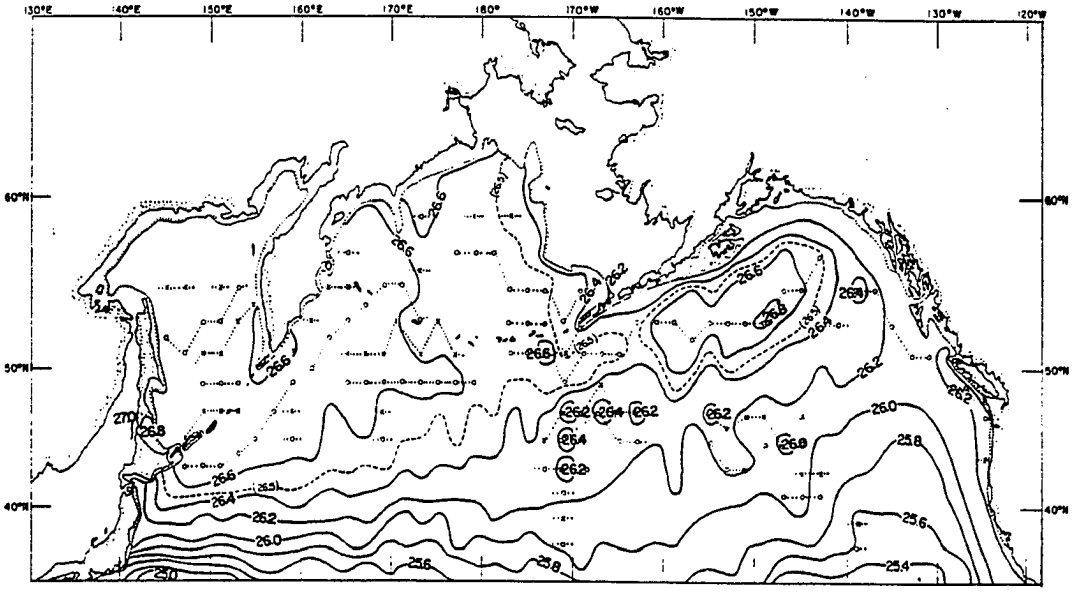

Figure 1.4 Long-term mean Sigma-t distribution at 125 m (from Favorite *et al.* 1976).

the coast resulting in downwelling there.

The upwelling in the interior of the gulf induced by the positive wind stress curl of the Aleutian Low causes a net advection of the water column to the north according to the Sverdrup theory. Along the western boundary the Alaska Stream carries the advected waters southwestward along the Alaska Peninsula and the Aleutian Islands, balancing the northward transport in the interior. Along the path of the Alaska Stream, recirculation of water into the interior gulf occurs and there is exchange of waters with the Bering Sea through passes along the Aleutian Islands. According to Favorite *et al.* (1976), two recirculation regions (170° W and 160° W) east of 180° are present in the surface and one (170° W) in the intermediate layer. Reed (1980) observed recirculation of the drifting buoys around 165° W, 158° W in 1978. A theoretical explanation of the recirculation is given by Thomson (1972) and he

Reproduced with permission of the copyright owner. Further reproduction prohibited without permission.

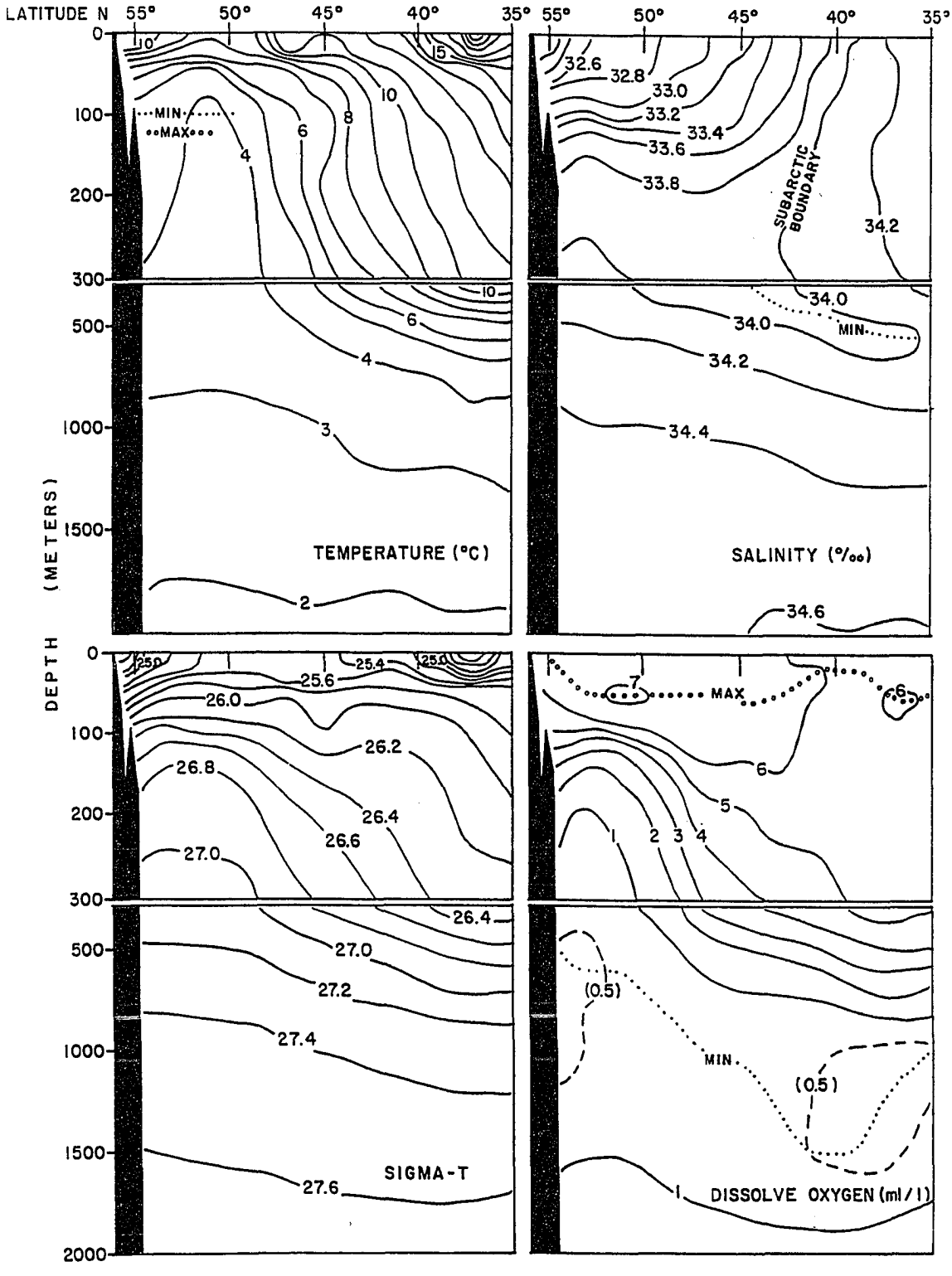

Figure 1.5 Vertical sections of Long-term mean temperature, salinity, sigma-t and dissolved Oxygen distribution along 159° W (from Favorite *et al.* 1976).

Reproduced with permission of the copyright owner. Further reproduction prohibited without permission.

linked recirculation to the orientation of Aleutian Islands along which Alaska Stream flows; the recirculation occurs where the advection of planetary vorticity no longer balances dissipation of relative vorticity as the Aleutian Islands becomes zonally oriented. Thomson (1972) also mentioned the possible role of passages as sources/sinks of vorticity to the Alaska Stream thus affecting the location of the recirculation.

Seasonal Circulation

Seasonal migration of the Aleutian Low and Pacific High causes a large seasonal fluctuation in the wind stress pattern in the gulf. Spatial distributions of the long-term monthly mean wind stress curl averaged from 1946 to 1988 (Figure 1.9) show the large seasonal cycle in the gulf. In winter the Aleutian Low is strong and the total wind-driven transports into the gulf reach about 20 Sv. In summer the Pacific High dominates and the transport is only 5 Sv (Reed *et al.* 1980). Musgrave *et al.* (1990) also report an expected seasonal transport variation of about 40 Sv near Cook Inlet based on the geostrophic current from the wind stress curl. It is surprising therefore that the circulation pattern remains almost constant despite large fluctuations in the atmospheric conditions in the gulf (Favorite *et al.* 1976). Reed *et al.* (1980) found no clear evidence of seasonal cycle in the transport of the Alaska Stream (Reed 1968) and sea level (Reid and Mantyla 1976) while Royer (1981) estimated the seasonal variation in the transport of the Alaska Stream near Kodiak Island to be about 13 % of the mean transport. An explanation of this meager seasonal variation in the gulf is one of the objectives of this thesis

Closely related with the seasonal variation of the Alaska Stream is interannual variability. Most famous interannual variability is an occasional shift of the Alaska Gyre which was observed in the summers of 1958 and 1981 (Reed 1984; Royer and Emery 1987). Reed (1984) suggested that the anomalous conditions were the result of unusually weak wind stress forcing over the Gulf region in the three months or so prior to the time of observations. Cummins (1989)

Reproduced with permission of the copyright owner. Further reproduction prohibited without permission.

agreed with Reed (1984) by noticing the seasonal east-west shift of gyre in his numerical results. Royer and Emery (1987) disputed this explanation and suggested an interaction of the eastward flowing North Pacific Current (Subarctic Current) with a group of seamounts near 51° N and 145° W as an alternative. According to Royer and Emery (1987) the shift of gyre occurs when the North Pacific Current flows far north of its normal position and is deflected by the seamounts resulting in the westward shift of Alaska Current.

Mesoscale Activity

Large variations in the flow of the Alaska Stream are observed frequently: for example, the transport relative to 1500 *db* at about 176° W ranges from 5 Sv to 14 Sv according to Favorite *et al.* (1976). There have been observations of an offshore shift of Alaska Stream from its normal position. For example, 185 km shift occurred at 155° W in winter 1962 and 280 km shift at 162° and 155° W in February and March 1967 and counter currents formed inshore at both times (Favorite *et al.* 1976). Reed *et al.* (1980) mentioned possible meanders and changes in the coastal current as an explanation for the variability in the Alaska Stream and recognized the need of a nonlinear model with stratification, topography, and β-effect.

Another possible cause of the circulation changes are mesoscale eddies. Ocean eddies have dominant temporal scales of weeks to months and spatial scales of tens to hundreds of kilometers. They commonly include a variety of variable flows such as meandering and filamenting of intense currents, semi-attached and cast-off rings, vortices, planetary waves, topography waves and wakes (Robinson 1983). A well-documented feature in the Gulf of Alaska is an eddy observed frequently offshore of Sitka at about 138° W, 57° N. Tabata (1982) described this eddy using 1954-1967 hydrographic data and the eddy was also detected with drifting buoys (Kirwan *et al.* 1978). The feature known as the Sitka eddy is about 200 to 300 km in horizontal diameter and extends to at least 2000 m depth and has a transport of 5-8 Sv.

Reproduced with permission of the copyright owner. Further reproduction prohibited without permission.

It propagates westward more than 1.5 *km/day* and persists 10-17 months. An anticyclonic eddy northwest of Sitka eddy and three cyclonic eddies along 55° N were also observed in February of 1967 by Roden (1969).

As an explanation of Sitka eddy Willmott and Mysak (1980) succeeded in producing an eddy-like structure from the reflection of a very low frequency Rossby wave by coastline. Tabata (1982) argued that topography should play an important role in the recurrence of Sitka eddy at the same location. In Cummins and Mysak (1988) an eddy appears at about the same location and they attributed the baroclinic instability of the Alaska Current for a generating mechanism.

Observations of long-period baroclinic Rossby waves were made by White and Tabata (1987). They used anomalies in the depth of σ_t=26.8 surface along Papa Line and concluded that these waves with a period of 1–5 years are correlated to ENSO events and driven by anomalous wind stress associated with teleconnetions in the atmosphere. They also mentioned wind resonance as a possible explanation (White 1982) for the amplification of signal westward.

Numerical modeling will be employed to explain the following physical features in the Gulf of Alaska.

1. To understand and explain why there is little to no seasonal variability in the transport of the Alaska Stream under one of the largest seasonal fluctuation in the atmospheric condition in the world,
2. To examine the suggestion of Cummins (1989) that the abnormal shift of the Alaska gyre is the amplification of the seasonal shift of gyre. The suggestion of Royer and Emery (1987) cannot be examined because it involves the shift of position of the Subarctic Current which may originate from farther west than the model domain of this thesis covers, and
3. To excite mesoscale eddies and study their roles in the circulation of the Gulf of Alaska.

Reproduced with permission of the copyright owner. Further reproduction prohibited without permission.

To achieve these goals, a series of numerical experiments have been carried out. The numerical models used vary in complexity ranging from a diagnostic model to a prognostic, time dependent model with bottom topography. In Chapter 2, a diagnostic model is used to reproduce a circulation expected from observed density structure in the Gulf of Alaska. Integrations are done over each season and results are discussed in terms of annual mean circulation and seasonal variability.

In Chapter 3, the Gulf of Alaska is assumed homogeneous and effect of topography on the oceanic response to seasonal wind forcing is discussed. This barotropic model follows a theory of Anderson and Corry (1985a) which predicts that the seasonal response of the western boundary current in middle and high latitudes is mainly barotropic.

In Chapter 4, stratification is introduced into the model so that baroclinic motion can be excited. The first case is a three-layer flat-bottom model and is forced by wind stress only. Next two cases include the thermohaline forcing and the number of vertical layers is increased to 10 in a flat-bottom case and 20 in a topography case.

In Chapter 5, the same model configurations (flat-bottom and topography cases) as in Chapter 4 are used to study the ocean response to the seasonal forcing. Discussions and conclusions are given in Chapter 6.

Reproduced with permission of the copyright owner. Further reproduction prohibited without permission.

Section 1.2 Previous Modeling Studies

There have been several numerical modeling efforts to simulate the circulation in the Gulf of Alaska. Most recently, Cummins and Mysak (1988) and Cummins (1989) used an eddy-resolving quasi-geostrophic (QG) numerical model for the climatological mean and seasonal cycle circulation studies. They found that bathymetry plays an important role in the suppression of the seasonal variation in the volume transport of the Alaska Stream. Cummins (1989) also remarked that the abnormal shift of the Alaska gyre might result from variations in the integrated strength of the wind stress curl over the gulf.

The Gulf of Alaska was included in some numerical modeling studies of the North Pacific (Huang 1978, 1979; Hsieh 1987), but their coarse resolution made it difficult to comprehend the full dynamical effects of the Aleutian Islands and bottom topography on the Alaska gyre. Hsieh (1987) used an $1° \times 1° \times 6$ (vertical levels) primitive equation model to study the seasonal circulation in the North Pacific and yielded unrealistic seasonal variations probably as a result of low vertical resolution.

Although the results by Cummins and Mysak (1988) and Cummins (1989) are impressive, QG models have limitations. QG theory assumes that the Rossby number, bottom relief, and the displacement of the interface are small. Furthermore, no thermohaline forcing is possible in the QG model. In this thesis, a high resolution primitive equation model is used which does not assume any of the approximations used in the QG model and is capable of thermohaline forcing. Unlike Hsieh (1987), as many vertical layers as possible will be employed to include the effect of bottom topography.

Reproduced with permission of the copyright owner. Further reproduction prohibited without permission.

Section 1.3 Numerical Model

Semtner's version (1974) of Bryan's (1969) primitive equation model is used for this study. This model adopts hydrostatic, Boussinesq, and rigid-lid approximations in spherical coordinate system. The horizontal momentum equations for the zonal (λ) and meridional (ϕ) directions are

$$\begin{aligned}
\frac{\partial u}{\partial t} + Lu - \frac{uv\tan\phi}{a} - fv &= -\frac{1}{\rho_0 a\cos\phi}\frac{\partial p}{\partial \lambda} + \kappa\frac{\partial^2 u}{\partial z^2} \\
&\quad + \begin{cases} A_M\left\{\nabla^2 u + \frac{(1-\tan^2\phi)u}{a} - \frac{2\sin\phi}{a^2\cos^2\phi}\frac{\partial v}{\partial\lambda}\right\} \\ B_M\nabla^4 u \end{cases} \\
\frac{\partial v}{\partial t} + Lv + \frac{u^2\tan\phi}{a} + fu &= -\frac{1}{\rho_0 a}\frac{\partial p}{\partial \phi} + \kappa\frac{\partial^2 v}{\partial z^2} \\
&\quad + \begin{cases} A_M\left\{\nabla^2 v + \frac{(1-\tan^2\phi)v}{a} + \frac{2\sin\phi}{a^2\cos^2\phi}\frac{\partial u}{\partial\lambda}\right\} \\ B_M\nabla^4 v. \end{cases}
\end{aligned} \tag{1.1}$$

The hydrostatic approximation is

$$\frac{\partial p}{\partial z} = -\rho g. \tag{1.2}$$

The continuity equation is

$$\frac{1}{a\cos\phi}\frac{\partial u}{\partial\lambda} + \frac{1}{a\cos\phi}\frac{\partial}{\partial\phi}(v\cos\phi) + \frac{\partial w}{\partial z} = 0. \tag{1.3}$$

The equations of temperature and salinity are

$$\begin{aligned}
\frac{\partial T}{\partial t} + LT &= \kappa\frac{\partial^2 T}{\partial z^2} + \begin{cases} A_H\nabla^2 T \\ B_H\nabla^4 T, \end{cases} \\
\frac{\partial S}{\partial t} + LS &= \kappa\frac{\partial^2 S}{\partial z^2} + \begin{cases} A_H\nabla^2 S \\ B_H\nabla^4 S. \end{cases}
\end{aligned} \tag{1.4}$$

The equation of state is

$$\rho = \rho(T, S, p). \tag{1.5}$$

z is positive upwards. u, v, and w are velocities in the λ, ϕ, and z directions, respectively and T is water temperature, S is salinity, p is pressure, g is acceleration due to gravity, a is the radius

Reproduced with permission of the copyright owner. Further reproduction prohibited without permission.

of the earth, ρ_0 is mean water density. The Coriolis parameter is $f = 2\Omega \sin\phi$ where Ω is the angular speed of the earth rotation. The advection operator L is defined as

$$L(\sigma) = \frac{1}{a\cos\phi}\frac{\partial}{\partial\lambda}(u\sigma) + \frac{1}{a\cos\phi}\frac{\partial}{\partial\phi}(v\sigma\cos\phi) + \frac{\partial}{\partial z}(w\sigma). \tag{1.6}$$

The horizontal Laplacian operator is

$$\nabla^2\sigma = \frac{1}{a^2\cos^2\phi}\frac{\partial^2\sigma}{\partial\lambda^2} + \frac{1}{a^2\cos\phi^2}\frac{\partial}{\partial\phi}\left(\cos\phi\frac{\partial\sigma}{\partial\phi}\right). \tag{1.7}$$

and the biharmonic operator is

$$\nabla^4\sigma = \frac{1}{a^2\cos^2\phi}\frac{\partial^2}{\partial\lambda^2}\nabla^2\sigma + \frac{1}{a^2\cos\phi^2}\frac{\partial}{\partial\phi}\left(\cos\phi\frac{\partial}{\partial\phi}\nabla^2\sigma\right). \tag{1.8}$$

A and B are the horizontal eddy coefficients for the Laplacian and biharmonic diffusions, respectively and their subscripts H and M are, respectively, for the diffusion and momentum. For the vertical eddy coefficients (κ), different values are used in the diffusion and momentum equations. Details of the numerical formulation and methods of finding solutions are in Semtner (1974).

The boundary conditions of momentum at the ocean surface and bottom are

$$\begin{aligned} \rho_o\kappa\frac{\partial\vec{u}}{\partial z} &= \vec{\tau}_w, \ z = 0, \quad \text{and} \\ \rho_o\kappa\frac{\partial\vec{u}}{\partial z} &= \vec{\tau}_b, \ z = -H. \end{aligned} \tag{1.9}$$

where $\vec{\tau}_w$ and $\vec{\tau}_b$ are wind stress and bottom stress, respectively. A no flux boundary condition is used at the ocean surface and bottom for temperature and salinity, which is

$$\rho_o\kappa\frac{\partial(T,S)}{\partial z} = 0. \tag{1.10}$$

The thermohaline forcing is incorporated by the use of a robust-diagnostic method and explained more detail in section 4.3.

Reproduced with permission of the copyright owner. Further reproduction prohibited without permission.

Biharmonic friction (Cox 1984) is used for horizontal friction and diffusion to resolve eddies. Biharmonic friction has an advantage over Laplacian friction in that it dissipates small scale motions more quickly than large scale motions so that the frictional effects on the mesoscale eddies and large scale circulation can be much smaller while still maintaining computational stability (Pond and Pickard 1983). For this reason it is sometimes called 'scale-selective friction'.

A boundary condition of temperature and salinity with biharmonic diffusion is

$$\frac{\partial \sigma}{\partial n} = 0, \qquad \frac{\partial}{\partial n}\nabla^2 \sigma = 0, \tag{1.11}$$

where σ is either temperature or salinity and n is normal direction to the boundary. For the momentum, no-slip boundary condition is used, i.e.,

$$\vec{u} = 0, \qquad \nabla^2 \vec{u} = 0. \tag{1.12}$$

These conditions can be better understood by considering the simple one dimensional heat diffusion problem.

$$\frac{\partial \sigma}{\partial t} = -B\frac{\partial^4 \sigma}{\partial x^4}, \quad 0 \leq x \leq 1 \tag{1.13}$$

Here, x is an arbitrary horizontal direction and σ represents temperature when the boundary condition of (1.11) is considered. The total heat content in the domain will remain constant if the boundary condition (1.11) is correct. The integration of (1.13) in x over the domain is

$$\frac{\partial}{\partial t}\int_0^1 \sigma dx = -B\left[\frac{\partial^3 \sigma}{\partial x^3}\right]_{x=0}^{x=1} \tag{1.14}$$

and is zero by the second boundary condition of (1.11), i.e., the total heat content is conserved in time.

Reproduced with permission of the copyright owner. Further reproduction prohibited without permission.

Now, the steady-state solution of (1.13) is

$$\sigma = C_0 + C_1 x + C_2 x^2 + C_3 x^3 \tag{1.15}$$

where the coefficients are to be determined by the conservation principle (1.14) and the boundary condition (1.11). First, applying the second boundary condition of (1.11) leads to $C_3=0$ and the temperature would take a parabolic distribution if C_2 is not zero. This distribution is not natural in the absence of any heating/cooling and a more realistic distribution is a homogeneous distribution with no spatial gradient of temperature. The first condition of (1.11) makes $C_1=C_2=0$ and then C_0 is determined from the initial heat contents of the domain.

The situation for the momentum (σ is now velocity) is different from the temperature because there is a leakage of momentum through the boundaries ((1.14) is not zero so that there is a variation of total momentum in time) and one can expect no motion ($\sigma=0$) all over the domain as a steady-state solution. Again, it can be easily shown that application of the boundary condition (1.12) to the general solution of the steady-state (1.15) leads to no motion.

Semtner and Mintz (1977) used the following formula to compare the biharmonic coefficient to the Laplacian coefficient. This formula can be derived from dissipation rates of the smallest scale motion by two formulations.

$$B_M = -\frac{A_M \delta x^2}{4} \tag{1.16}$$

where δx is the grid size and a value of 20′ (37 km) is used. According to this formula -8 $\times$ 10^{19} is equivalent to Laplacian coefficient of 2.3 $\times$ 10^7. Figure 1.6 shows that the decay rates of the biharmonic diffusion decrease more rapidly with wavelength than those of the Laplacian diffusion. It also shows that a Laplacian coefficient of 2.5 $\times$ 10^7 has the same damping rate at about 70 km as the biharmonic coefficient of -8 $\times$ 10^{19} but the Laplacian damping is more than a order of magnitude larger than biharmonic damping at large scales ($\geq$ 400 km).

Reproduced with permission of the copyright owner. Further reproduction prohibited without permission.

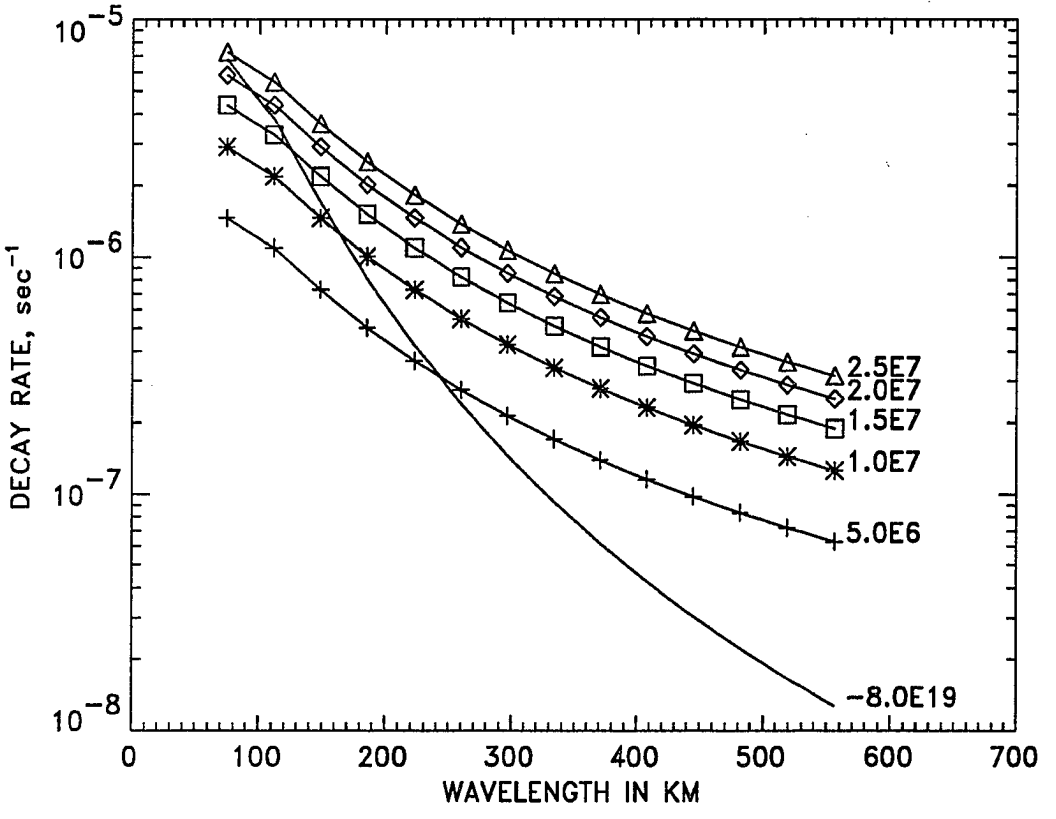

Figure 1.6 Decay rates of the two-grid size motion by biharmonic (solid) and Laplacian (with marks) diffusion as a function of wavelength.

Another comparison between the coefficients of the two diffusion schemes can be made in terms of the thickness of Munk's boundary layer (Pedlosky 1982) which is a dynamically important parameter for judging the friction effect. The width of the Munk layer is defined as $(A_M/\beta)^{1/3}$ for Laplacian friction and is modified to $(-B_M/\beta)^{1/5}$ for biharmonic friction. Here, β is the meridional gradient of f. 1.3 x 10^{-13} sec^{-1} cm^{-1} is used here. By equating these two expressions, one can obtain a relationship for a biharmonic coefficient in terms of the Laplacian coefficient as following;

$$B_M = -A_M^{5/3}\beta^{-2/3}. \tag{1.17}$$

Reproduced with permission of the copyright owner. Further reproduction prohibited without permission.

Then, a biharmonic coefficient of -8×10^{19} would have the same width of the Munk layer as a Laplacian coefficient of 6.1×10^{6}, which is about a quarter of the value by (1.16). So, (1.16) is too conservative in the comparison of the coefficients by two diffusion schemes and the biharmonic coefficient determined by (1.16) would produce much thinner Munk layer than the equivalent Laplacian coefficient. Consequently, the horizontal friction effect would be overestimated.

Resolution both in horizontal and vertical directions is important for successful computation. Since the objectives of this thesis include the generation of mesoscale eddies and the assessment of the effect of a mesoscale topography, a fine resolution in both horizontal and vertical directions is needed. On the other hand, as the resolution of the model becomes higher, it requires more computer time and storage space. A compromise would be made between the available resources and objectives. After careful consideration, 30′ (zonal) × 20′ (meridional) resolution with 20 vertical layers is adopted. The horizontal resolution is 31 km (at 55° N) × 37 km and is larger than 25 km used by Cummins and Mysak (1988). The model is run on the Cray Y-MP 8/864 of San Diego Supercomputer Center and it took about 100 minutes of service unit for one year integration of a baroclinic model with 1 hour timestep.

For the determination of density from temperature, salinity, and depth in world ocean circulation models, polynomial approximations to Knudsen formula (Fofonoff 1962) were employed to save the computer time. Two choices have been developed by Friedrich and Levitus (1972) and Bryan and Cox (1972). Since there is not any significant advantage of one approximation over the other, the Friedrich and Levitus (1972) technique is used because it was easier to incorporate into the model.

Reproduced with permission of the copyright owner. Further reproduction prohibited without permission.

Section 1.4 Input Data

Abrupt changes in depth, such as those found across a trench, can cause numerical instabilities in a primitive equation model (Ramming and Kowalik 1980; Killworth 1987). A certain amount of topographic smoothing is necessary therefore to ensure numerical stability, although some dynamics are lost. A smoothed depth distribution was obtained from 5′–interval depth data both in longitude and latitude. The raw data was smoothed by 9-point Shapiro filter (Shapiro 1970), subsampled every 30′ in longitude and 20′ in latitude, and smoothed once more by the same filter. The depth distributions before and after smoothing are shown in Figure 1.7. Seamounts and the Aleutian trench, which are considered dynamically important in the Gulf of Alaska, remain resolved with this resolution.

Forty three years (1946–1988) of monthly mean sea level atmospheric pressure of Fleet Numerical Oceanography Center were used for the computation of wind stress. Geostrophic winds were computed from derivatives of monthly mean sea level pressure using natural cubic spline interpolation (Cheney and Kincaid 1985). Wind direction was rotated 15° counter-clockwise and wind speed was reduced 30 % to compensate for the effect of friction (Willebrand 1978; Luick *et al.* 1987). Next, wind stress was computed by the bulk formula

$$\vec{\tau} = \rho_a C_d \vec{u}|u|, \tag{1.18}$$

where ρ_a is the air density, 1.225 kg/m^3 and u is the wind velocity in *m/sec*. Garratt's (1977) formula was used for drag coefficient.

$$C_d = (0.75 + 0.067|\vec{u}|) \times 10^{-3}. \tag{1.19}$$

Wind stress curl appears as a forcing term in the vorticity equation of the vertically integrated transport. Therefore, a wind-driven circulation can be understood more easily in

Reproduced with permission of the copyright owner. Further reproduction prohibited without permission.

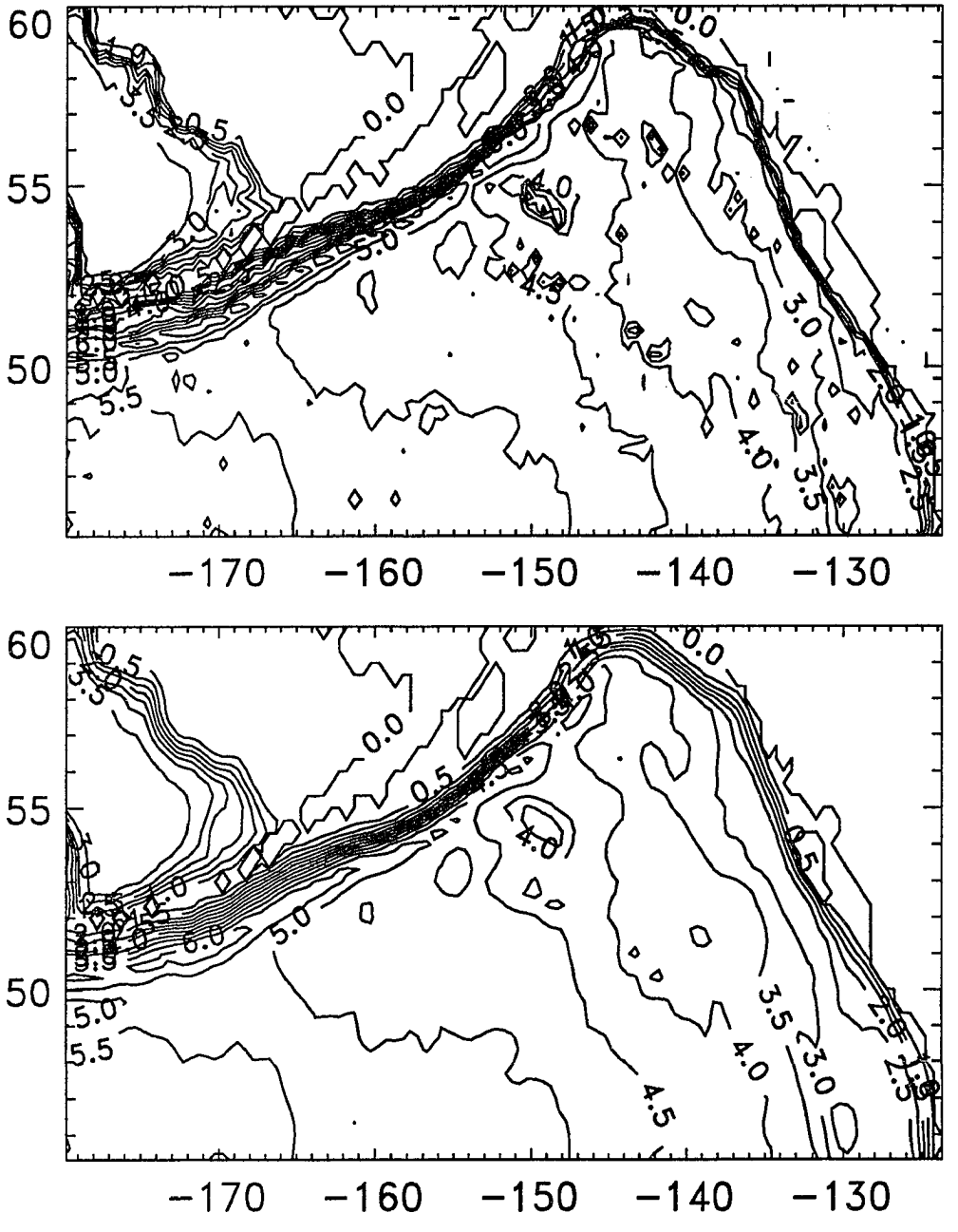

Figure 1.7 Bottom topography (in km) before (upper) and after (lower) smoothing.

Reproduced with permission of the copyright owner. Further reproduction prohibited without permission.

terms of the wind stress curl than the wind stress, although the latter is used to force the model ocean in the computation. For example, wind stress curl determines the sense of rotation of the wind-driven gyre (positive wind stress curl establishes a cyclonic gyre and vice versa) and can be used to estimate the transport using the Sverdrup balance. Wind stress curl is computed by the central finite difference formulation from the wind stress and the annual mean and the seasonal range of wind stress curl are shown in Figure 1.8. Maximum positive wind stress curl is about 3×10^{-8} dyn/cm^3 and is located at 58° N, 140° W. It is northeastward of the position of the maximum from Willebrand (1978) and the maximum value is higher than the maximum in Willebrand (1978). In general, the wind stress curl used in this thesis is higher in the region north of 55° N and lower to the south of 55° N compared to Willebrand (1978). Interestingly, the seasonal variation of the wind stress curl is large in the northeast corner of the gulf where a large annual mean wind stress curl is also found. Monthly mean wind stress curl for selected months (Figure 1.9) also illustrates the temporal variabilities of the wind stress curl.

Temperature and salinity data of Levitus (1982) were used as the observation data. This dataset includes all observations by XBT, CTD, and Nansen casts through the first quarter of 1977 and annual mean and seasonal means are compiled at 1° resolution. The annual mean data are defined at 33 standard oceanographic depths from the sea surface to 6000 *m*, but the seasonal data are defined only at the upper 24 standard depths.

Reproduced with permission of the copyright owner. Further reproduction prohibited without permission.

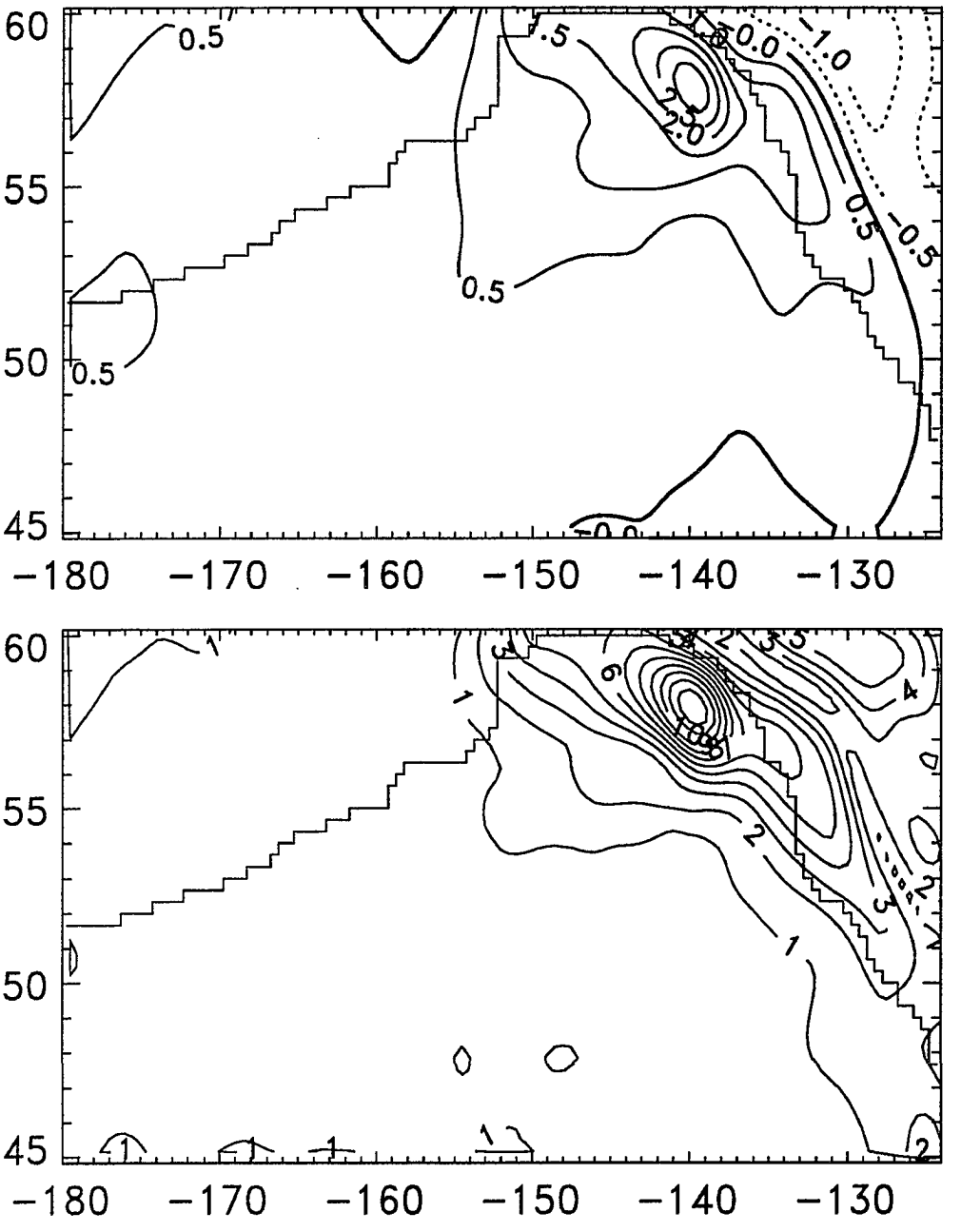

Figure 1.8 Annual mean wind stress curl (upper) and seasonal range of the wind stress curl (lower). Unit is 1 × 10^{-8} *dyn/cm*^{3}.

Reproduced with permission of the copyright owner. Further reproduction prohibited without permission.

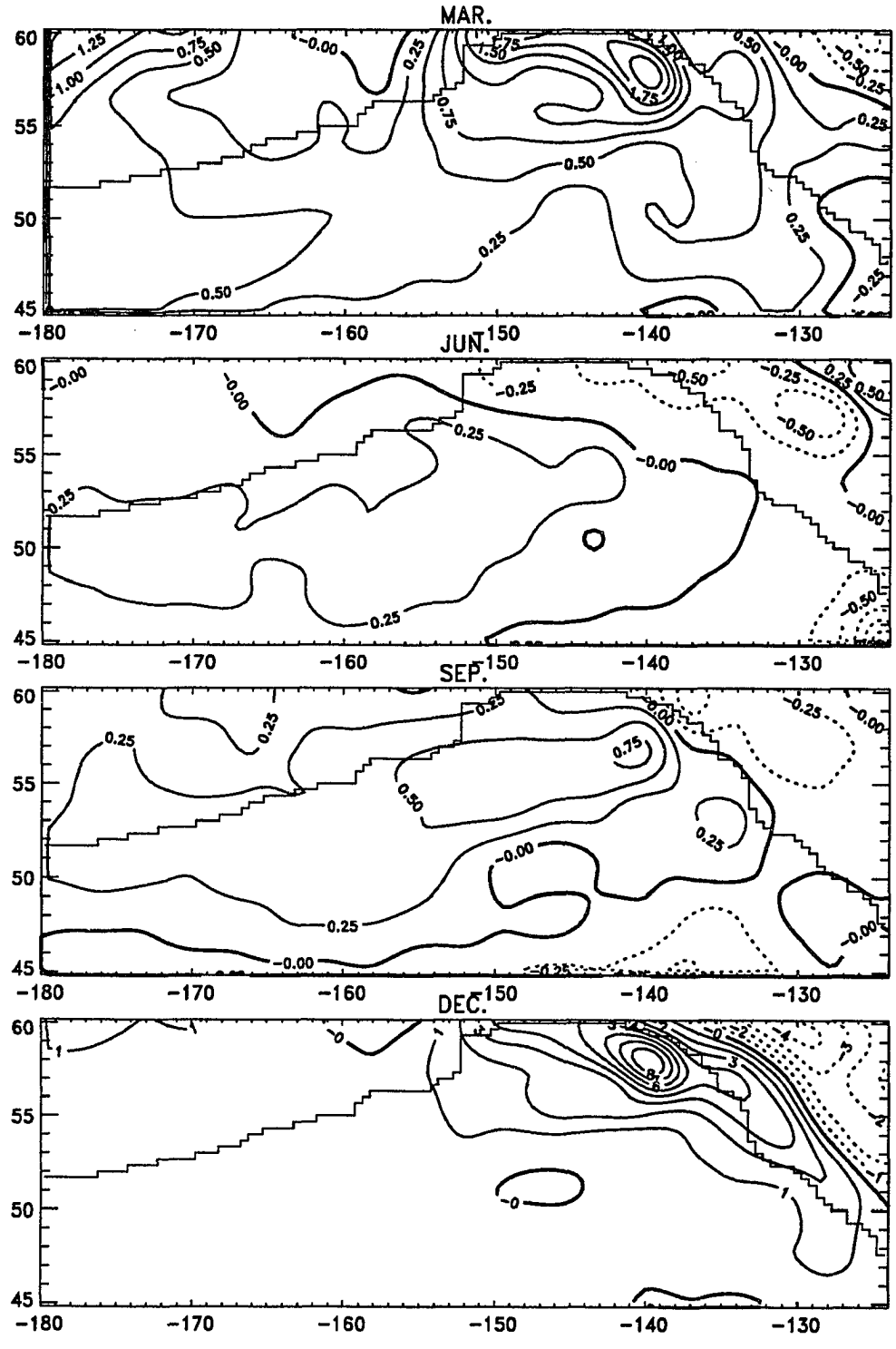

Figure 1.9 Monthly mean wind stress curl (10^{-8} *dyn/cm*^{3}) in March, June, September, and December. Solid contour lines are for positive wind stress curl.

Reproduced with permission of the copyright owner. Further reproduction prohibited without permission.

Chapter 2 DIAGNOSTIC MODEL

Section 2.1 Introduction

From a given density field, a current field can be constructed by several methods. The traditional dynamic method, although quite simple in dynamics and to use, produces reasonable results with an appropriate choice of level of no motion. More sophisticated methods such as β-spiral (Stommel and Schott 1977) and inverse methods (Wunsch 1978) have also been developed utilizing conservation principles of the ocean properties such as mass, salinity, and potential vorticity.

The large archive of observations now allows another type of computation to construct the velocity field. Pioneering calculations using the observed density field have been made by Sarkisyan and coworkers (1966, 1970, 1971). They used a modified set of the steady-state equations of motion to compute the velocity field for the Atlantic Ocean. However, Holland and Hirshmann (1972) integrated the Bryan (1969) time-dependent primitive equation model while holding the density fixed in time. This type of computation is attractive because 1) no modifications which may cause some loss of dynamics are made, 2) the spin-up time is only on the order of months, which can be compared to a thousand years of prognostic model and 3) there is no uncertainty due to the level of no motion like dynamic method. In fact, Holland and Hirshmann (1972) were quite successful in reproducing major features in the North Atlantic circulation.

The same computations as those used by Holland and Hirshmann (1972) were used for the mean and seasonal circulation in the Gulf of Alaska. The mean circulation is compared with the observed circulation and the seasonal variation in the gulf is extracted. Methods are first explained and then the results are compared with the observations.

Reproduced with permission of the copyright owner. Further reproduction prohibited without permission.

Section 2.2 Methods

The method of Holland and Hirschman (1972) specifies that the density field (temperature and salinity) does not change in time. Computations were done at two different resolutions both in horizontal and vertical. The first experiment has 1° horizontal grid and 32 vertical levels. The bottom of each level corresponds to the standard depth (10, 20, 30, 50, 75, 100, 125, 150, 175, 200, 225, 250, 300, 400, 500, 600, 700, 800, 900, 1000, 1250, 1500, 1750, 2000, 2500, 3000, 3500, 4000, 4500, 5000, 5500, 6000 m). The density data from Levitus (1982) were linearly interpolated onto the center of the model grid box where model temperature and salinity are defined. The finer spatial resolution of the second experiment is 30′ × 20′ × 20 layers and this same fine resolution is used later in the seasonal barotropic computation and one of the baroclinic computations. Depths of the bottom of the grid box are 20, 50, 100, 200, 300, 400, 600, 800, 1000, 1200, 1500, 2000, 2500, 3000, 3500, 4000, 4500, 5000, 5500, and 6000 m. Since the Levitus (1982) data are not defined at the model grid points, interpolations in both horizontal and vertical directions are necessary. Prior to these interpolations, seasonal three-dimensional temperature and salinity fields were constructed by combining the seasonal data defined at the upper 24 standard depths and the annual mean data at the lower standard depths. The seasonal data were then assigned to the nearest model depth from data at 33 standard depths and two dimensional interpolation scheme was used to interpolate the one-degree data onto the model horizontal grid points.

Biharmonic diffusion is used instead of Laplacian diffusion and the coefficients are -4×10^{21} for 1° model and -6×10^{19} for high-resolution model. The low-resolution model ocean is closed at 40° N and 160° E and the Bering Sea is included in the computation. The high-resolution model is closed at 45° N and 179° 30′ W and Kodiak Island and Queen Charolette Island are connected to the land and no passage to the Bering Sea is resolved. At the southern

Reproduced with permission of the copyright owner. Further reproduction prohibited without permission.

and western boundaries, which are not natural boundaries, a slip boundary condition is used. A no-slip boundary condition is applied at the land-sea boundary.

Integration from the initially motionless state with 1 hour time step is performed for one month for 1° model and for two months for high-resolution model. This leads to a quasi stationary state. Wind stress was not applied since the observed density field already has wind information (Holland and Hirschman 1972). Holland and Hirschman (1972) report only 5 % decrease in Gulf Stream transport when wind is not included in the model and they conclude that the pressure torque associated with the bottom topography is the main vorticity input.

Reproduced with permission of the copyright owner. Further reproduction prohibited without permission.

Section 2.3 Results

After 30 days of integration, the kinetic energy averaged over the entire volume of the model can be represented by a stationary state with the inertial and 7–day oscillations superimposed upon it (Figure 2.1). The final, steady state kinetic energy of 1° case (about 0.5 *ergs/cm*^{3}) is lower than that of high-resolution case (about 0.8 *ergs/cm*^{3}). The amplitude of the inertial oscillation decays in the early phase of computation, but its amplitude remains constant afterwards until the end of computation in both cases.

A 7–day oscillation is present in the high-resolution case but not in 1° case. This low-frequency oscillation is identified as a westward propagating quasi-geostrophic normal mode (Pedlosky 1982). The normal mode in a closed rectangular basin has a frequency given by

$$\sigma_{mn} = -\frac{\beta}{2\pi\{(m^2/x_o^2 + n^2/y_o^2)\}^{1/2}}, \quad m = 1,2,3,..., \quad n = 1,2,3,..., \tag{2.1}$$

where x_o and y_o are lengths of the basin in x (zonal) and y (meridional) directions, respectively. Then, the period of the lowest mode (m=n=*1*) is 21 days with x_o=4000 km, y_o=1600 km, and β at 50° N. This period is too large compared to the observed period of 7 days. The higher modes have longer periods and also the decrease in the dimension of the model domain (the model domain of this thesis is not rectangular in shape and the land-sea boundary of the model would have an effect to decrease the dimension) would only increase the period. A possible explanation is then to increase β. In a barotropic ocean, the horizontal gradient of the bottom topography has the exactly same dynamical effect as β (Pedlosky 1982). The total potential vorticity gradient in the presence of bottom topography is

$$\left(\beta - \frac{f}{H}\frac{\partial H}{\partial y}\right)\hat{\mathbf{i}} - \frac{f}{H}\frac{\partial H}{\partial x}\hat{\mathbf{j}} \tag{2.2}$$

where $\hat{\mathbf{i}}$ and $\hat{\mathbf{j}}$ are unit vectors in x and y directions, respectively and H is the water depth. A region where the depth change occurs rapidly exists east of 150° W in the gulf. f/H

Reproduced with permission of the copyright owner. Further reproduction prohibited without permission.

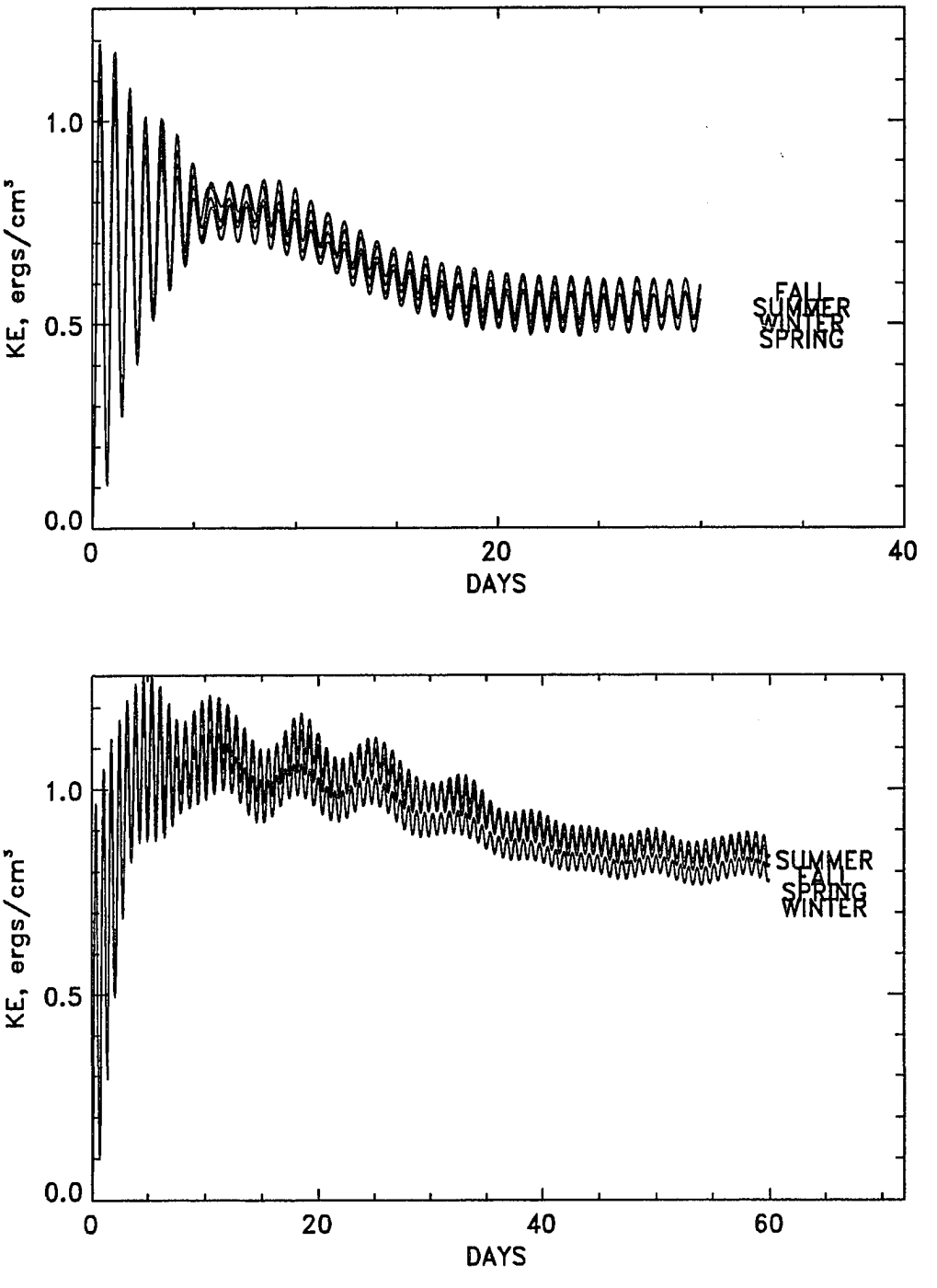

Figure 2.1 Basin-averaged kinetic energies (*ergs/cm*^{3}) of 1° diagnostic case (upper) and high-resolution case (lower).

Reproduced with permission of the copyright owner. Further reproduction prohibited without permission.

contours align northwest to southeast in this region indicating that the bottom topography effect is dominant in f/H. At 50° N, β is $1.47 \times 10^{-13}\ cm^{-1}sec^{-1}$ and the water depth change is 2.5 km over 25 degrees of longitudinal distance with a mean water depth of 4.5 km (the contour lines of 5 km and 2.5 km in Figure 1.7 are used for these estimates). This depth change produces the ambient potential vorticity gradient of $3.47 \times 10^{-13}\ cm^{-1}sec^{-1}$. Therefore, the effect of bottom topography is almost 2.5 times larger than the planetary vorticity gradient. The frequency of the normal mode would be also 2.5 times larger than that without the bottom topography and the 7–day period oscillation observed in the high-resolution diagnostic model is due to the effect of bottom topography. But note that the normal mode of 7–day period was possible because the model domain is closed. In a real ocean where there are no walls at 180° and 45° N, the frequency will be different if there is ever any of such an oscillation.

Results from 1° diagnostic model are discussed first. Contour plots of the stream functions of the vertically integrated transport (Figure 2.2) show no significant differences in the circulation pattern from season to season that any season can be selected for a discussion of the mean circulation in the Gulf of Alaska. In fact, one of the goals of this thesis is to explain why the seasonal variability in the gulf is so small compared to the large fluctuations in the atmospheric conditions. A cyclonic gyre occupies most of the model region extending from the western artificial boundary at 160° E to the coast of America and small anticyclonic gyres are present near the southern artificial boundary and in the eastern Bering Sea. The southwestward flowing Alaska Stream is identifiable as a narrow and intense current from 145 W to the dateline. The current width is about 250 km and the volume transport is about 12 Sv near Kodiak Island. As the Alaska Stream flows downstream, the transport increases to about 20 Sv at 154° W. But the transport decreases downstream of this longitude until it begins to increase again around 160° W. This pattern of increase and decrease in the transport of the Alaska Stream is due to the low values in the stream function (a cyclonic gyre has negative values of the stream function)

Reproduced with permission of the copyright owner. Further reproduction prohibited without permission.

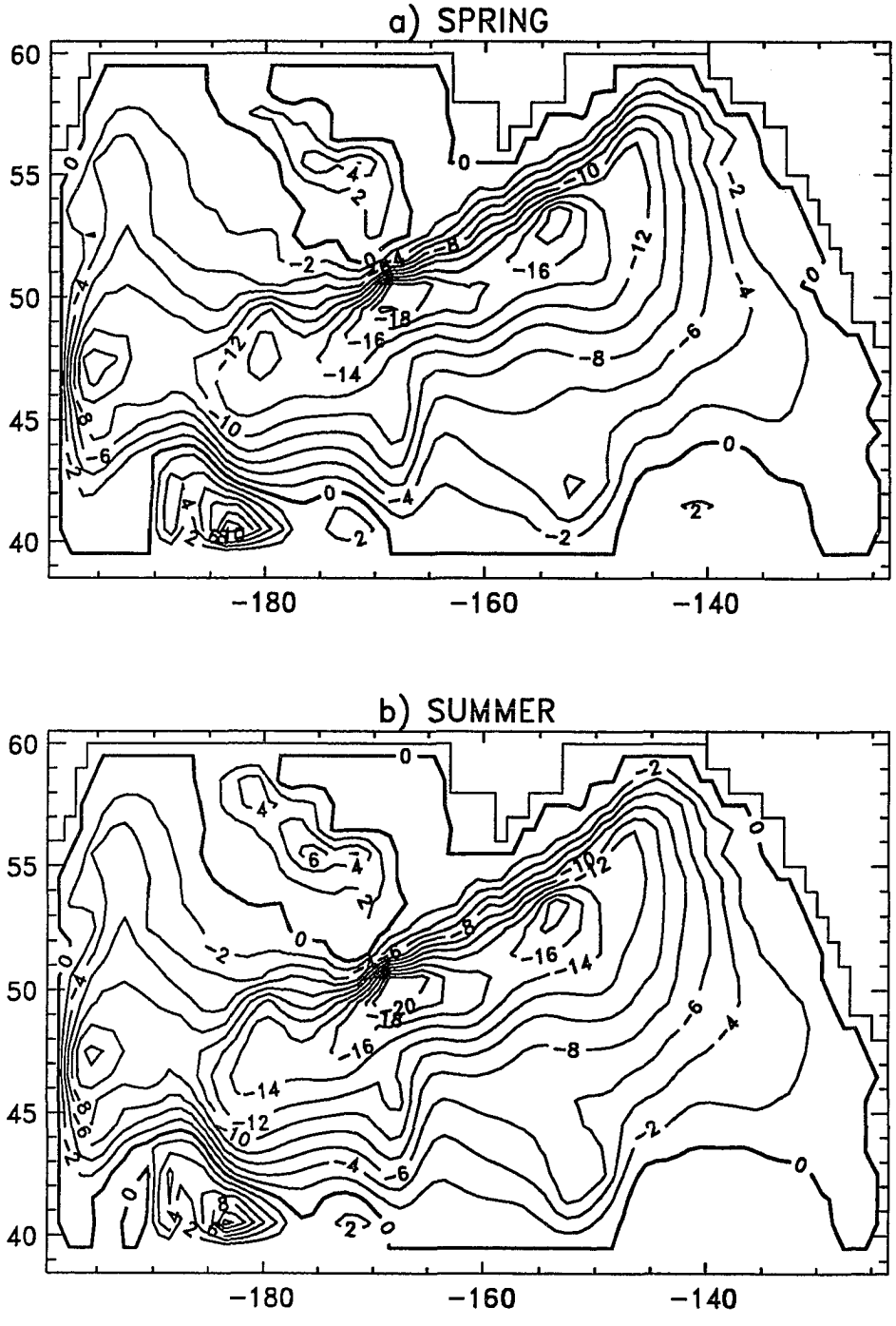

Figure 2.2 Contour plots of the stream function in: a) spring, b) summer, c) fall, d) winter, and e) annual mean and f) seasonal range of the stream function.

Reproduced with permission of the copyright owner. Further reproduction prohibited without permission.

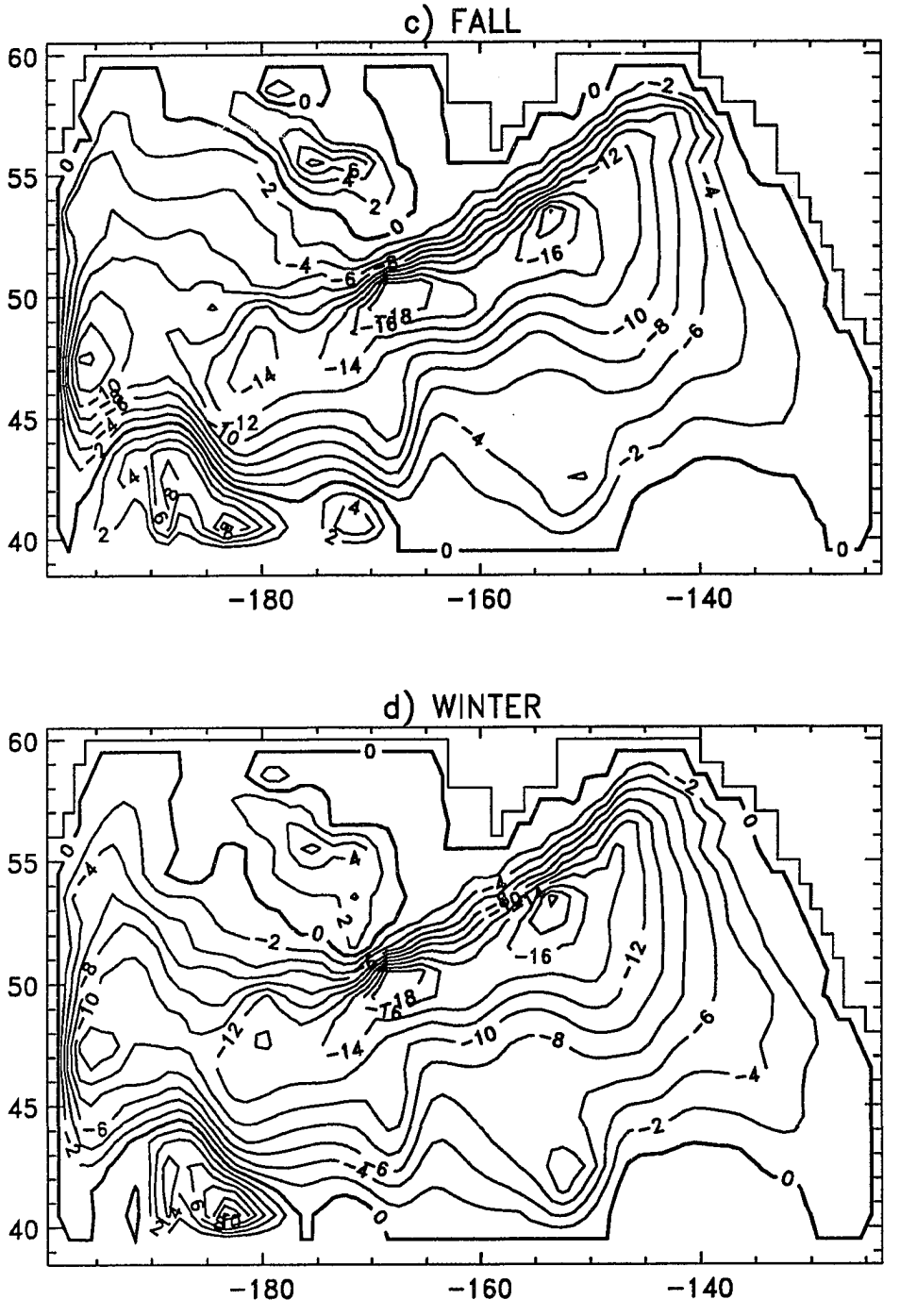

Figure 2.2 (continued)

Reproduced with permission of the copyright owner. Further reproduction prohibited without permission.

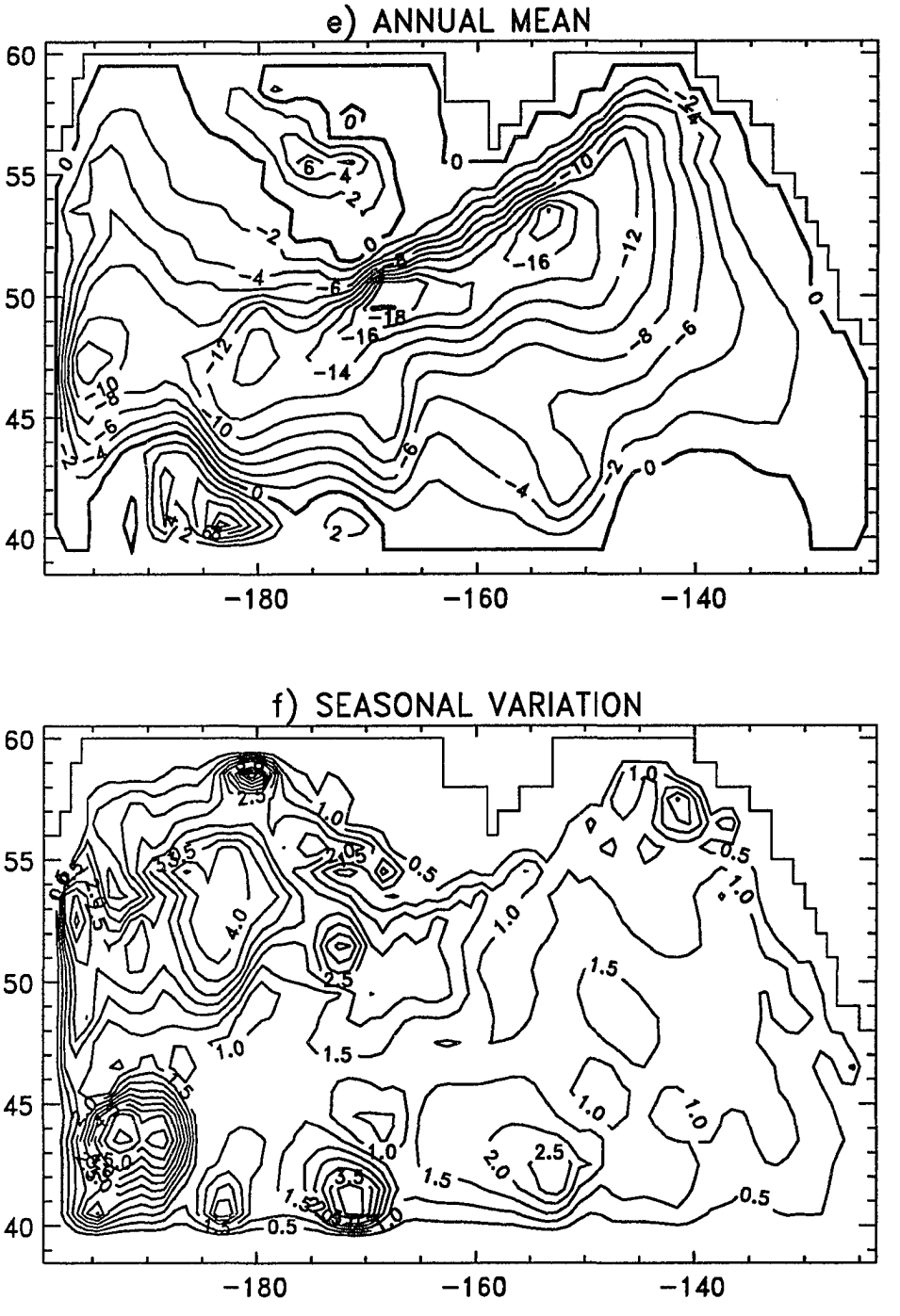

Figure 2.2 (continued)

Reproduced with permission of the copyright owner. Further reproduction prohibited without permission.

located just south of the Alaska Stream. They are found at 154° W, 170° W and 180° and recirculations occur in the first half region between two lows.

Since Figure 2.2 represents the total transport from surface to bottom, it is not appropriate for a comparison with observations which are usually referenced to 1000 or 1500 *db*. Furthermore, the contribution by the slow deep circulation, which is affected strongly by topography, is contained in the stream function (Holland and Hirschman 1972). For these reasons, another plot which shows particle tracks released at every grid point is prepared to understand the circulation in the upper 1000 m (Figure 2.3). Mean horizontal velocity of the upper 1000 m in fall is used to compute positions of each particle in the horizontal plane at regular interval by a formula

$$\frac{d\vec{x}}{dt} = \vec{u} \tag{2.3}$$

using the linear interpolation for the velocity.

Most of the features in the contour plot of stream function (Figure 2.2) are also identifiable: the Subarctic Current and its bifurcation into Alaska Current and California Current, the Alaska Stream, and recirculation. However, the western boundary current along the artificial western wall at 160° E and the small anticyclonic gyres near the southern boundary are now missing. Their absence in the surface circulation proves that these features are due to the artificial boundaries where the stream function is forced to be constant (zero). It is also interesting to note that the currents near the artificial boundaries behave as if there is no boundary, i.e., the currents near these boundaries show strong in- and outflow perpendicular to them.

Observations of the deep circulation below the wind-driven surface circulation are rare. Results from this diagnostic computation can provide a picture of deep circulation within limitations of the model. Particle track plots for the depth from 1000 m to 4000 m are prepared at 1000 m intervals (Figure 2.4—2.6). Particles are followed for one year in 1000 m – 2000 m and for two years in the deeper depth ranges. The first thing to note is the absence of the

Reproduced with permission of the copyright owner. Further reproduction prohibited without permission.

Reproduced with permission of the copyright owner. Further reproduction prohibited without permission.

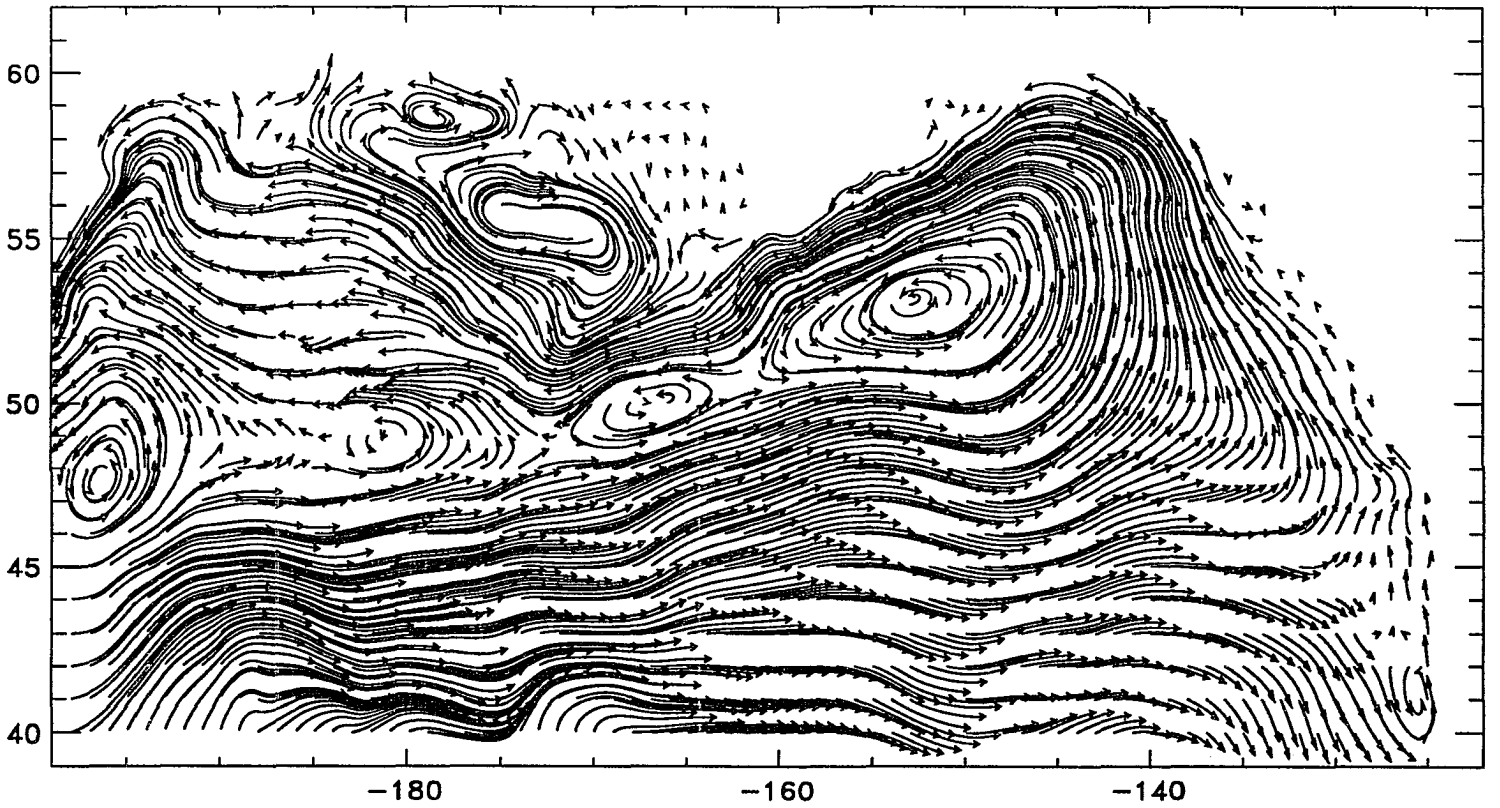

Figure 2.3 Particle tracks followed for one year show the fall diagnostic circulation in the upper 1000 m (the position is computed every 5 days).

systematic eastward flowing Subarctic Current below 2000 m. A partly systematic eastward flowing current still exists in 1000 m – 2000 m but completely disappears below this depth range. Instead, the deep currents are weak and directions are variable in space. In general, there is a northward flowing current in the eastern part of the gulf, east of about 150° W and westward flowing current to the west of 150° W. This northward flowing current feeds the Alaska Stream. West of 170° W, the extension current of the Alaska Stream, is joined by the westward flowing current and flows to the south.

Support to the pattern of the model deep circulation can be found in Reid and Arthur (1975). Their maps of geopotential anomalies at 2500 db relative to 3500 db and 3000 db relative to 4000 db show a northward flowing current near the coast of America and westward flowing current to the west. Although these flows are relative, geostrophic currents, the agreement with the model results is encouraging.

One conspicuous feature that distinguishes the model's deep circulation (Figure 2.4—2.6) from that of the surface is the appearance of the small closed circulations or eddies of 200–500 km in size. They are more clearly defined in the deeper depth ranges but it seems that they are not related to the mesoscale topographic features like seamounts except for the one at 170° E, 44° N which might be due to Emperor Seamount chain. In fact, no other seamount is resolved by 1° resolution of this model. Two cyclonic eddies located offshore of the Alaska Stream at 153° W and 167° W are related to the center of the Alaska gyre and the recirculation in the surface layers. To the south of these eddies there are four more eddies between 150° W and 180° (Figure 2.5) of unknown origin. One possible cause of these eddies is the change of model depth in this region. Actual field observations are necessary for comparison with the model results and these eddies remain to be studied further.

A small anticyclonic eddy exists at about 140° W, 55° N, which might be the Sitka eddy (Figure 2.4 and 2.5). Another anticyclonic eddy is also seen at 50° N (Figure 2.4) and in

Reproduced with permission of the copyright owner. Further reproduction prohibited without permission.

Reproduced with permission of the copyright owner. Further reproduction prohibited without permission.

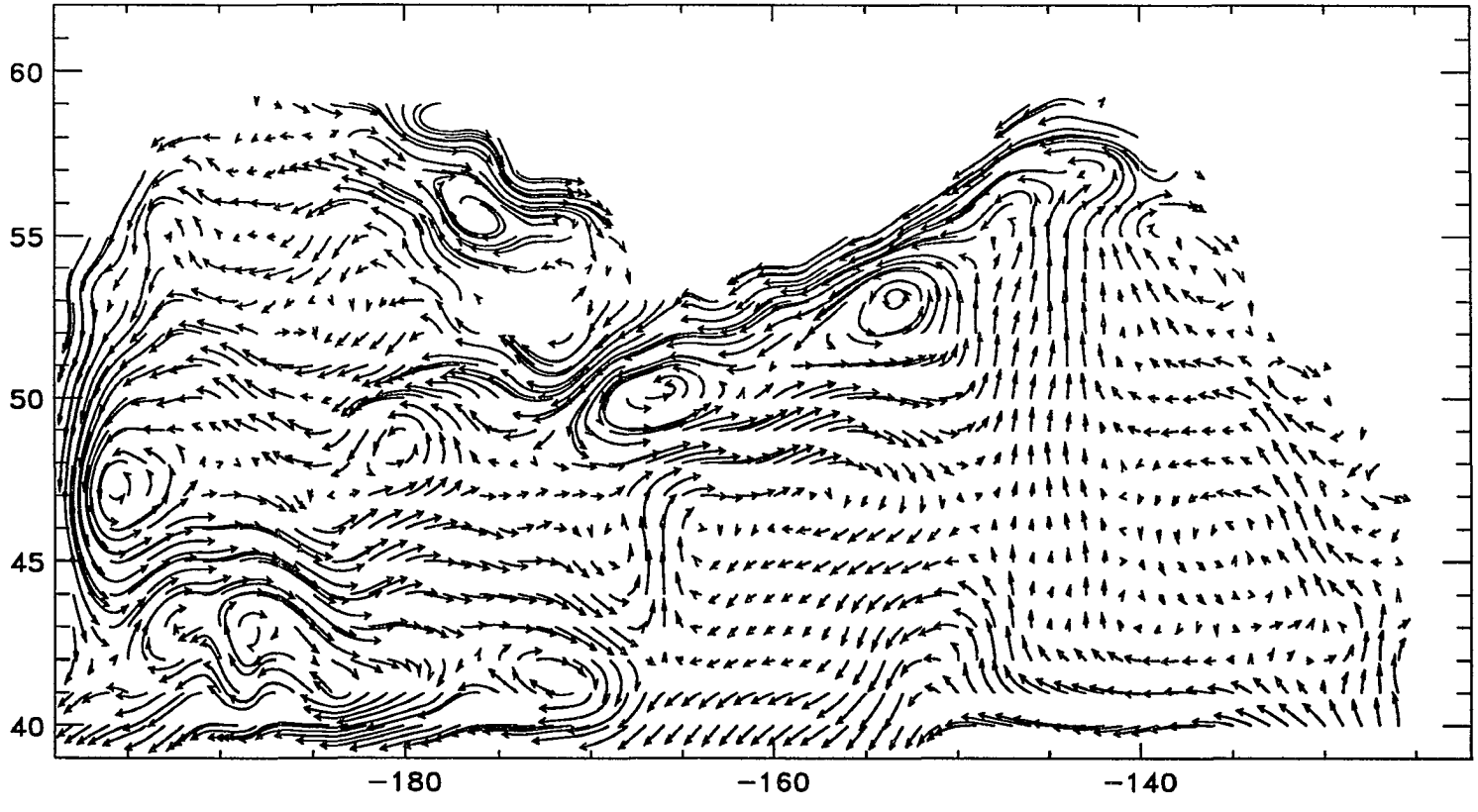

Figure 2.4 Particle tracks followed for one year show the fall diagnostic circulation in 1000–2000 m (the position is computed every 5 days).

Reproduced with permission of the copyright owner. Further reproduction prohibited without permission.

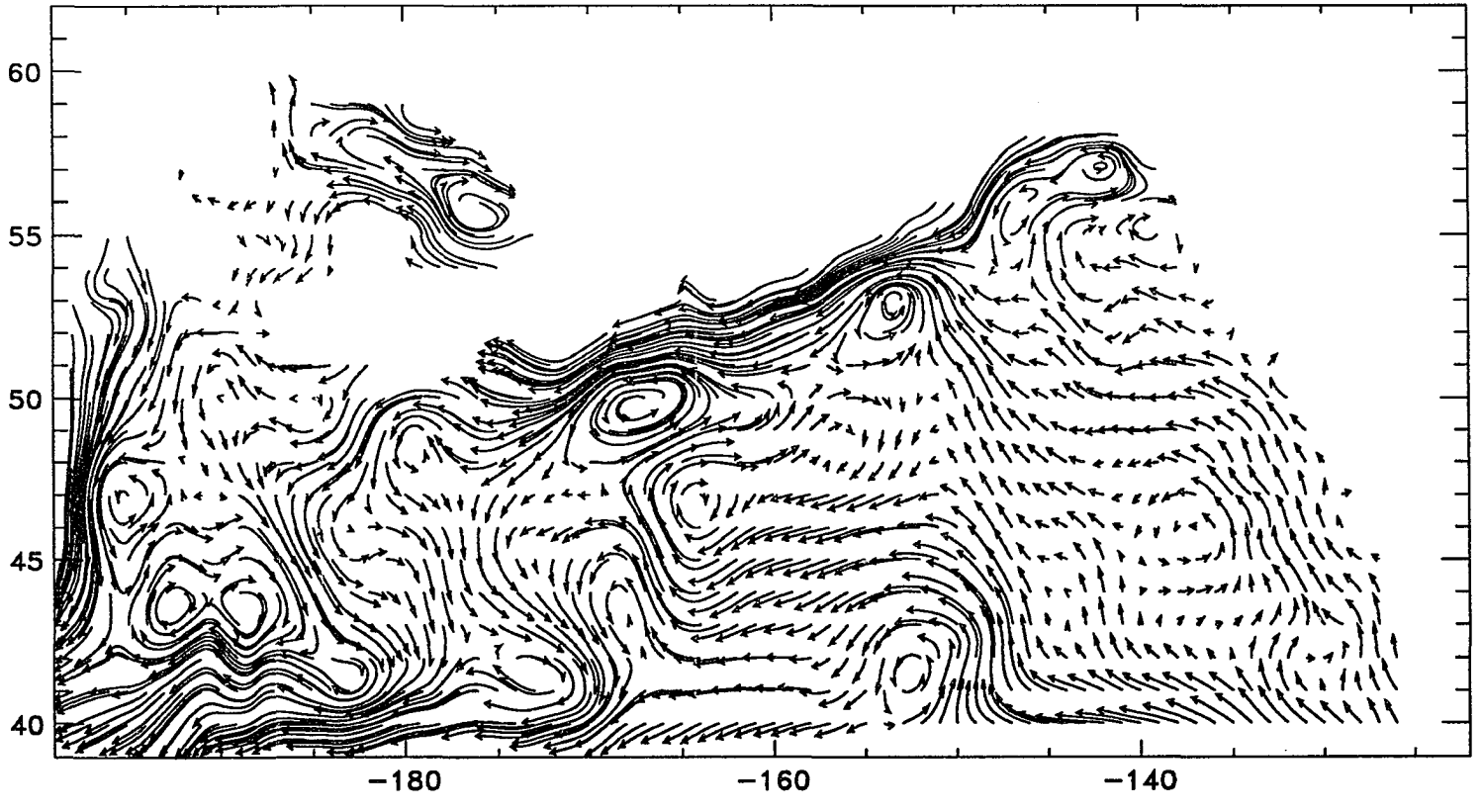

Figure 2.5 Particle tracks followed for two years show the fall diagnostic circulation in 2000–3000 m (the position is computed every 10 days).

Reproduced with permission of the copyright owner. Further reproduction prohibited without permission.

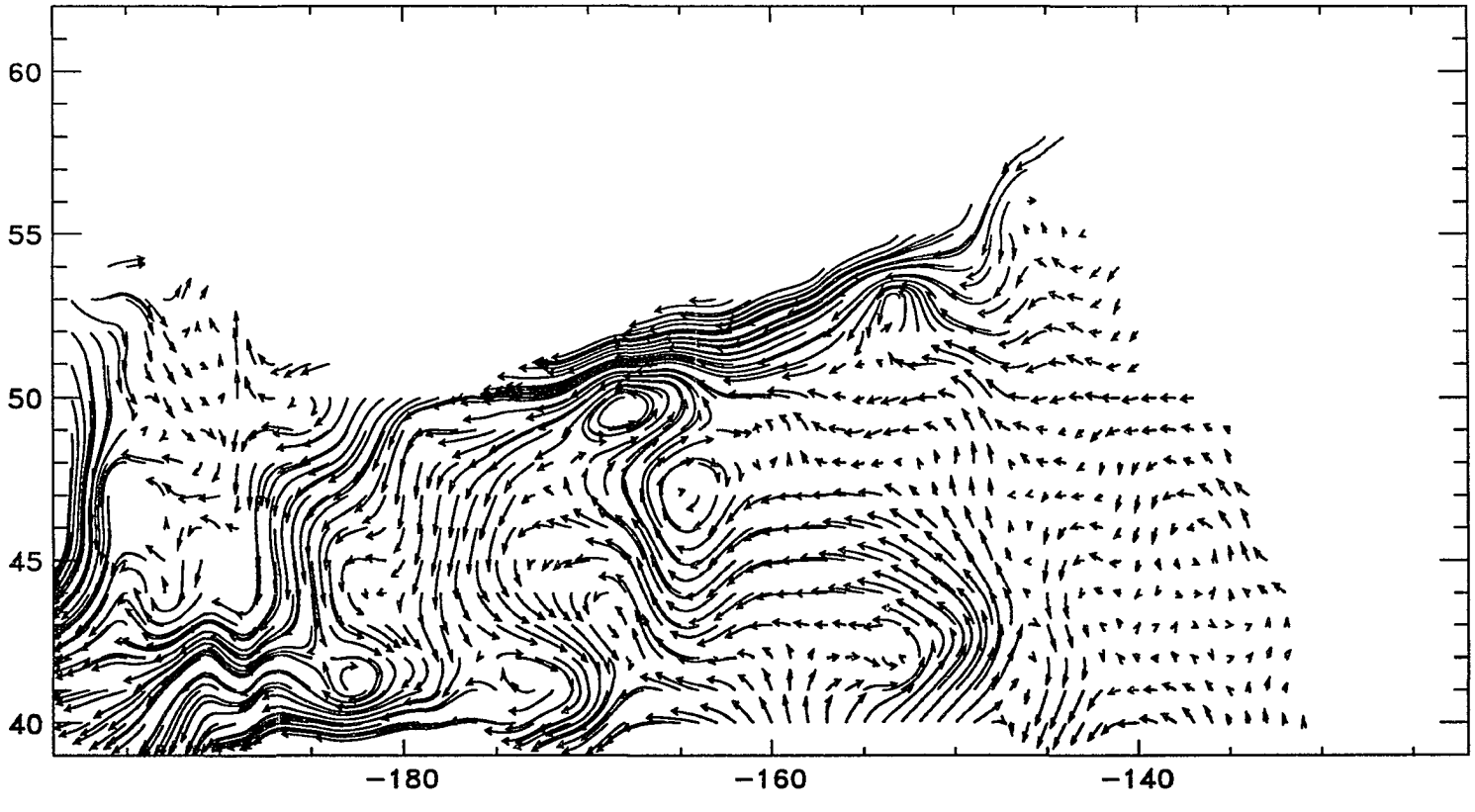

Figure 2.6 Particle tracks followed for two years show the fall diagnostic circulation in 3000–4000 m (the position is computed every 10 days).

fact, the current system just offshore along the west coast of North America shows a pattern of inshore southward flowing current and offshore northward flowing current connected by crossshelf currents resulting in an anticyclonic eddy.

An estimate of the seasonal variability in the Gulf of Alaska is made from the results of the diagnostic computation to compare with observations and also results from other experiments of this thesis. The seasonal variability of the diagnostic circulation is defined as the range of variation of the stream function over four seasons. The stream function data at the end of the computation which show the same phase of oscillation in all seasons (Figure 2.1) are used.

Large seasonal variations are seen in four places; southwest corner of the model domain, around 170° W near the southern boundary, around 180° in the Bering Sea near the northern boundary, and 51° N, 175°W in the interior. These locations are, however, excluded from the discussion because they are probably due to boundary condition (first three locations) and numerical instability (last location). Discussions will be focused in the region east of 165° W and north of 45° N where no signs of numerical instability were noted during the computation. The seasonal range of variation is less than 2 Sv except for about 2.5 Sv in the northeast corner of the gulf. The seasonal range is about 0.5–2 Sv along the Alaska Stream from 145° W to 165° W.

A seasonal shift of the Alaska gyre is observed in the numerical model results of Cummins (1989). The Alaska gyre shifts 150-250 km offshore from the west coast of North America in July and resumes its position in January. Cummins (1989) further suggested that the interannual gyre shift (Royer and Emery 1987) is simply an amplification of this regular seasonal variation. However, no seasonal shift of the Alaska gyre is observed in the diagnostic model results of this thesis. Instead, only a slight intensification of the westward flowing current between 140° W and 150° W is noticeable in fall and winter.

Sea level is a good parameter that can be used to compare the model results with the

Reproduced with permission of the copyright owner. Further reproduction prohibited without permission.

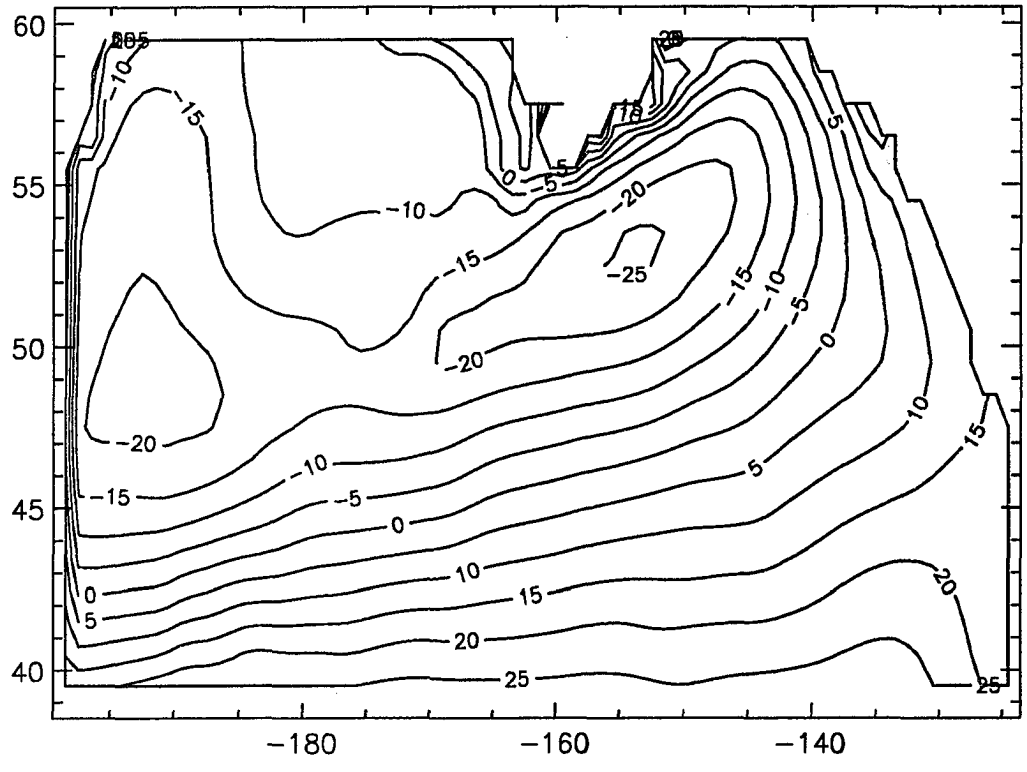

Figure 2.7 Distribution of the sea levels (in cm) in summer defined by $\eta = p/\rho_0 g$, where ρ_0=1.02 *gr/cm*^{3} and g=980.6 *cm/sec*^{2}.

observation (dynamic topography). The sea level is not an explicit variable computed during the integration in this model but it is possible to compute sea level from the sea-surface pressure gradient. The distribution of the sea level at the surface (actually at 10 m depth) shows the surface circulation pattern nicely and the lowest sea level is found at 53° N, 153° W (Figure 2.7). If the sea levels –15 cm and –20 cm are respectively defined as the main axis and the offshore limit of the Alaska Stream between 145° W and 175° W the sea level change across the Alaska Stream is 15-20 *cm.*

Now, results from the high-resolution model are described. Note that no new information is added to the internal pressure gradient force because the density data used in the high-resolution

Reproduced with permission of the copyright owner. Further reproduction prohibited without permission.

diagnostic model are interpolated from 1° data onto the grid points. So, if a new and different circulation appears in this high-resolution model, it should be the result only of the resolution of model.

The large-scale circulation revealed by the stream function (Figure 2.8) also shows a cyclonic gyre but some differences from the 1° model are noted in detailed features. In the shallow region east of a line connecting 45° N, 140° W and 52° N, 150° W, the circulation is complicated by the presence of mesoscale features. This is probably due to the mesoscale topographic features which are now resolved by the high-resolution model. Large values of the seasonal range found north of 50° N near the western boundary (Figure 2.8) appear to be due to the mismatch between the density field and the bottom topography. The seasonal range, however, in the Alaska Stream region agrees with 1° model and is about 0.5–2 Sv.

Reproduced with permission of the copyright owner. Further reproduction prohibited without permission.

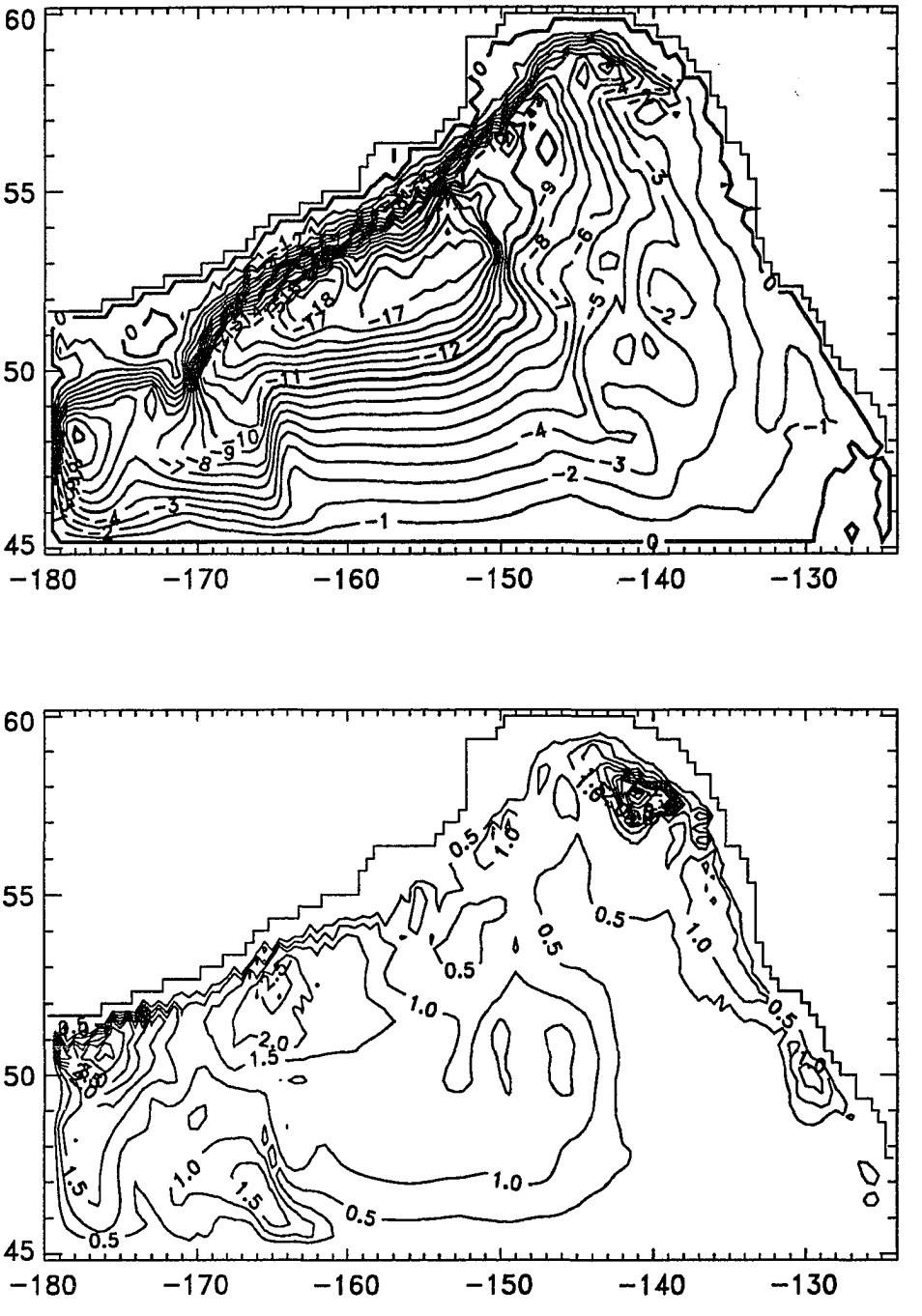

Figure 2.8 Contour plots of the annual mean (upper) and the seasonal range (lower) of the stream function of the high–resolution diagnostic model.

Reproduced with permission of the copyright owner. Further reproduction prohibited without permission.

Section 2.4 Discussion and conclusions

Major currents are well reproduced by the 1° diagnostic computation, especially in the upper 2000 *m*. In the Gulf of Alaska, the Alaska Stream persists from the surface through the deep layers but the Subarctic Current is not identified as a broad eastward flowing current at depth as it is at the surface. Instead, a broad flow enters from the south, east of 150° W, and a part of it merges into the deep Alaska Stream and the rest returns to the south after travelling to the west. This deep circulation feature agrees well with Reid and Arthur (1975) but needs more study. The deep circulation also revealed several eddies of unknown origin.

A difference is noted in the eastern part of the gulf between results by 1° model and high-resolution model and the mesoscale topography was mentioned in the previous section as a possible source of this discrepancy. In fact, the diagnostic model has been known to produce some erroneous results due to the mismatch between the near-bottom density gradient and topography (Sarmiento and Bryan 1982). This can be more clearly understood by looking into the vorticity balance of the vertically averaged, linear, frictionless (no horizontal and bottom friction), and steady flow (Holland 1973).

$$-\beta\frac{\partial\psi}{\partial x} + \nabla \times \vec{\tau}_w - J[P_b, H] = 0 \qquad (2.4)$$

where ψ is the stream function, β is the meridional gradient of Coriolis parameter f, $\vec{\tau}_w$ is the wind stress, P_b is the bottom pressure, H is the depth, and J is the Jacobian operator.

Equation (2.4) shows the balance between planetary vorticity advection (first term), wind stress curl (second term), and bottom pressure torque (third term). In the absence of wind forcing as in this diagnostic model, a balance between planetary vorticity advection and bottom pressure torque is achieved. This is why Holland and Hirschman (1972) concluded that the pressure torque associated with the bottom topography is the main vorticity input. The bottom

Reproduced with permission of the copyright owner. Further reproduction prohibited without permission.

pressure torque can be further decomposed into contributions by the surface pressure P_s (it is equivalent to the sea level because of the rigid-lid approximation in this model) and the pressure by the vertically integrated density,

$$J[P_b, H] = J[P_s, H] + J\left[g \int_H^0 \rho dz, H\right]. \tag{2.5}$$

Problems can arise because the length scale of the topography is considerably smaller in high-resolution model (one grid is about 37 km in latitude) than those of the sea level and the density field (the smoothing scale of the density data is about 700 km). In 1° model, the discrepancy in length scales between the pressure field and topography was not as serious, but in high-resolution model it generates erroneous vorticity input and alters the circulation. If more freedom is given to the density field so that it can adjust to the topography the problem would be much less severe.

Sarmiento and Bryan (1982) allowed the density to change in time with one restriction that the predicted value is forced toward the observation value within a specified time scale and called it "robust-diagnostic model". This model can be placed between the pure diagnostic model which does not allow the density to change in time and the prognostic model in which the density is one of the predicted variables. However, this robust-diagnostic model is not tried despite its ability to improve the results because 1) a prognostic model is going to be tried and 2) the 1° diagnostic model produced a realistic circulation. The pure diagnostic model used here and by Holland and Hirschman (1972) computes the velocity and the sea level from the time-independent density field so that the ocean can have a barotropic transient response only. This is because the baroclinic motion is only possible through density variations.

An important result from this diagnostic model is the seasonal variability. Seasonal variation of the Alaska Stream determined from the stream function is about 1.5 Sv but no significant seasonal variations are found in the overall pattern of the circulation in the Gulf of Alaska. Since

Reproduced with permission of the copyright owner. Further reproduction prohibited without permission.

no wind forcing is used in the diagnostic model, this small seasonal variation in the circulation indicates that there is little seasonal change in the density field. However, the diagnostic model alone cannot explain why the seasonal variability in the Gulf of Alaska is small in the presence of large seasonal fluctuation in the wind stress. A prognostic model with a realistic configuration of the gulf might be able to unveil the secret of the seasonal variability in the gulf.

Reproduced with permission of the copyright owner. Further reproduction prohibited without permission.

Chapter 3 SEASONAL BAROTROPIC MODEL

Section 3.1 Introduction

Long-term mean transport of the western boundary current can be estimated by the zonal integration of mean wind stress curl, i.e., the Sverdrup balance can be used to estimate the mean transport (for example, Warren and Owens 1988). However, the seasonal variation cannot be explained by the integration of the seasonal wind stress curl. For example, the observed transport of the Florida current is maximum in summer with an annual cycle of 4 Sv while the integration of the seasonal wind stress curl predicts maximum in winter with an annual variation of 15 Sv (Anderson and Corry 1985b). In the Gulf of Alaska, the seasonal fluctuation of the wind stress curl also predicts maximum transport in winter with an annual cycle of almost 20 Sv (Musgrave *et al.* 1990). However, there are little seasonal variations in the transport of the Alaska Stream (Reed *et al.* 1980; Royer 1981) and the maximum occurs in spring (Royer 1981). The diagnostic model in the previous chapter also shows a small seasonal cycle of about 1 Sv in the transport of the Alaska Stream. In summary, the predicted seasonal variation in the transport of the western boundary current by the wind stress curl is far larger than the observations and the predicted phase is not consistent with the observations. Therefore, it is clear that the ocean responds to the seasonal fluctuations in the wind with different dynamics from the Sverdrup dynamics which is successful in explaining the annual mean circulation.

There are several theoretical and numerical works on the ocean response to the time-dependent forcing. Veronis and Stommel (1956) first considered the ocean response to the time-dependent wind forcing and concluded that in the middle and high latitudes the ocean response is mainly barotropic. However, Lighthill (1969) showed that the relatively fast group velocity of the baroclinic Rossby wave near the equator is responsible for the reversal of the

Reproduced with permission of the copyright owner. Further reproduction prohibited without permission.

Somali Current which takes place within a month from the change of the seasonal monsoon. In a series of papers, Anderson and Gill (1975) developed a two-layer one-dimensional model to study the barotropic and baroclinic responses of the ocean to the wind forcing, Anderson and Killworth (1977) include the effect of topography, and Anderson and Corry (1985a) applied time-dependent wind forcing to their model. From these studies, Anderson and Corry (1985a) concluded that the propagation time of the baroclinic Rossby wave from a generation point to the western boundary is important in determining whether the western boundary current will respond barotropically or baroclinically. According to Anderson and Corry (1985a and b), the response of the western boundary current to the annual forcing is barotropic at the middle and high latitudes and the Sverdrup balance holds in the interior only after the passage of baroclinic Rossby waves.

Following these theoretical and numerical works, Anderson and Corry (1985b) used a two-layer model in the North Atlantic and Greatbatch and Goulding (1989) used a vertically integrated linear model in the North Pacific to see if a barotropic response alone can explain the observed seasonal variability. The results showed that the predicted seasonal variation in Florida Current by Anderson and Corry (1985b) was in phase with observation, but their amplitude was several factors smaller. Greatbatch and Goulding (1989) also reached at the similar conclusion for the Kuroshio. To explain the discrepancy of the model results with the observations, Anderson and Corry (1985b) mentioned baroclinic Kelvin waves and topographic Rossby waves as possible contributors.

In this chapter, a barotropic model is used to investigate the influences of bottom topography on the ocean response to the seasonal forcing in the Gulf of Alaska. In the eastern gulf, the lines of constant barotropic potential vorticity f/H are almost parallel to the coastline of North America so that one can expect that barotropic Rossby waves propagate northwestward instead of westward. If this is true, wind changes in the Alaska Current region over the continental

Reproduced with permission of the copyright owner. Further reproduction prohibited without permission.

slope offshore of North America would be important in the seasonal variation of the Alaska Stream transport.

The same configuration of the high–resolution diagnostic model (Chapter 2) is adopted except that the density (constant temperature at 4° C, constant salinity at 33 psu) is now constant. The barotropic ocean with no motion initially is forced by seasonally varying wind stress. Each month has 30 days and monthly mean wind stress is considered as being observed in the middle of that month (ex. Jan. 15 for Jan. mean wind stress). Both components of the wind stress are first decomposed into harmonics and new wind stress is reconstructed at every timestep from the mean and annual and semi-annual harmonics to be used for the actual wind forcing. This approach has an advantage over the linear interpolation because the frequencies of the forcing are exactly known and it also prevents a sudden change of wind stress between months which may occur by the use of linear interpolation if the seasonal wind stress does not change smoothly in time. Integration is done for 14 months and stream function data are sampled every 5 days and three-dimensional velocity fields are sampled every half a month. Also, data are retained at seven monitoring points over various regions in the gulf for 6–hour intervals. These points are indicated in Figure 3.3 which also shows bottom topography defined by the number of layers.

Biharmonic coefficient in the interior is -4×10^{19} for momentum. Laplacian coefficient in the sponge layer near the western boundary is 1×10^{8}. A linear bottom friction is also used with the damping time scale (γ) of 5 days.

$$-\frac{1}{\gamma}\vec{u}_b \tag{3.1}$$

where γ^{-1} is the damping coefficient and has the dimension of $time^{-1}$ and $\vec{u}_b$ is the velocity of the bottom layer. Horizontal boundary conditions are same as in the diagnostic model, i.e., no-slip at the land-sea boundary and slip boundary condition at the artificial wall. The sponge

Reproduced with permission of the copyright owner. Further reproduction prohibited without permission.

layer is intended to dissipate the incoming waves and eddies propagated to the western boundary at 180° so that they cannot affect the interior circulation by reflection or reentering the interior.

Reproduced with permission of the copyright owner. Further reproduction prohibited without permission.

Section 3.2 Results

The spin-up time of the seasonal barotropic model from the initial state of no motion is 5–10 days. The basin-averaged kinetic energy shows a large seasonal variation with its maximum of 0.08 *ergs/cm*^{3} in January and almost zero in July (Figure 3.1) and is in phase with the wind stress curl. As is evident from the maximum kinetic energy (0.08 *ergs/cm*^{3}), the kinetic energy level is low; it is only about 10 % of the kinetic energy of the circulation in the high-resolution diagnostic model (Figure 2.1). The mean circulation shows a cyclonic gyre but the mean transport is only about 1 Sv in the Alaska Stream (Figure 3.2). Large transports (about 2 Sv), compared to the other parts of the gulf, are found in the northeast corner, along the artificial western boundary, and in the region between 170° W and 150° W south of 50° N. The circulation in the last region needs an explanation because comparison with the topography indicates that the topography is the major factor in shaping the circulation in this region.

The semi-closed cyclonic gyre sitting between 170° W and 150° W south of 50° N consists of a western boundary current which flows southward along the 5500 m isobath, a northward interior flow between two isobaths of 5500 and 5000 m, and zonal flows connecting these meridional flows (Figure 3.3). The 5500 m isobath where the western boundary current is formed is actually a line across where the depth decreases suddenly from 6000 m to 5500 m. In fact, all contours greater than 1500 m represent the sudden depth change of 500 m (thickness of the grid box below 1500 m). On each side of the depth discontinuity, there exists a large area with constant depth (5500 m in the eastern area and 6000 m in the western area) and a separate cyclonic gyre is formed in each area. The western gyre can be easily understood because the depth discontinuity acts like a wall blocking the flow to the east. For the eastern gyre, the increase in depth appears to have the same effect as the wall noting that a similar circulation is

Reproduced with permission of the copyright owner. Further reproduction prohibited without permission.

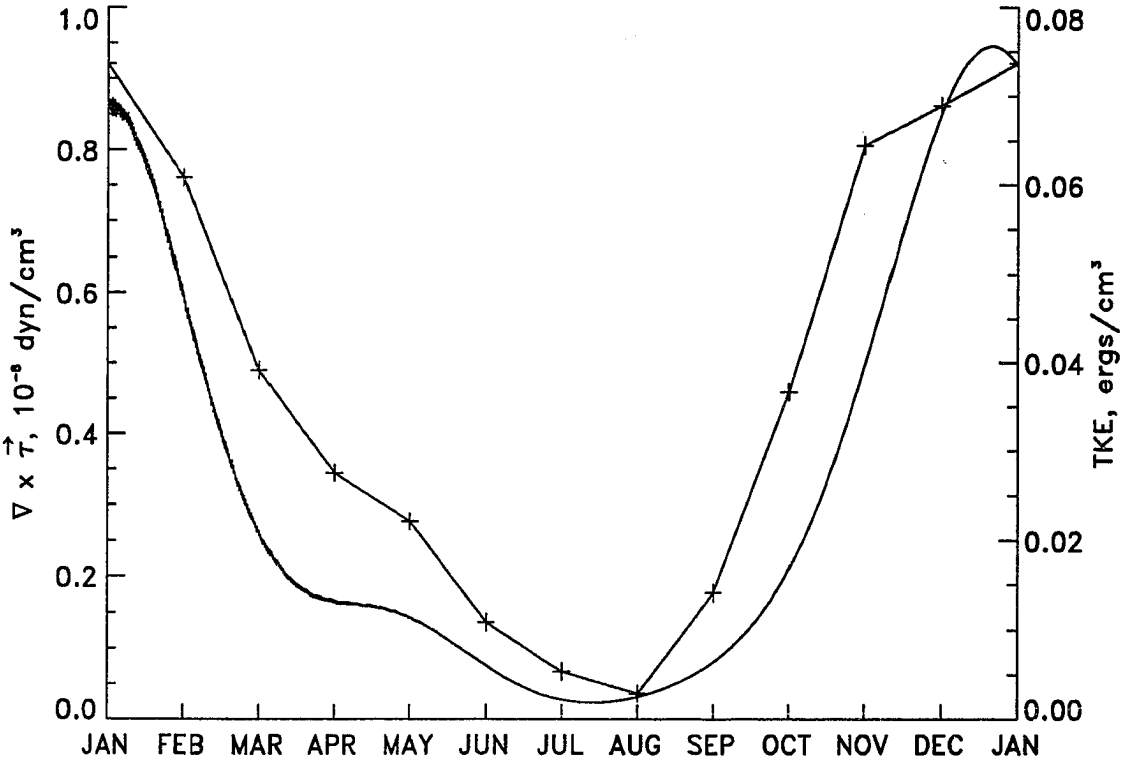

Figure 3.1 Basin-averaged kinetic energy (*ergs/cm*^{3}) of the seasonal barotropic model and the average wind stress curl over the entire model domain (+).

also found in other model result in which a midocean ridge separates a flat-bottom ocean into two subdomains (Anderson and Killworth 1977).

One can understand how these interior gyres are formed by noticing that they have the same shape as the basin scale gyre which is composed of the Sverdrup interior and the western boundary current. The northward flow in the flat area is the Sverdrup response to the positive wind stress curl and is returned to the south by the western boundary current. It is possible because of the flat-bottom interior where the Rossby waves propagate westward without any interruption by bottom topography. Certainly, there is no such a depth discontinuity in the Gulf of Alaska and the almost flat Aleutian Abyssal Plain where the depth decreases gradually to

Reproduced with permission of the copyright owner. Further reproduction prohibited without permission.

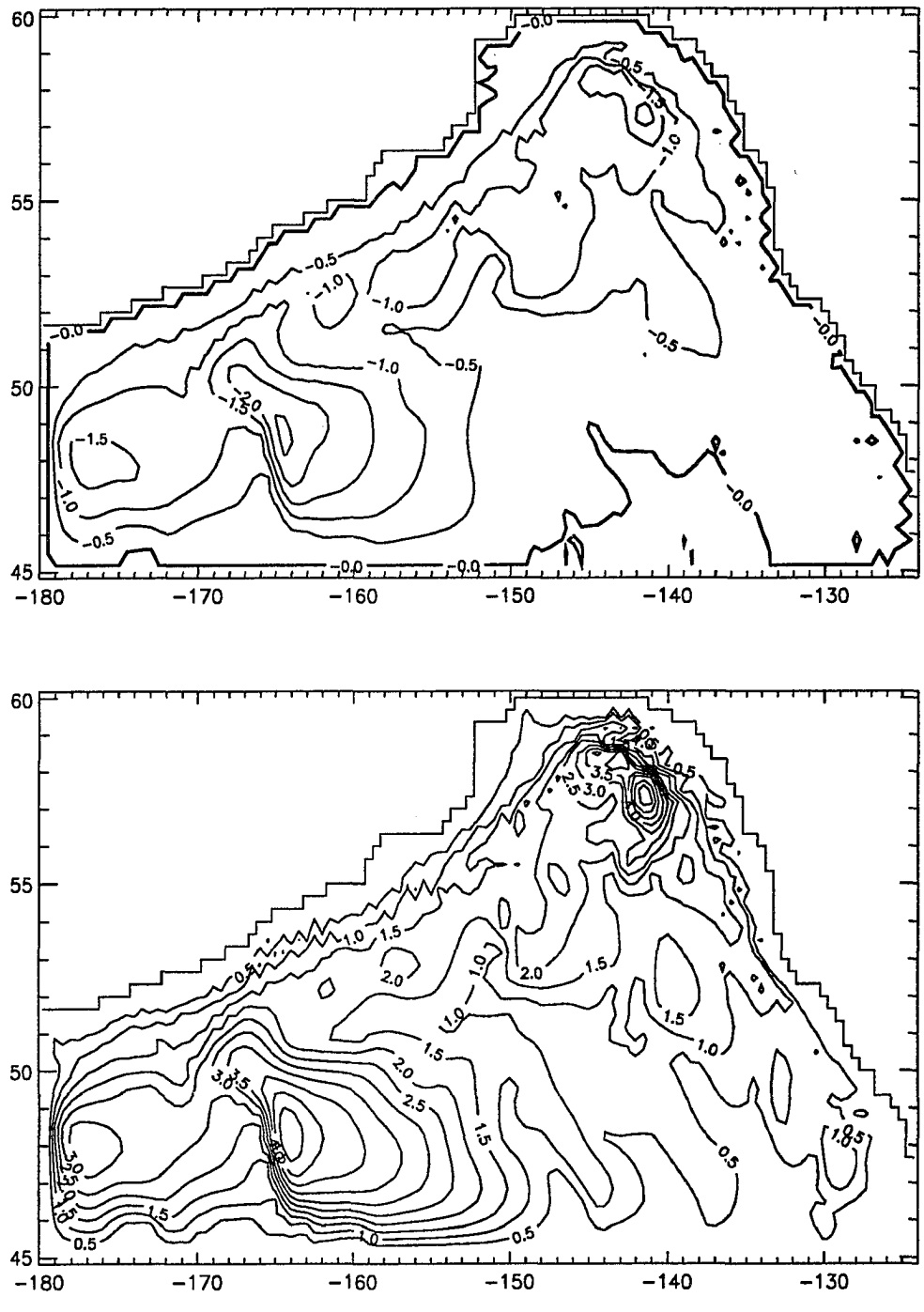

Figure 3.2 Annual mean (upper) and seasonal range (lower) of the stream function.

Reproduced with permission of the copyright owner. Further reproduction prohibited without permission.

the east occupies this region.

Question arises then about how good this depth representation of the real topography is in terms of dynamics. This is a serious question considering that the barotropic model is governed strongly by the topography and the resulting circulation can be different depending on the scheme of the depth representation. In works of Anderson and Corry (1985b) and Greatbatch and Goulding (1989), the topography was represented by a continuous and smooth surface rather than by steps as in this model. The continuous depth distribution can produce a better result than the step representation. However, the present vertical resolution (20 levels) is not poor in resolving the topography as evident by comparing the contour plots of the continuous depth distribution (Figure 1.7) and of the step representation (Figure 3.3). Furthermore, the continuous depth distribution is not possible for the nonlinear, three-dimensional models used in this thesis. One may also expect that the Rossby waves actually propagate more or less westward in the Aleutian Abyssal Plain because of its flatness.

In the region east of the 5000 m isobath the depth decreases to the coast and the flat area that can support a separate interior gyre is much smaller than the region west of the 5000 m isobath. In this eastern region, the topography is complicated by the presence of seamounts and the interpretation of the circulation in this shallow region is not easy. The time-dependent forcing also makes it difficult to detect any propagation of the signals. However, another computation forced by the annual mean wind shows a northwestward propagation of the barotropic Rossby waves in the region east of 150° W as can be expected by the dominance of H in the potential vorticity f/H. Therefore, the step representation of the bottom topography in this thesis is acceptable. There are, however, attempts to avoid the step representation; for example, Spall and Robinson (1990) use both a level model near the surface and a sigma coordinate system below a certain level to follow the bottom topography smoothly.

Interestingly, the spatial distribution of the seasonal range (Figure 3.2) is similar in pattern

Reproduced with permission of the copyright owner. Further reproduction prohibited without permission.

Reproduced with permission of the copyright owner. Further reproduction prohibited without permission.

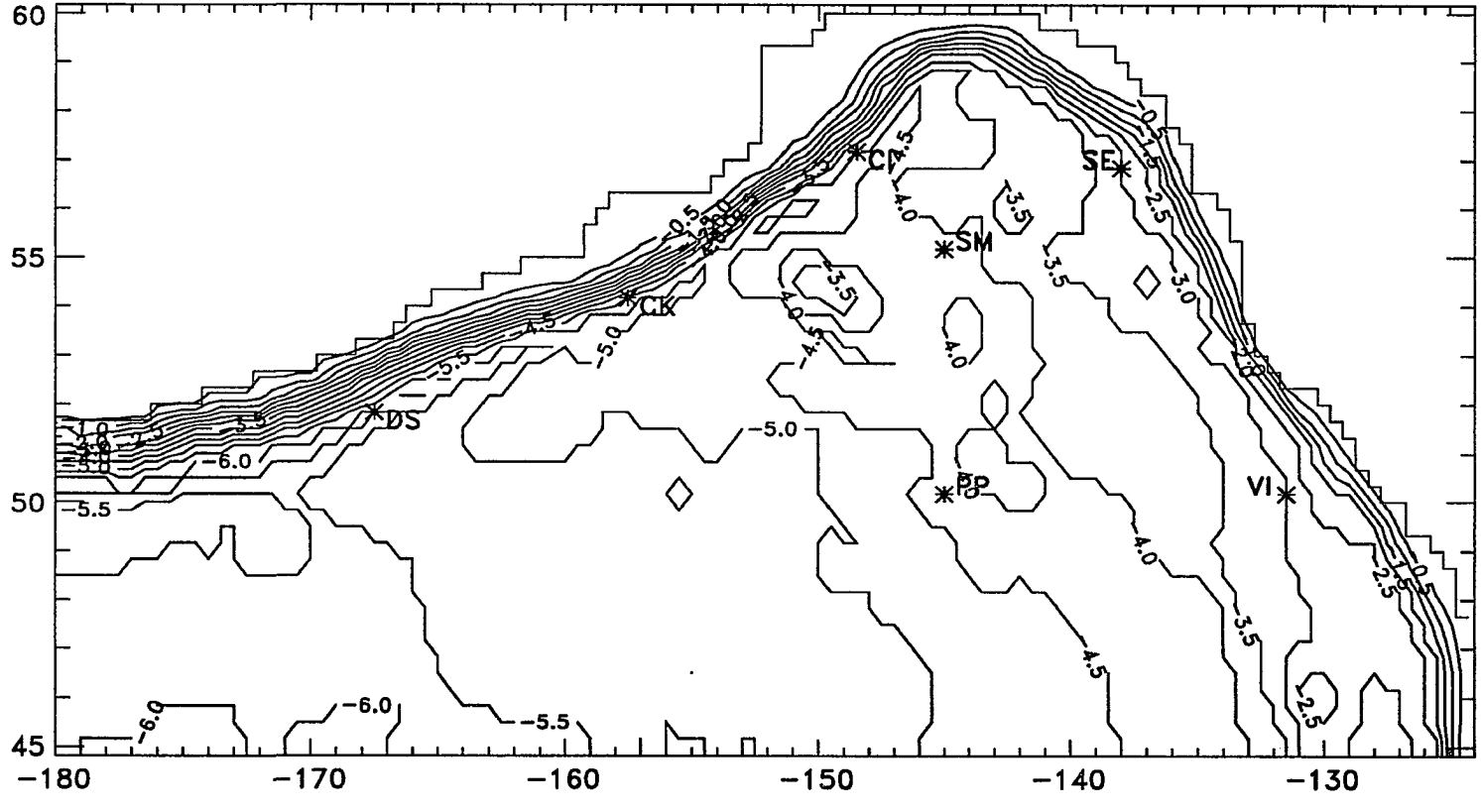

Figure 3.3 Topography defined by number of layers. Seven monitoring points are marked by asterisk (VI: Vancouver Island, PP: Papa, CI: Cook Inlet, SE: Sitka Eddy, SM: Seamount, CK: Chirikof Island, and DS: Downstream)

to that of the mean circulation. Large seasonal ranges are found in the region with large mean transports and vice versa. This can be understood through a simple example. Imagine another circulation forced by the same wind as the one used here but with opposite sign, i.e., the wind stress curl is negative in this case. Then the circulation would be anticyclonic with the same spatial pattern as the cyclonic circulation by the positive wind stress curl. This is because the propagation of the Rossby waves does not depend on the sign of the wind stress curl. Consequently, the range defined by the difference of these two circulations would be just twice of any of them and large values will be found in the region with large transports.

The above example demonstrates why the seasonal range of the seasonal barotropic model has the same spatial distribution as the annual mean circulation. There is one condition that has to be satisfied for this example to be directly applicable to the seasonal barotropic model where time-varying wind forcing is used. It is the fast response time of the barotropic model. The fast response time (5–10 days) implies that the energy input by the wind forcing propagates relatively fast and the time-dependent wind forcing has little effect on the propagation. If this is true, the final monthly circulation would differ little whether the model is forced by the time-dependent seasonal wind stress or by the time-independent monthly wind stress. Thus, the seasonal range of the seasonal barotropic model which is defined by the difference between the maximum and minimum values of the stream functions over one year period can also be estimated from the monthly circulation forced by the strongest positive wind stress curl and the strongest negative wind stress curl. Greatbatch and Goulding (1989) also noted similar results in the North Pacific and attributed it to the nearly zonal topography in the North Pacific, which does not block and detour the westward propagation of barotropic Rossby wave like the midocean ridge in the North Atlantic. The agreement with the Greatbatch and Goulding (1989) also indicates that the seamounts, which are major topographic irregularities in the gulf, do not detour the propagation of the barotropic Rossby waves.

Reproduced with permission of the copyright owner. Further reproduction prohibited without permission.

Comparison of the monthly mean circulation (Figure 3.4) with the wind stress curl (Figure 1.9) provides more evidence for the close relationship between the ocean response and the wind forcing. There is a change in the position of the zero stream function line throughout the year. The cyclonic gyre is strongest in oceanic fall (December) and covers the entire model domain. In spring (June), the cyclonic gyre has shifted westward and in summer (September), the gyre has shifted northward. These shifts of gyre are the response to the change of the wind stress curl pattern. The annual mean position of the zero wind stress curl line lies along about 45° N in the ocean though it becomes roughly parallel to the coastline on the land over North America (Figure 1.8). The position of the zero line oscillates throughout the year (Figure 1.9) and the largest westward shift of the zero line occurs in spring (June) and the largest northward shift occurs in summer (September). These shifts of the zero wind stress curl line are clearly reflected in the monthly mean circulation (Figure 3.4) and the positions of the zero wind stress curl line and the zero transport line are almost coincident.

Comparison of the seasonal range (Figure 3.2) with diagnostic results (Figure 2.8) provides an interesting interpretation. There is a similarity in the spatial pattern of the seasonal ranges of the two models; for example, large values in the northeast corner of the model domain and in the region between 160°–170° W south of 50° N and small values between these two regions. Especially, the seasonal range between 145° W and 165° W along the Alaska Steam is about 1–2 Sv and agrees with values from the diagnostic model. This agreement may indicate that the seasonal fluctuation in the transport of the Alaska Stream is mainly barotropic and agrees with the theory of Anderson and Corry (1985a). However, differences in spatial patterns are also noted in some places and they are due to the mismatch of the density field with the bottom topography in the diagnostic model as explained before.

Reproduced with permission of the copyright owner. Further reproduction prohibited without permission.

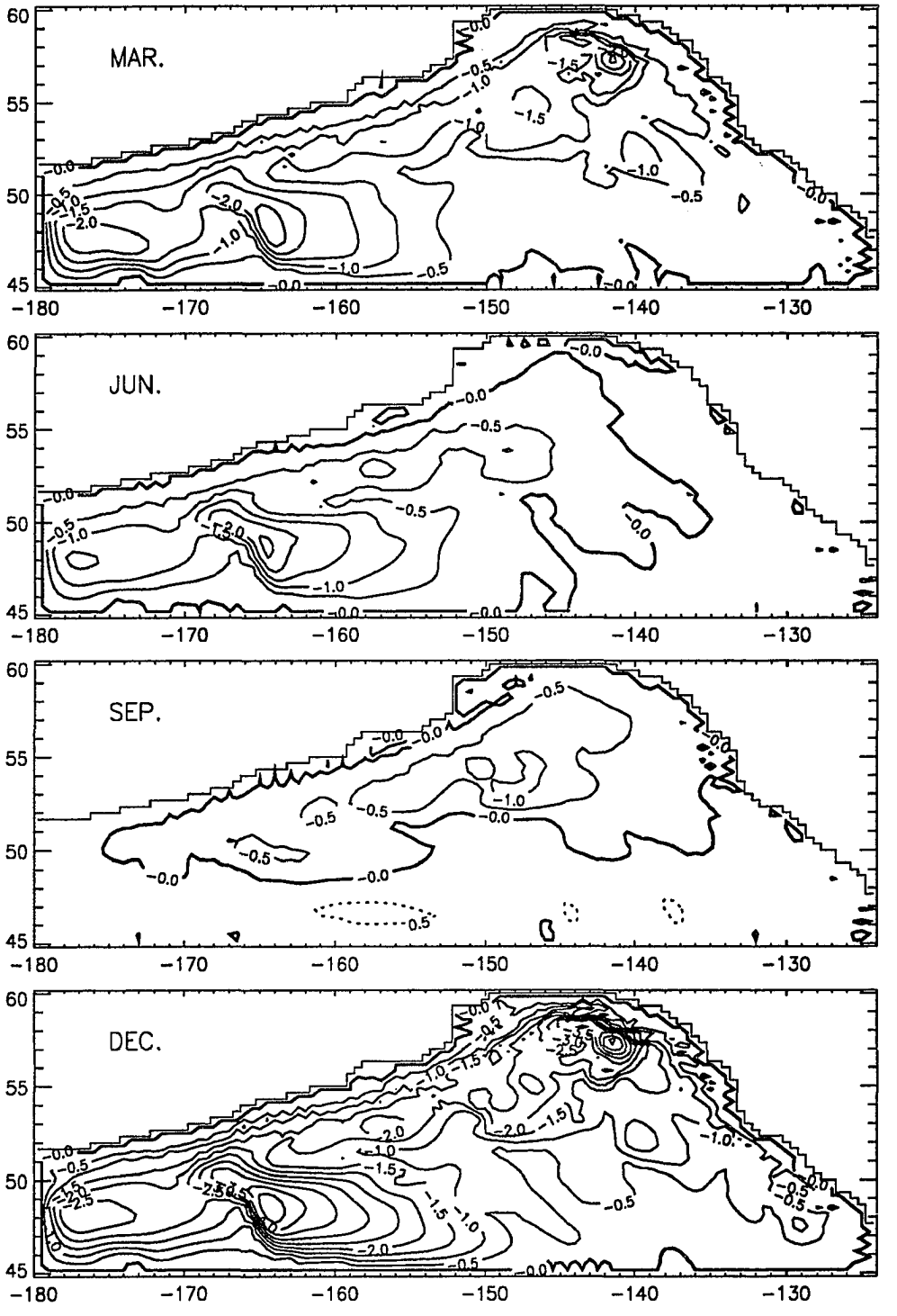

Figure 3.4 Contour plots of the stream functions at the middle of March, June, September, and December.

Reproduced with permission of the copyright owner. Further reproduction prohibited without permission.

Section 3.3 Discussion and Conclusions

In a barotropic ocean, the information imparted by the wind stress curl will be carried away from the interior by barotropic waves only. If the ocean is flat, the barotropic Rossby waves will establish a mean circulation according to the Sverdrup dynamics, i.e., the transport of the western boundary current is equal to the interior transport driven by the wind stress curl. On the other hand, if the ocean has bottom topography, the resulting circulation is relatively weak and is strongly controlled by topography. This is because the barotropic Rossby waves no longer propagate in zonal direction and instead, they propagate along the constant lines of f/H so that their destination is not necessarily the western boundary. Furthermore, mesoscale topographic features like seamounts would dissipate the barotropic waves easily by trapping and scattering them into high-frequency waves.

The annual mean circulation of the seasonal barotropic model shows a cyclonic gyre as a direct response to the mean positive wind stress curl in the gulf. The energy level estimated by the maximum value is only 10 % of that of the high-resolution diagnostic circulation. The spatial patterns of the seasonal range and the annual mean circulation are very similar to each other. The seasonal range is almost proportional to the annual mean transport and a simple example is used to explain it. The monthly mean circulation also has a similar pattern as the annual mean except for September when the negative wind stress curl is strong. The monthly mean circulation closely follows the seasonal change in the wind stress curl and a westward shift of the cyclonic gyre occurs in oceanic spring (June) and summer (September) when the negative wind stress curl gains the strength.

The seasonal barotropic model predicts 1–2 Sv for the seasonal variation in the transport of the Alaska Stream and this value agrees well with results of the diagnostic model. This agreement leads to the important conclusion that the seasonal response of the transport of the

Reproduced with permission of the copyright owner. Further reproduction prohibited without permission.

Alaska Stream is mainly barotropic. However, a further discussion will be made in Chapter 5 after the seasonal baroclinic model is completed.

Reproduced with permission of the copyright owner. Further reproduction prohibited without permission.

Chapter 4 ANNUAL MEAN BAROCLINIC MODEL

Section 4.1 Introduction

In Chapter 2, a diagnostic model was used to reproduce the mean circulation and examine the seasonal variability in the gulf. In Chapter 3, the Gulf of Alaska was assumed homogeneous and forced by the seasonal wind stress in the presence of bottom topography to determine if the seasonal variability can be explained by a barotropic response alone as predicted by Anderson and Corry (1985a). In this chapter, a numerical simulation of the mean circulation and mesoscale eddies in the Gulf of Alaska is attempted. Density stratification is introduced into the model to include the baroclinic motions which were not included in Chapter 3.

The spin-up time of the baroclinic ocean is considerably longer than that of the barotropic ocean and an equilibrium is achieved after the passage of baroclinic Rossby waves. However, the speed of first baroclinic Rossby wave is on the order of 0.01 *m/sec* at high latitude (Lighthill 1969) and it would take a decade for the baroclinic Rossby wave to cross the Gulf of Alaska at this speed. Therefore, it takes more time to spin up the baroclinic ocean at high latitudes than near the equator where the spin-up time is on the order of months.

The baroclinic model domain is the same one used in the high-resolution diagnostic model and is closed by artificial walls at the western (180°) and southern (45° N) boundaries. These walls block the water exchange and interaction of the Gulf of Alaska with the rest of North Pacific. Appropriate treatments on the walls are needed to minimize the possible effects of this isolation of the gulf. For example, across 180° where the western boundary of the model is located, the Alaska Stream flows westward and the Subarctic Current flows eastward. However, the presence of the wall in the model would force the Alaska Stream to flow southward along the wall and reenter the interior as the Subarctic Current. This transformation of the Alaska

Reproduced with permission of the copyright owner. Further reproduction prohibited without permission.

Stream to the Subarctic Current may be acceptable because no in- and outflows are prescribed at the western boundary in the model. However, waves and eddies propagating from the interior are also going to be reflected by the wall or reenter the interior resulting in the contamination of the interior circulation. In the real ocean, the waves do not reflect and the eddies do not join the eastward flowing Subarctic Current at this longitude (180°). Therefore, appropriate treatments on the westward propagating signals are needed for a successful simulation.

A radiating boundary condition has been used in some simple models (Camerlengo and O'Brien 1980; Chapman 1985), but no successful radiating boundary condition has been reported so far for primitive equation models to my knowledge. High friction region (so-called 'sponge layer') is also commonly implemented near the artificial boundary. In the sponge layer, the incoming waves and eddies are dissipated by the high friction to prevent them from contaminating the interior (Cummins and Mysak 1988). Usually, friction coefficients are increased gradually from the interior value to the high value in the sponge layer. In this thesis, however, Laplacian diffusion scheme with a constant coefficient over 10 grid points adjacent to the artificial western wall is adopted after various schemes have been tried. The Laplacian diffusion is chosen because it dissipates mesoscale motions more effectively than the biharmonic diffusion as shown in Figure 1.6. The sponge layer allows the Alaska Stream which enters the northern part of the sponge layer to leave as the Subarctic current through the southern part after all high-frequency, mesoscale motions originated from the interior have been destroyed.

The southern boundary is located near the zero wind stress curl line and the current direction at this latitude (45° N) is nearly zonal (Figure 1.1) even though there is an indication of the north-south flow as can be inferred from the intrusion of the low-salinity tongue at intermediate depth (Figure 1.5). A problem was noted when a slip-boundary condition is used at the southern boundary. Anticyclonic vortices were generated from the wall and anticyclonic circulation eventually filled up the eastern half of the gulf. The anticyclonic eddies were found

Reproduced with permission of the copyright owner. Further reproduction prohibited without permission.

to be generated by a strong eastward current formed as the strong westerly wind establishes downwelling along the southern boundary. As a remedy of this problem, a 'linear zone' is established over 2 grid points from the southern boundary where the advection terms are removed from both momentum and temperature (salinity) equations. This linear zone ensures no generation of anticyclonic eddies from the wall by eliminating a unrealistic downwelling responsible for the horizontal density gradient from which the anticyclonic eddies extract energy for their growth.

For the determination of density, the polynomial formula by Friedrich and Levitus (1972) is used with the depth assumed zero, i.e., ρ(s,t,0) is used instead of ρ(s,t,p). The effects of pressure on the density can be understood by the difference between these two variables expressed in terms of specific volume.

$$\begin{aligned}\alpha(s,t,p) - \alpha(s,t,0) &= \alpha(35,0,p) + \Delta_{s,t} + \delta_{s,p} + \delta_{t,p} + \delta_{s,t,p} \\ &\quad - \alpha(35,0,0) + \Delta_{s,t} \\ &= \alpha(35,0,p) - \alpha(35,0,0) + \delta_{s,p} + \delta_{t,p} + \delta_{s,t,p} \qquad (4.1)\end{aligned}$$

The terms on the RHS are missing effects by the choice of ρ(s,t,0) and represent the pressure effects. The last term is small and is always neglected in the determination of the density (Pond and Pickard 1982). The first two terms play no role in the computation of the pressure gradient force. The remaining terms represent the combined effects of temperature and pressure and of salinity and pressure, respectively, and are the major missing effects by the choice of ρ(s,t,0). These pressure terms may often be neglected in the upper 1 km so that the difference between ρ(s,t,0) and ρ(s,t,p) is not significant there. Another reason for choosing ρ(s,t,0) is that it produces a more stable solution than ρ(s,t,p) does. This is a serious advantage because it means that a small friction coefficient can be used for the generation of eddies which is one of the goals. Therefore, ρ(s,t,0) is used for the determination of density despite some missing effects.

Reproduced with permission of the copyright owner. Further reproduction prohibited without permission.

The first case is the simplest of three experiments in this chapter. It has only 3 vertical layers and a motionless ocean is forced by the annual mean wind stress. In the second case, the number of vertical layers is increased to 10 and the thermohaline forcing is included along with the wind. Finally, topography is included into the model and 20 vertical layers are used to resolve mesoscale topographic features. For all these experiments, the biharmonic diffusion is used with the coefficients being different from experiment to experiment.

Reproduced with permission of the copyright owner. Further reproduction prohibited without permission.

Section 4.2 3-layer Case

A three-layer (200, 800, and 5000 m), flat-bottom ocean which is initially motionless, horizontally homogeneous, but vertically stratified is forced by the annual mean wind stress. There is no thermohaline forcing to focus on the wind-driven circulation of a stratified ocean. This case is intended to study the spin-up process and also to find out if spontaneous eddies can be generated by the wind forcing only.

Initial temperatures and salinities are 7°, 4°, 1.5° C and 33, 34, 34.7 psu from the surface to bottom. Biharmonic coefficients are -1×10^{19} and -1×10^{20} cm^4/sec for momentum and diffusion, respectively. Coefficients for vertical momentum and diffusion are 30 and 0.3 cm^2/sec, respectively. The vertical viscosity is higher than usually adopted values, 1–10 cm^2/sec, but it has little effect on the results since the major dissipation of energy comes from the bottom and horizontal friction. Integration in time is carried out for almost two decades.

Table 4.1 Temperature, salinity, sigma-t, layer thickness (*d*), and effective depth (*h*, see text for the definition) of each layer.

Layer	T, °C	S	σ_t	d, m	h, m
1	7	33.0	25.93	200	
					0.20
2	4	34.0	26.98	800	
					0.67
3	1.5	34.7	27.78	5000	

The basin-averaged kinetic energy increases continuously until year 10 to the maximum value of 0.61 $ergs/cm^3$ and decreases slowly to 0.56 $ergs/cm^3$ at year 19. No high-frequency fluctuations are present (Figure 4.1) and the circulation pattern (upper panel of Figure 4.2)

Reproduced with permission of the copyright owner. Further reproduction prohibited without permission.

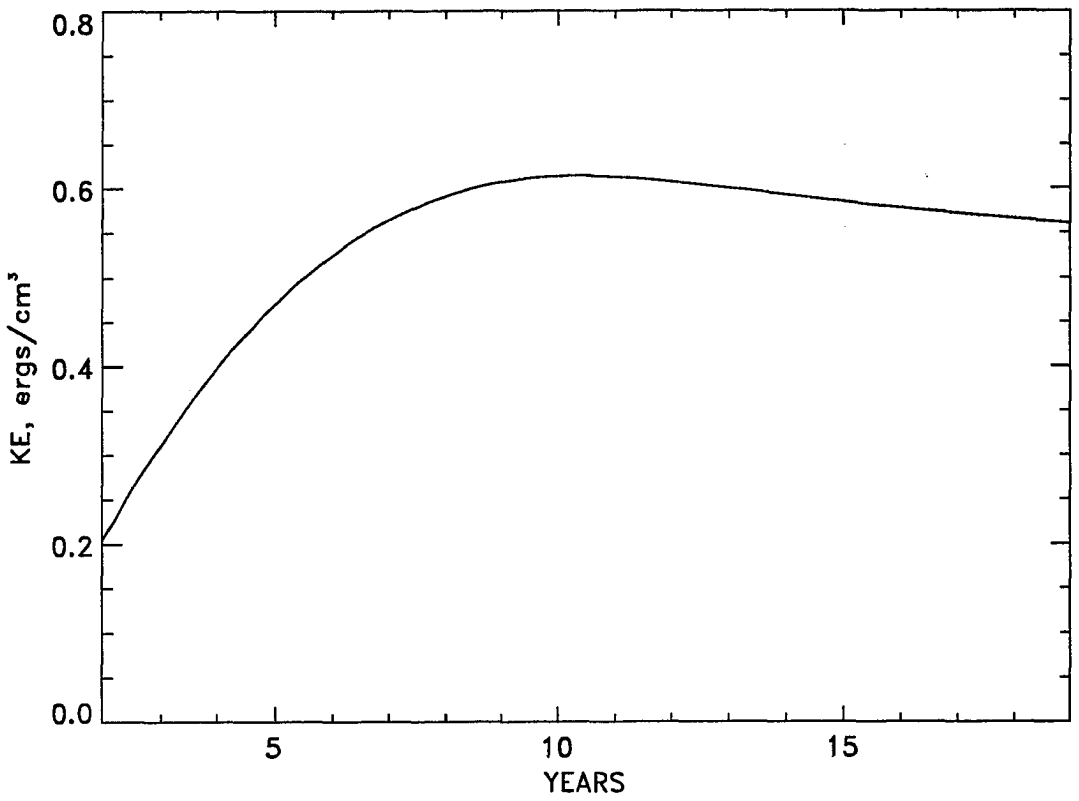

Figure 4.1 Time series of basin-averaged kinetic energy (*ergs/cm³*).

shows little change in time. The circulation pattern is somewhat different from the diagnostic model (Figure 2.2). In the diagnostic model, the eastward flowing Subarctic Current is broad, weak, and distributed equally meridionally. In this 3–layer model, however, most of the contour lines are passing within about 500 km from the sloping boundary along the Aleutian Islands Arc. Sverdrup transport (Figure 4.2) is computed from the wind stress curl to compare with the circulation of the 3–layer model and the agreement is good indicating that the circulation is dynamically consistent with the wind pattern.

The maximum transport of the Alaska gyre is about 12 Sv at 148° W, 56° N (Figure 4.2), consistent with the Sverdrup transport. The width of the Alaska Stream becomes wider

Reproduced with permission of the copyright owner. Further reproduction prohibited without permission.

as it flows downstream and another narrow western boundary current forms at the artificial western boundary. Most of the broad, weak current emanating from the western boundary flows eastward at first but soon flows northeastward to the head of gulf. Only 2 or 3 Sv flows through the region south of 50° N between 150° W and the eastern boundary.

Velocity vector plots in each layer (Figure 4.3) show a similar circulation pattern as the one by the stream function except for the bottom layer. In the upper two layers, a boundary current develops about 57° N, 137° W and flows westward. There is a strong eastward flow just south of the Alaska Stream. In the bottom layer, the cyclonic gyre which occupied all of the gulf in the upper two layers is now limited close to the Alaska Stream and an anticyclonic circulation prevails offshore. Also, a wavy fluctuation of the current path is seen south of 55° N near the coast of North America in the upper and middle layers but it is stationary in time with no indication of propagation.

Whether the circulation described so far is observable in the real ocean is not important in this simple case. As stated before, this case is intended for a study of the spin-up process in the gulf by the wind. From Figure 4.1, one can see that it took about 10 years for this model to reach an equilibrium and it agrees with the earlier estimate of the propagation time of the baroclinic Rossby wave. In Figure 4.4, zonal velocity in the bottom layer is depicted in time-longitude plot along a latitude line (48° 20′ N). Baroclinic Rossby waves propagate from 136° W to the western boundary at a speed of 0.8 *cm/sec* and are denoted by a dash-dot line. The dash-dot line forms a boundary of two regions. In the region to the right of the line, the isolines are almost parallel to the time axis (except 160°–140° W) indicating the completion of spin-up process while to the left of the line the zonal velocity increases in time. This agrees well with the theoretical and numerical results of Anderson and Gill (1975).

The phase speed of 0.8 *cm/sec* of the baroclinic Rossby wave also agrees well with Lighthill (1969). Using the normal mode approach, Lighthill (1969) studied responses of a flat-bottom

Reproduced with permission of the copyright owner. Further reproduction prohibited without permission.

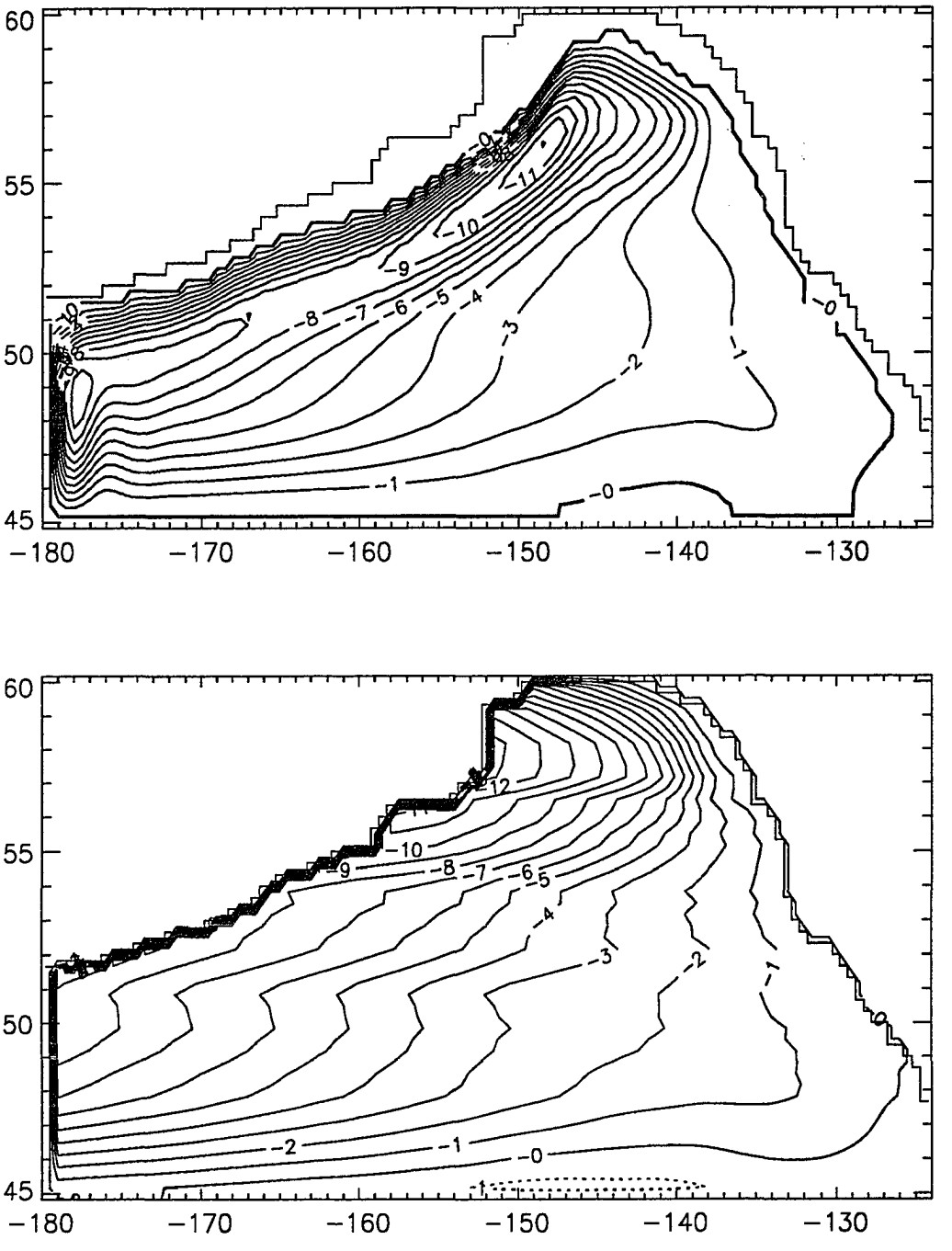

Figure 4.2 Contour plot of the stream function at year 10 (upper) and the Sverdrup circulation (lower).

Reproduced with permission of the copyright owner. Further reproduction prohibited without permission.

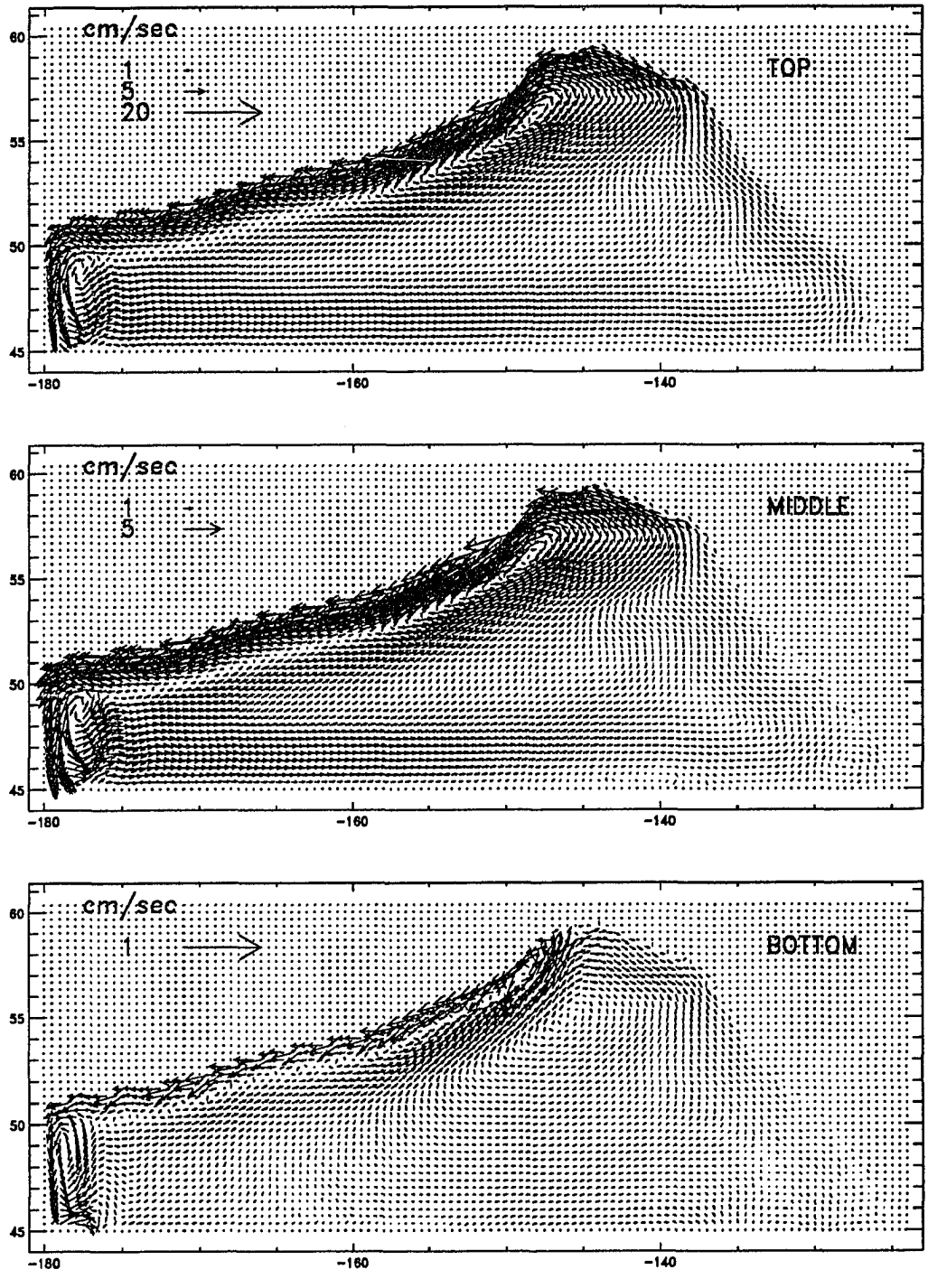

Figure 4.3 Velocity vector plots of top, middle, and bottom layers at year 10.

Reproduced with permission of the copyright owner. Further reproduction prohibited without permission.

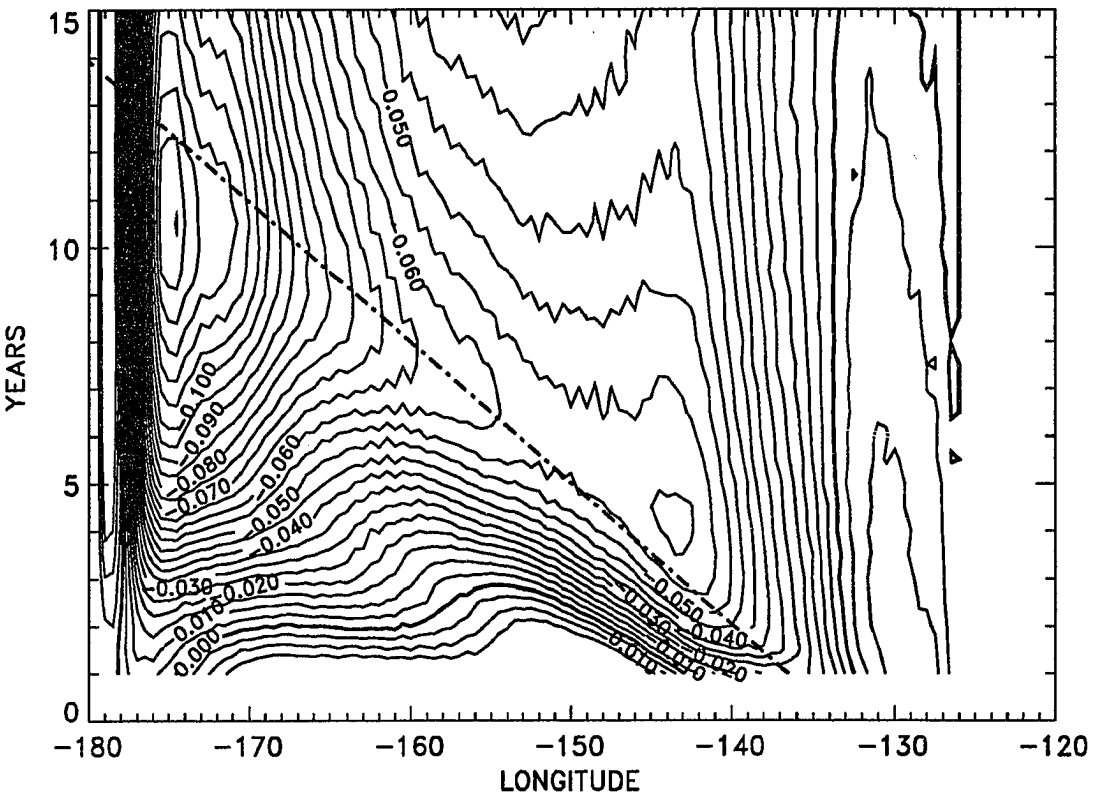

Figure 4.4 Contour plot of the zonal velocity of the bottom layer along 48° 20′ N in longitude-time space. The chain-dotted line indicates the predicted location of baroclinic Rossby wave with a phase speed of 0.8 *cm/sec.*

and stratified ocean to the wind. Small perturbations to the stationary state in a flat-bottom ocean makes it possible to decompose the current into modes which satisfy the same wave equation with different 'effective depth', h, characteristic of each mode. The effective depth of barotropic mode is the actual depth of the ocean and is only about 1 m at most for the first baroclinic mode (Lighthill 1969).

Knowing the effective depth, one can estimate the speed of the baroclinic Rossby wave. Rossby waves excited by a predominantly zonal distribution of wind stress have nearly westward

Reproduced with permission of the copyright owner. Further reproduction prohibited without permission.

phase velocity C_x given by

$$C_x = \frac{\beta}{k^2 + (f^2/gh)} \tag{4.2}$$

where k is the zonal wavenumber, β is the meridional gradient of the Coriolis parameter f, and h is the effective depth. The maximum phase speed of baroclinic Rossby wave is

$$C_x^{max} = \beta gh/f^2 \tag{4.3}$$

and is about 1 *cm/sec* at high latitude and 10 *cm/sec* near 20° N with a typical value of h=1 *m*. The maximum phase speed of baroclinic Rossby waves is also equal to the maximum group speed and the waves are called 'non-dispersive baroclinic Rossby waves' (Lighthill 1969).

From (4.3) and $C_x^{max} = 0.8$ *cm/sec*, one can estimate the effective depth and it is about 0.64 *m* in this model. It can also be compared with the effective depth computed from the initial density gradient and thicknesses of layers. The effective depth of the first baroclinic mode of which the eigenfunction has only one zero in vertical is given by

$$h = \frac{\Delta\rho}{\rho_0}\frac{D_1 D_2}{D_1 + D_2} \tag{4.4}$$

where, $\Delta\rho$ is the density difference between two layers, ρ_0 the mean density, D_1 the thickness of the upper layer, and D_2 the thickness of the lower layer. As is shown in the last column of Table 4.1, two effective depths are possible from two density jumps between layers. The effective depth 0.67 *m* which is computed from D_1=d_1+d_2 and D_2=d_3 is close to 0.64 *m* estimated from the group speed of the first baroclinic Rossby wave in the model. A baroclinic Rossby wave which can result from the density gradient between the first and second layer is not clear in Figure 4.4 and it can be understood in terms of the effective depth and propagating speed. This wave will have a group speed of only a third of that by h=0.67 *m* according to (4.3) and Table 4.1 and consequently would be subject to more dissipation.

Reproduced with permission of the copyright owner. Further reproduction prohibited without permission.

Section 4.3 10-layer Case

This case now includes thermohaline forcing along with wind. The gulf is assumed 1200 m deep and any shallower depths are designated as land. The Laplacian eddy coefficient in the sponge layer is 1×10^8 cm^2/sec for both viscosity and diffusivity and biharmonic eddy coefficient in the interior are -1×10^{19} and -3×10^{19} cm^4/sec for momentum and diffusion, respectively. Vertical viscosity is now reduced to 1 cm^2/sec and vertical diffusivity is 0.3 cm^2/sec as before.

A thermohaline information at the ocean surface takes an order of thousand years to reach the deep portion of a ocean because of the small vertical diffusivity. For example, the diffusion time scale H^2/κ is 5000 years with H=4 km and κ=1 cm^2/sec. Therefore, a reproduction of an observed three-dimensional density field starting from a homogeneous ocean by wind and thermohaline forcing is not a good approach. A use of longer time step for the density field is one way of speeding up the spin-up process. This is possible because the density field changes more slowly in time than does the velocity field. Bryan (1984) further extended this method by using longer time steps in deep layers. However, this approach of different time stepping is valid only for a steady-state solution.

Semtner and Chervin (1988) adopted the robust-diagnostic method (Sarmiento and Bryan 1982) for a fast spin-up to the observed density field in their world ocean circulation model. The model density field is forced to the observed density field by the help of a Newtonian type forcing term in the temperature and salinity equations.

$$-\frac{1}{\gamma}(T - T_o) \quad \text{and} \quad -\frac{1}{\gamma}(S - S_o) \tag{4.5}$$

where T_o and S_o are the observed values and γ is the restoring time scale. When γ is small, the predicted temperature (T) is almost equal to the observed temperature (T_o) and the model

Reproduced with permission of the copyright owner. Further reproduction prohibited without permission.

becomes a pure diagnostic model as in Chapter 2. When γ is large, this term is negligible and the model becomes a prognostic model. Semtner and Chervin (1988) could spin up the world ocean in a decade by gradually increasing the restoring time scale in time. After the spin-up process, Semtner and Chervin (1988) removed the robust-diagnostic term from layers in the upper 1000 m for a study of transient motions. A short time scale (a month) was kept throughout the integration in the surface layer to keep the surface density close to the observed value as a thermohaline forcing.

The robust-diagnostic approach is also adopted for the spin-up process in this thesis. One year of restoring time scale is used during the first two years in all layers except for the surface layer where 30 days of restoring time scale is kept throughout the integration. Wind stress is linearly increased during the first year and remains constant after reaching its normal strength at the end of the first year. The initial conditions are horizontally homogeneous temperature and salinity fields and no motion.

The kinetic energy shows a stationary state after 3 years of integration, which is 1 year after the removal of the robust-diagnostic term (Figure 4.5). Fluctuations with a period of about 70 days are also seen to appear beginning from the third year of integration (Figure 4.5). The mean circulation as a cyclonic gyre is established (upper panel of Figure 4.6). A wide and weak eastward flow turns more and more to the north as it approaches North America. A boundary current is formed about 140° W at the head of gulf and flows westward along the coast of Alaska. The overall strength of the gyre is 6–7 Sv and large transports associated with eddies are found mainly in the upstream region of the Alaska Stream. There is also an indication of large meandering near the coast of North America as can be seen by the contour line of –1 Sv.

The lower panel of Figure 4.6 shows an instantaneous picture of the perturbation stream function. This pattern stays almost unchanged in time except for the westward propagation of eddies. Eddies are concentrated along the Alaska Stream from around 144° W to the western

Reproduced with permission of the copyright owner. Further reproduction prohibited without permission.

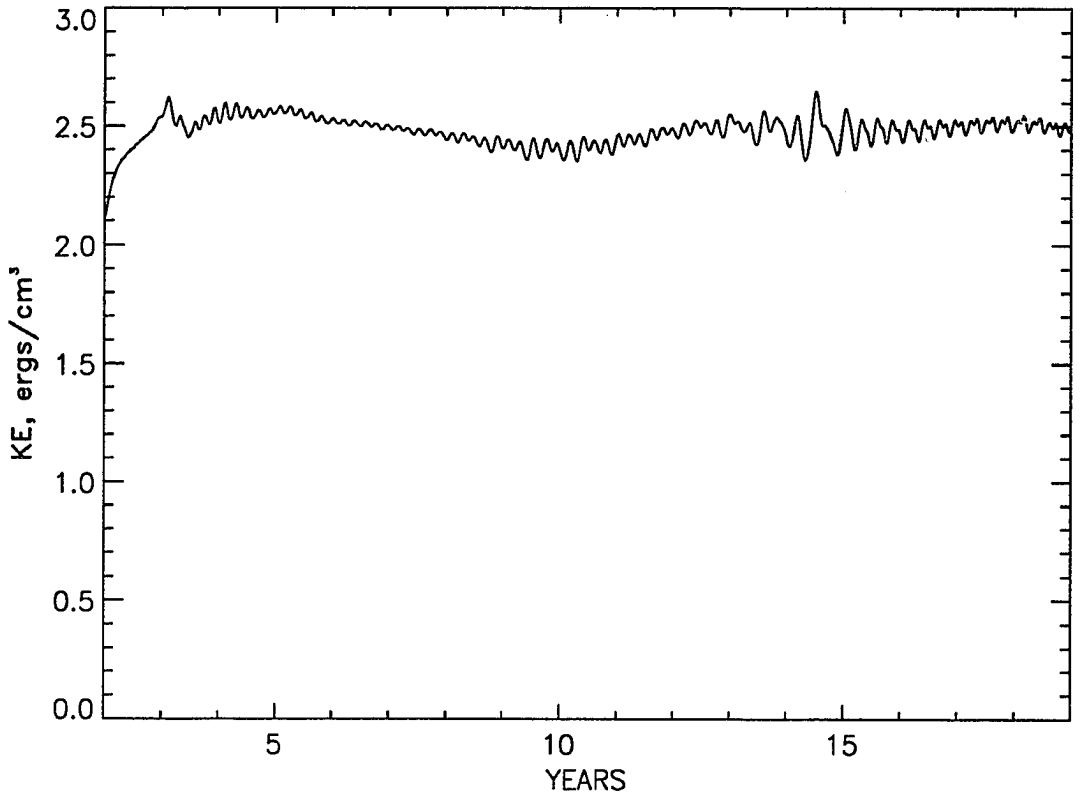

Figure 4.5 Basin-averaged kinetic energy (*ergs/cm³*).

boundary and become weaker in the downstream direction. There is no indication of eddies reentering the interior from the sponge layer near the western boundary. The wavelength determined by the number of eddy pairs (9 cyclonic and anticyclonic eddy pairs) and the length (2160 km) is about 240 km.

From the time series of the stream function at seven monitoring points, one can estimate the periods and variabilities of the eddy activity at various points of the gulf (Figure 4.7). The transport fluctuation at CI (Cook Inlet) is the largest of the seven points, almost 5 Sv, and decreases to about 1 Sv at CK and less than 1 Sv at DS. At the other monitoring points which

Reproduced with permission of the copyright owner. Further reproduction prohibited without permission.

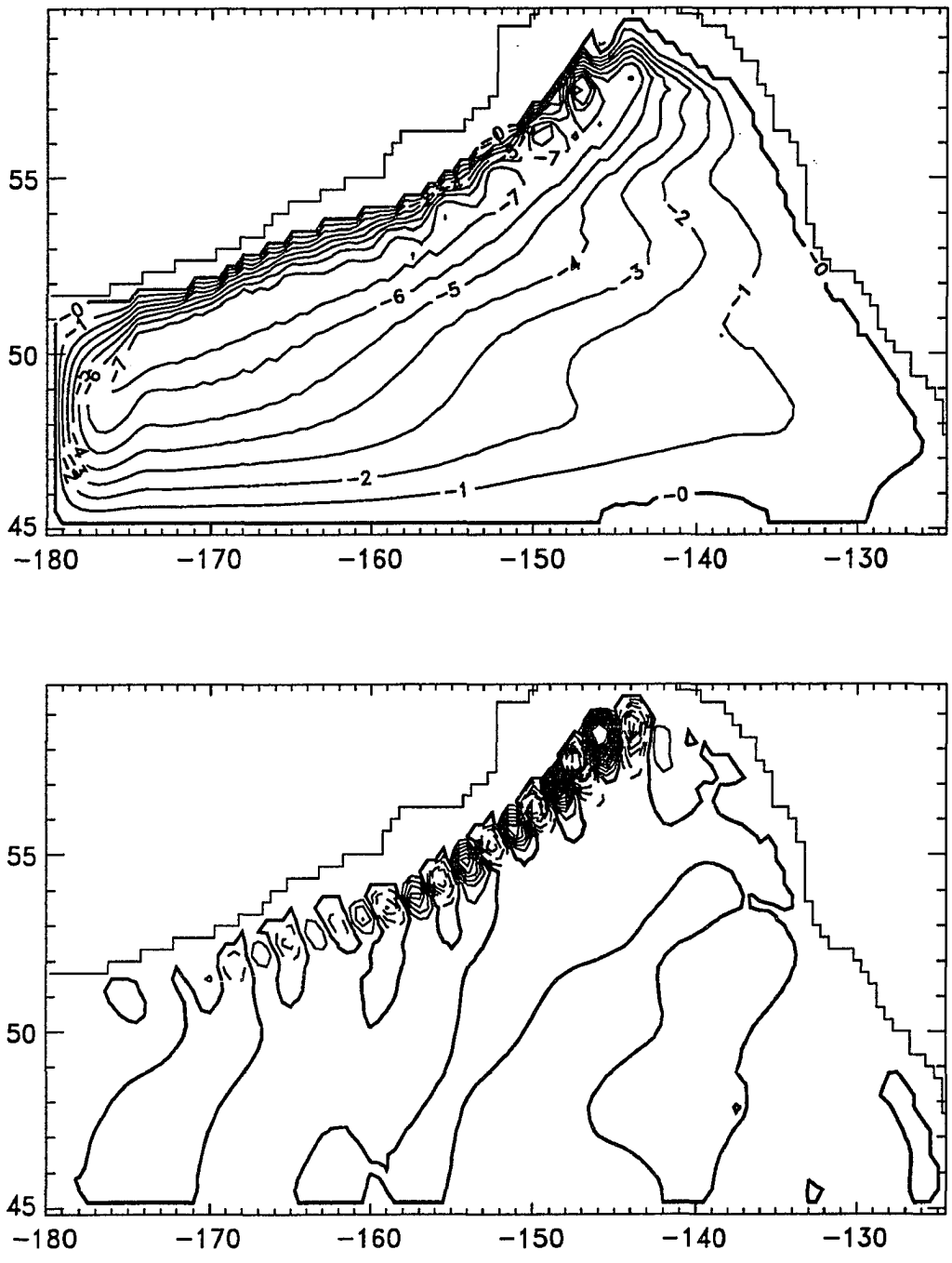

Figure 4.6 Contour plots of the stream function at year 10 (upper) and of the perturbation field (lower) from the 2-year mean from 9–11. Contour interval of the bottom figure is 0.2 Sv.

Reproduced with permission of the copyright owner. Further reproduction prohibited without permission.

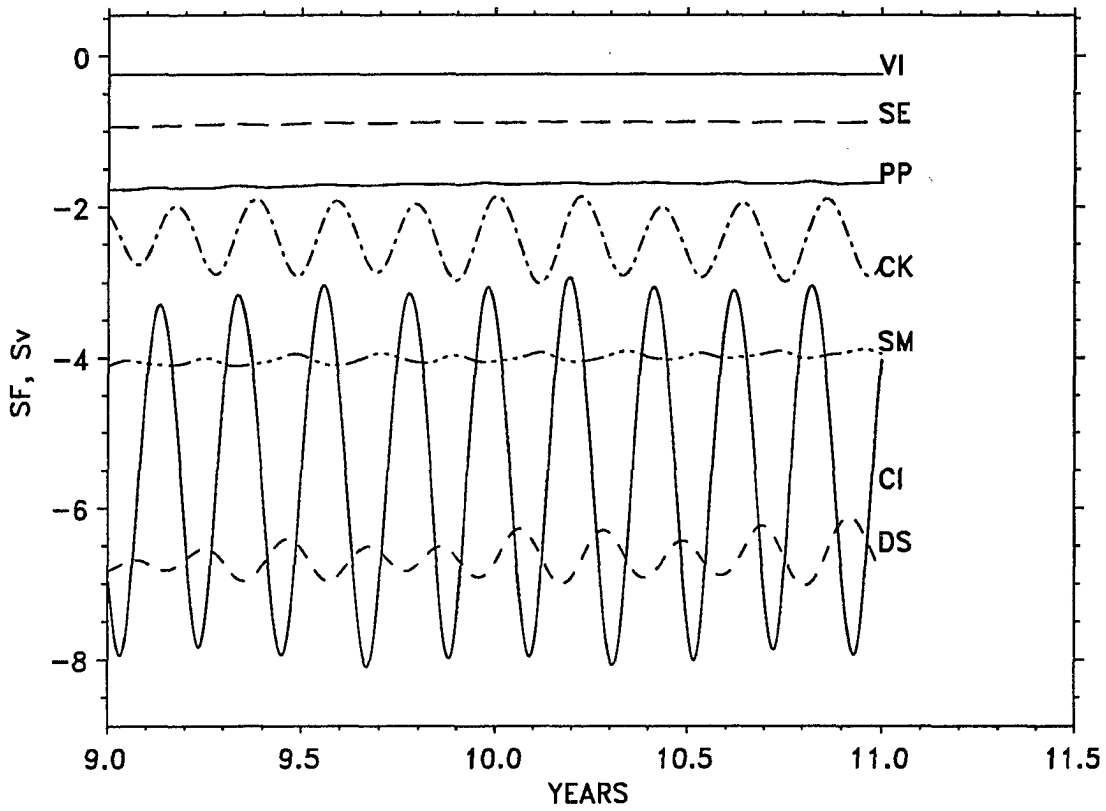

Figure 4.7 Time series of the stream function (SF) at monitoring points for year 9–11 (see Figure 3.3 for the locations).

are located outside of the Alaska Stream (VI, SE, SM, and PP), the ranges of the fluctuations are almost zero. Period of these fluctuations at CI, CK, and DS is about 75 days. Although a phase speed of about 0.037 *m/sec* can be obtained from the period of 75 days and the wavelength, a time-longitude plot is also shown to show the propagation characteristics of these eddies (Figure 4.8). The two-year mean over the same period as Figure 4.7 is subtracted from the stream function. The eddies are mainly seen in the Alaska Stream, 160°–155° W at this latitude, and propagate westward at a phase speed of about 0.04 *m/sec*. The wavelength is about 250 km with the period of about 75 days.

The westward propagation of phase indicates that these eddies are Rossby waves (internal

Reproduced with permission of the copyright owner. Further reproduction prohibited without permission.

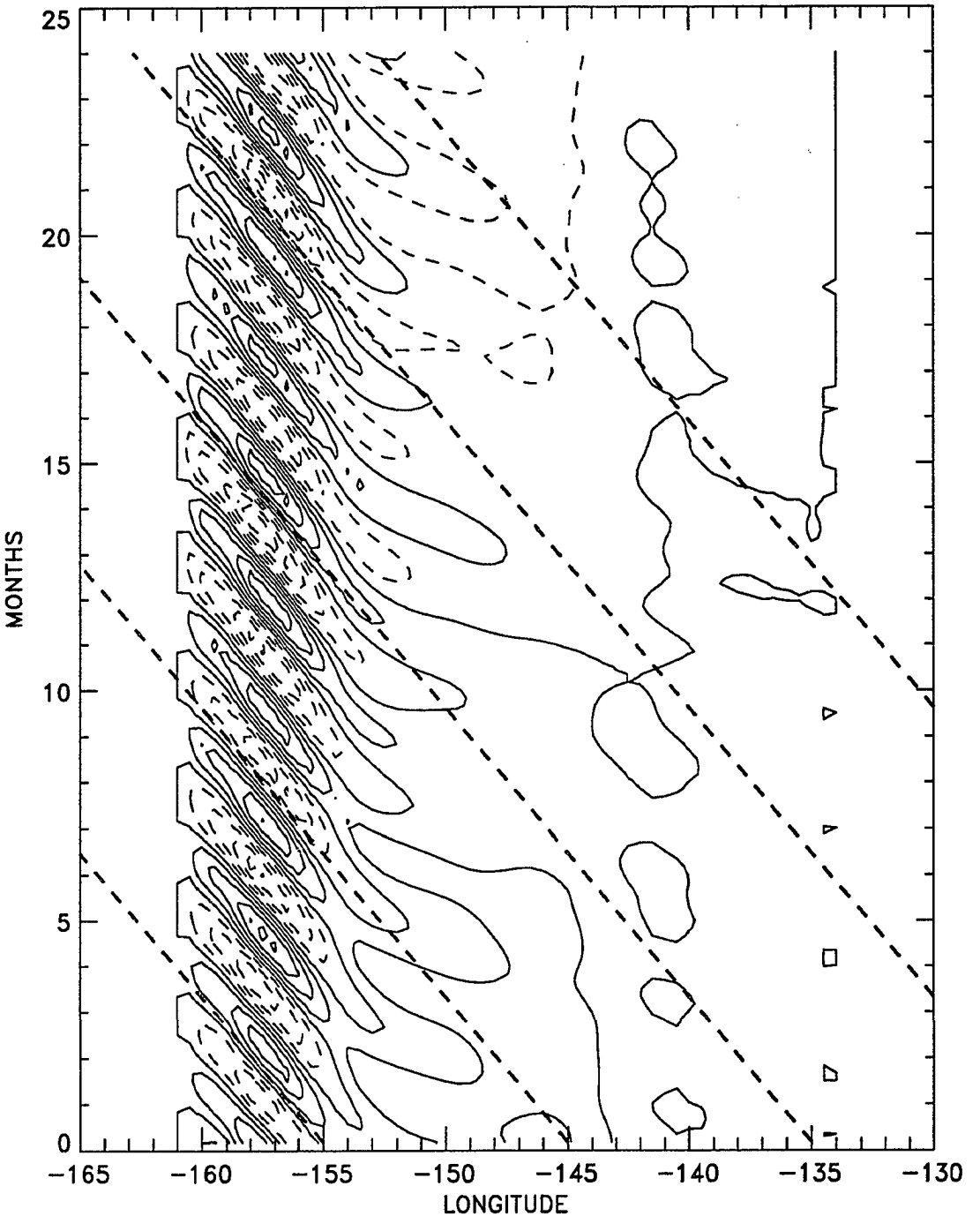

Figure 4.8 Time-longitude plot of perturbation stream function at 54° N. Dashed lines are 0.04 m/sec and contour interval is 0.2 Sv.

Reproduced with permission of the copyright owner. Further reproduction prohibited without permission.

Kelvin waves also propagate westward along the sloping boundary, but their phase speed is on the order of 1 *m/sec*). The phase speed of 0.04 *m/sec* is too fast for these eddies to be considered as baroclinic Rossby waves whose phase speed is only about 0.01 *m/sec* at this latitude. Therefore, it is most likely that these eddies are barotropic Rossby waves. Cummins and Mysak (1988) observed a similar high frequency fluctuations (100 days and 330 km) in their flat-bottom case and identified them as barotropic Rossby waves. Compared to their period and wavelength, the values found here are smaller but the phase speed remains the same. A dispersion relation of the zonally propagating barotropic Rossby waves is

$$\omega = -\frac{\beta}{k} \tag{4.6}$$

and gives a period of 135 days for waves with zonal wavelength of 250 km at 54° N, which is almost twice of the observed period of 75 days.

Since the eddies are propagating within the Alaska Stream, it is natural to consider the Doppler shift effect as a possible explanation for this discrepancy. If the observed frequency is considered as being Doppler-shifted by the westward flowing Alaska Stream, then the mean current of about 2 *cm/sec* would be enough to get the observed period. However, the mean speed of the model Alaska Stream is greater than 5 *cm/sec*. The effect of this strong current can be better understood in terms of phase speed rather than the frequency. The Doppler-shifted or observed phase speed (C_o) to the stationary observer is the sum of the speed of the mean current (C_m) and the intrinsic speed (C_i).

$$C_o = C_m + C_i \tag{4.7}$$

If C_o is –4 *cm/sec* and C_m is –5 *cm/sec*, then C_i is +1 *cm/sec*, which means that the barotropic Rossby wave propagates eastward rather than westward.

Another factor which is not included in the discussion so far is the contribution of the gradient of the relative vorticity to the potential vorticity. The relative vorticity is small

Reproduced with permission of the copyright owner. Further reproduction prohibited without permission.

compared to the planetary vorticity by the order of Rossby number (the ratio of relative vorticity to the planetary vorticity is Rossby number). On the other hand, the gradient of the relative vorticity is not necessarily small compared to the gradient of the planetary vorticity, β (Pedlosky 1982). The relative magnitude of the latter to the former is estimated by a nondimensional parameter

$$\frac{\beta L^2}{U} \tag{4.8}$$

As an example, this parameter is on the order of 1 for motions with characteristic scales of U=5 *cm/sec* and L=100 km (β=1 $\times$ 10^{-13} cm^{-1} sec^{-1}).

The model Alaska Stream has such scales that the meridional gradient of the relative vorticity can be no longer ignored. Now, the governing equation of the small perturbation (ψ) in a barotropic zonal mean flow, $U(y)$, is (Leblond and Mysak. 1978)

$$\left(\frac{\partial}{\partial t} + U\frac{\partial}{\partial x}\right)\nabla_h^2\psi + \left(\beta - U''\right)\frac{\partial \psi}{\partial x} = 0 \tag{4.9}$$

where the prime denotes the differentiation with respect to y. A plane wave of the form

$$\psi = \Psi e^{i(kx+ly-\sigma t)} \tag{4.10}$$

is a solution to (4.9) if

$$(C-U)\left(k^2+l^2\right) + \left(\beta - U''\right) = 0 \tag{4.11}$$

or

$$C = U - \frac{\beta - U''}{k^2+l^2} \tag{4.12}$$

in terms of the phase speed. This is a dispersion relation of the barotropic Rossby waves in the presence of the zonal mean flow and the observed phase speed consists of three components; advection by mean flow, intrinsic propagation by β effect (C_p), and propagation by the effect of

Reproduced with permission of the copyright owner. Further reproduction prohibited without permission.

the gradient of the relative vorticity (C_r). Assuming $k>>l$, denote each component as following

$$C_o = U + \left(-\frac{\beta}{k^2}\right) + \frac{U''}{k^2}$$
$$= C_m + C_p + C_r \qquad (4.13)$$

For a westward flowing jet like the Alaska Stream, C_r is positive (assuming a sinusoidal form) whereas the other two terms are negative. Therefore, the observed phase speed (C_o) can be either westward or eastward depending on the relative magnitude of these three speeds.

Estimates of the relative vorticity and corresponding propagation speed are made along 157.5° W from the vertical average of the time-mean zonal velocity over two years (year 9–11). The meridional gradient of the relative vorticity is almost zero in the interior but is negative and exceeds the magnitude of β in the Alaska Stream (upper panel of Figure 4.9). Therefore, the meridional gradient of the relative vorticity cannot be ignored in the Alaska Stream. The gradient of the total vorticity, $\beta - U''$, changes from the positive value ($\sim\beta$) in the interior (south of 54° N) to the large negative value at the center of the jet. In terms of the phase speed, C_r is positive (eastward) and partially cancels the negative (westward) C_m within the jet. However, the westward advection by the mean flow C_m is not totally cancelled out by C_r and the residuals plus C_p results in the enhanced westward speed. An average of C_o over 5 grid points (1° 40′) within the jet is about –3.6 *cm/sec* and agrees well with the phase speed of –4 *cm/sec* obtained from the time-longitude plot (Figure 4.8). The intrinsic phase speed of the barotropic Rossby waves is then about 2.1 *cm/sec* and the intrinsic period is about 135 days.

A question, then, arises about the result of Cummins and Mysak (1988). Cummins and Mysak (1988) could satisfy the dispersion relation of the barotropic Rossby waves, equation (4.6) (note (4.6) is a special case of (4.13)) . A possible explanation comes from C_m and C_r. These phase velocities have opposite signs and tend to cancel each other (C_m is negative and C_r is positive for a westward jet and vice versa for a eastward jet). In our case, C_m/C_r is about

Reproduced with permission of the copyright owner. Further reproduction prohibited without permission.

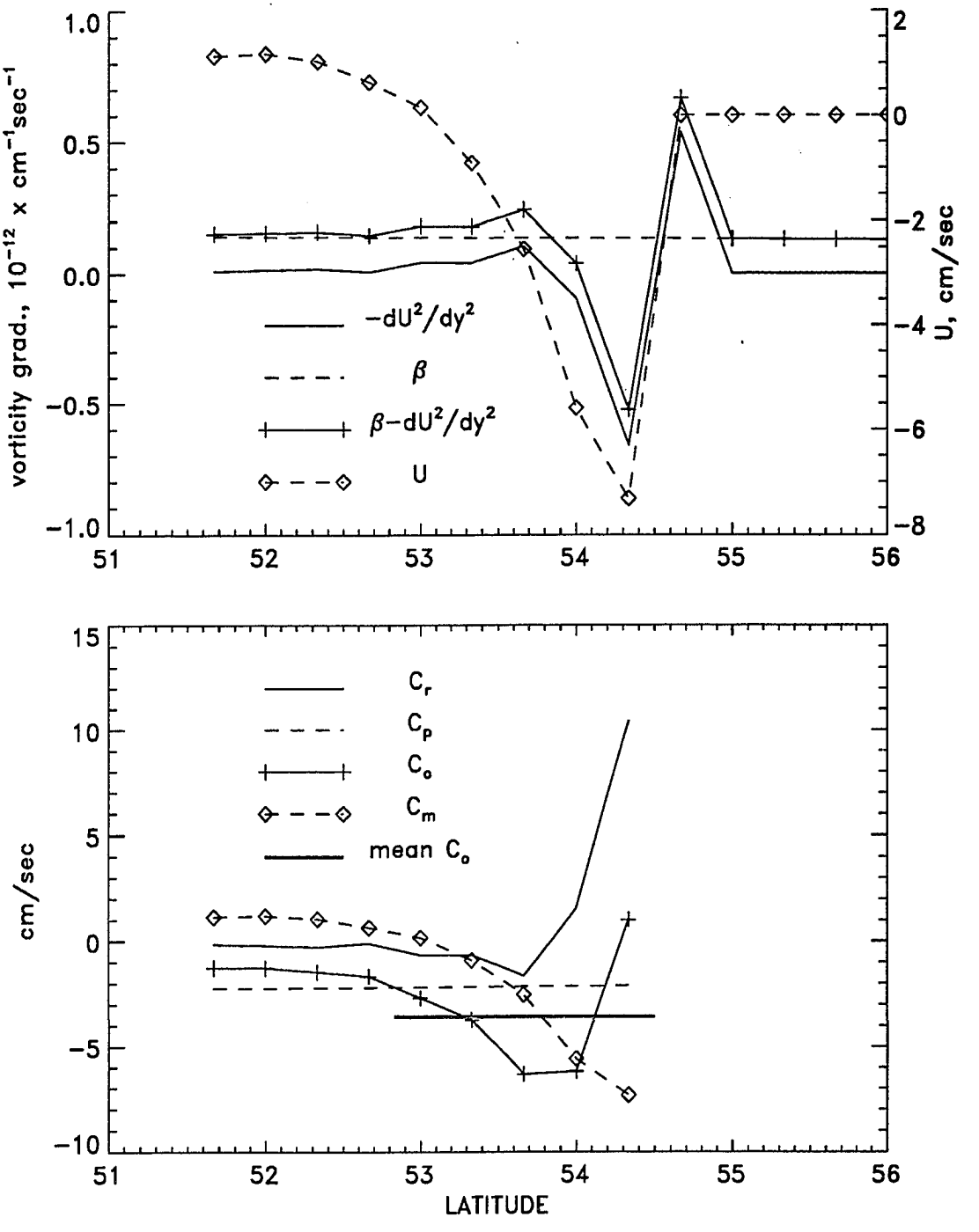

Figure 4.9 Meridional gradients of the total, relative, and planetary vorticities and vertically averaged zonal velocity U (upper). Phase speeds of a barotropic Rossby wave defined by (4.13) (lower). The thick bar indicates the average of C_o over the distance which it spans.

Reproduced with permission of the copyright owner. Further reproduction prohibited without permission.

–1.8 resulting in the increased westward phase speed C_o over C_p which is about –2.1 *cm/sec.* The ratio of C_m to C_r is proportional to the square of the ratio of the width of the jet L_m to the zonal wavelength of eddies L_e.

$$\frac{C_m}{C_r} = \frac{Uk^2}{U''} \propto \frac{L_m^2}{L_e^2} \tag{4.14}$$

On the other hand, C_m/C_r would be about –1 if L_e is increased from our value of 250 km to 330 km of Cummins and Mysak (1988) with a constant L_m. Therefore, C_m and C_r of Cummins and Mysak (1988) would cancel each other. Consequently, the dispersion relation (4.6) and (4.13) are satisfied at the same time. Although this analysis needs a detailed information about the current structure of Cummins and Mysak (1988) for an accurate estimation, it shows a possibility of the cancellation of these two effects.

Empirical orthogonal function (EOF) analysis was done for two years of stream function data (year 9–12) sampled at every other point in both horizontal directions. The first two modes explain 94.0 % of variability (Table 4.2). According to the statistical analysis by North *et al.* (1982), individual EOFs of similar variance are interpreted as dependent components of a set of EOFs that together describe the same statistical process (White and Tabata 1987). In this case, the first two EOFs, which explain 50.3 % and 43.7 % of the total variance, respectively, are therefore not statistically independent. Although they are orthogonal to each other (i.e., linearly independent), they are a part of very similar statistical processes. This is further supported by the fact that they both have a same period of about 75 days in time function (Figure 4.10) and a similar spatial pattern of eigenvectors. The period is equal to the period of eddies in the Alaska Stream which was determined from Figure 4.7 and 4.8 and the spatial distributions of eigenvectors also confirm that these two modes represent the same eddy activities.

Reproduced with permission of the copyright owner. Further reproduction prohibited without permission.

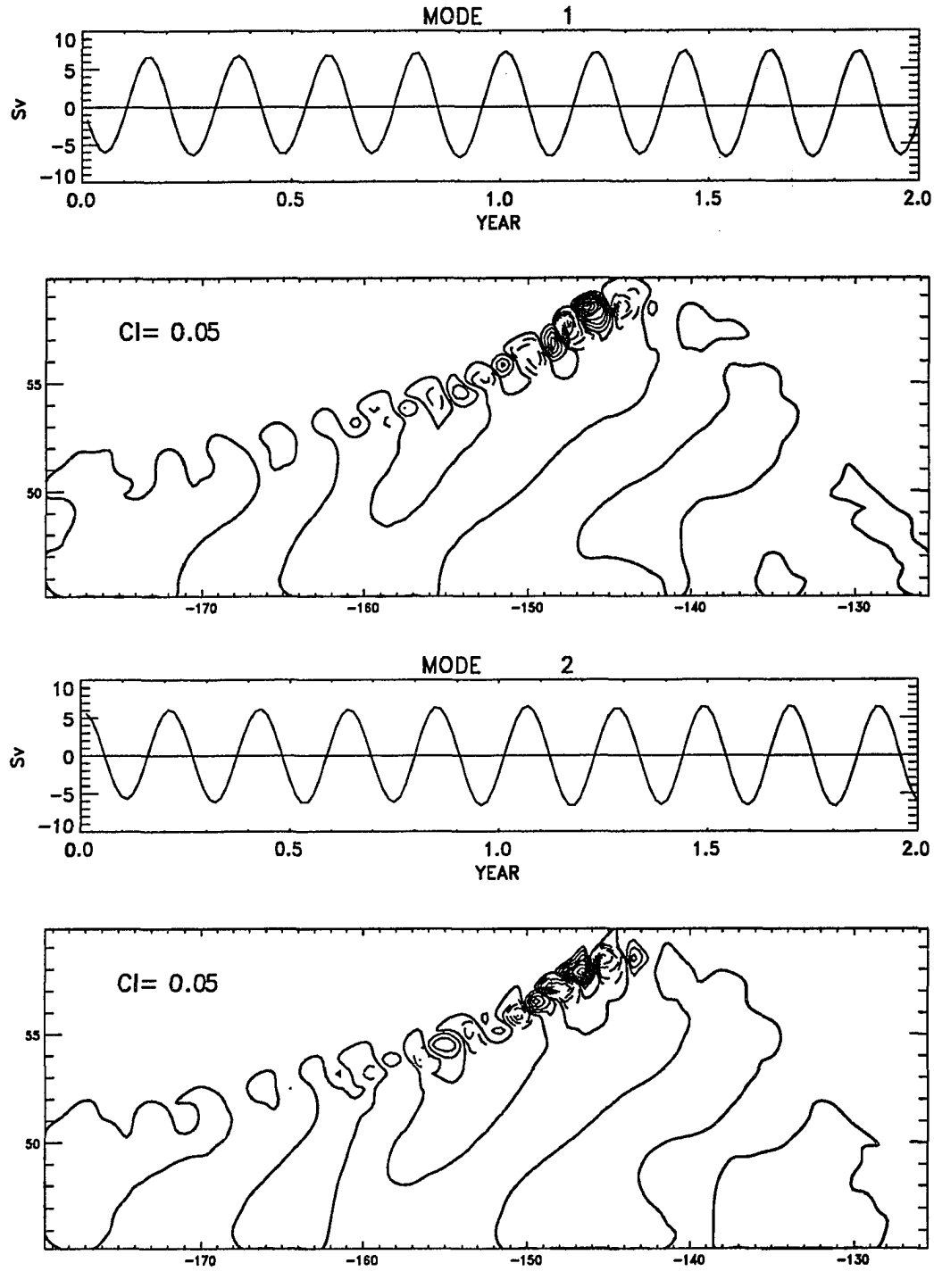

Figure 4.10 Time coefficients and eigenvectors of the first two EOF modes. Zero contour lines are denoted by a thick solid line and other solid lines are for positive values and dashed lines are for negative values.

Reproduced with permission of the copyright owner. Further reproduction prohibited without permission.

Table 4.2 Percentages explained by the first four EOF modes of stream function data of year 11.

Mode	1	2	3	4	5
Variance Explained(%)	50.3	43.7	2.9	0.8	0.7
Cumulative %	50.3	94.0	96.9	97.7	98.4

From the above observations, it is clear that most of eddy activities are large in the Alaska Stream and it can be further clarified by a spectral analysis. Spectral analysis was done for 640–day stream function data all over the region. Distribution of power spectral density (PSD) of the stream function in the frequency domain is first examined. Figure 4.11 shows the spectrum at five points from 158° W to 138° W along a constant latitude line (54° N). At the westernmost point, 158° W, which is located at the center of the eddy activity (Figure 4.8), dominant peaks are found at 70–80 day periods. This peak is also found at 153° W but disappears at points farther east. This peak is certainly associated with eddies and its absence in the interior is consistent with Figure 4.8.

Distribution of PSD of the stream function of the 80–day period was calculated in the Gulf of Alaska at every horizontal grid points (Figure 4.12). It has large values along the Alaska Stream as expected because this period is associated with eddies in the Alaska Stream. The maximum PSD is found at 58° N, 147° W and gradually decreases downstream. The spectral density at 170° W is about 3 orders smaller compared to the maximum value. The spatial distribution of the phase of the 80 day period waves relative to 158° W, 54° N has the phase ranging from –180 ° to 180° with a contour interval of 30° (Figure 4.13). In general, the phase increases from east to west, consistent with the propagation of Rossby waves, not only in the Alaska Stream but also in the interior although the signal in the interior has a far smaller

Reproduced with permission of the copyright owner. Further reproduction prohibited without permission.

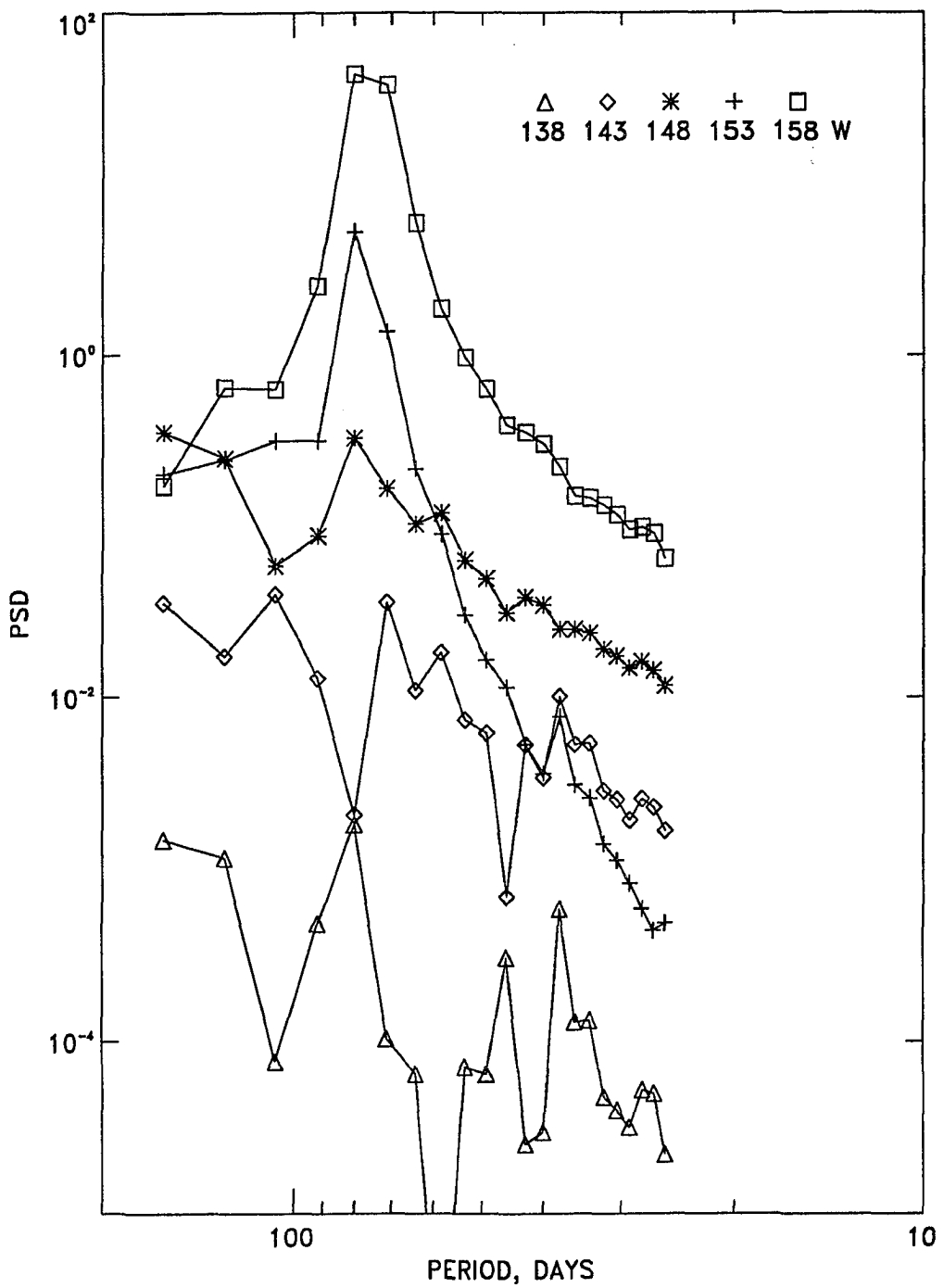

Figure 4.11 Spectrum of stream function at five points along 54° N.

Reproduced with permission of the copyright owner. Further reproduction prohibited without permission.

Reproduced with permission of the copyright owner. Further reproduction prohibited without permission.

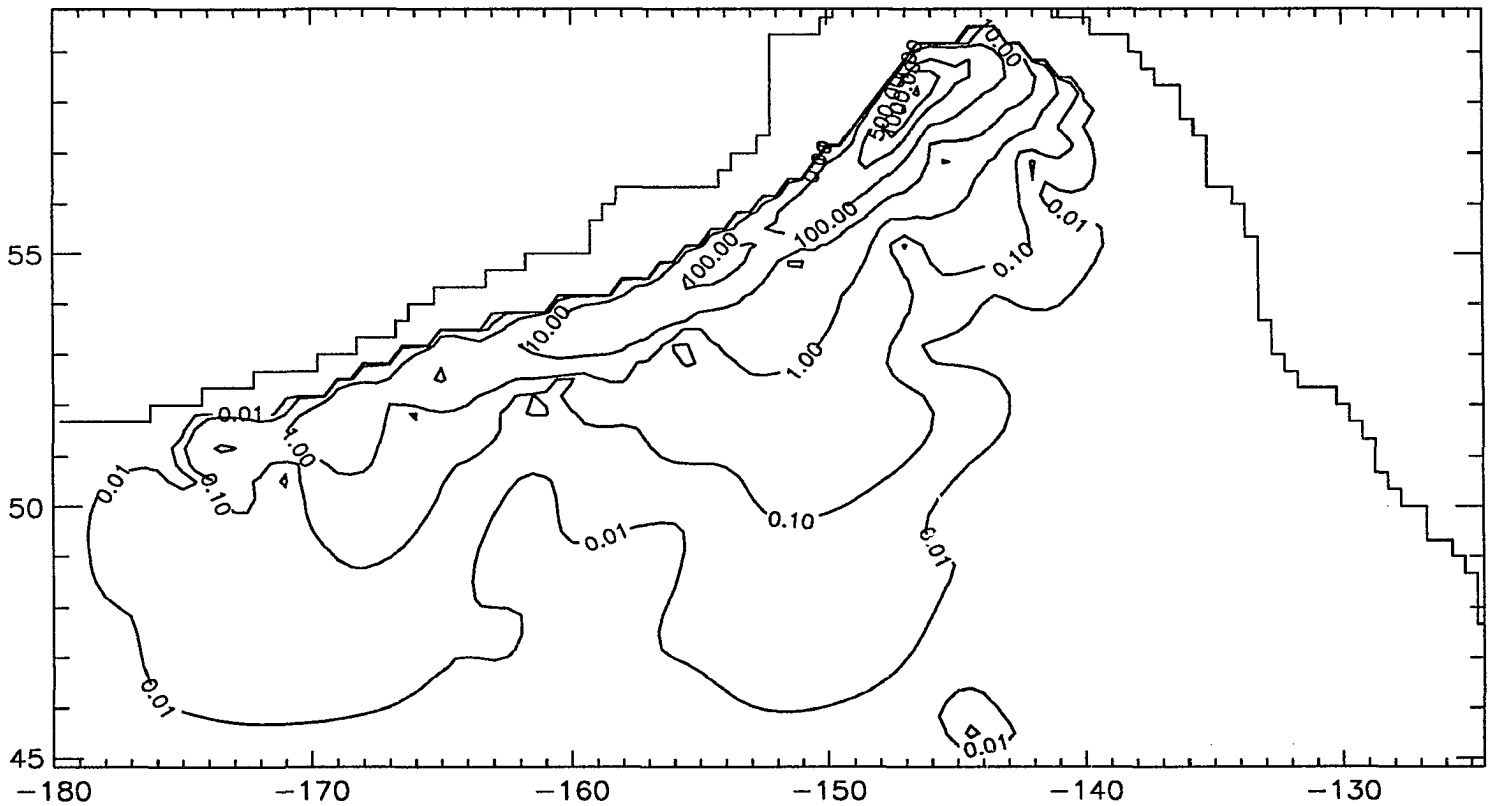

Figure 4.12 Distribution of spectrum of 80–day period. Note that contour intervals are not regular.

Reproduced with permission of the copyright owner. Further reproduction prohibited without permission.

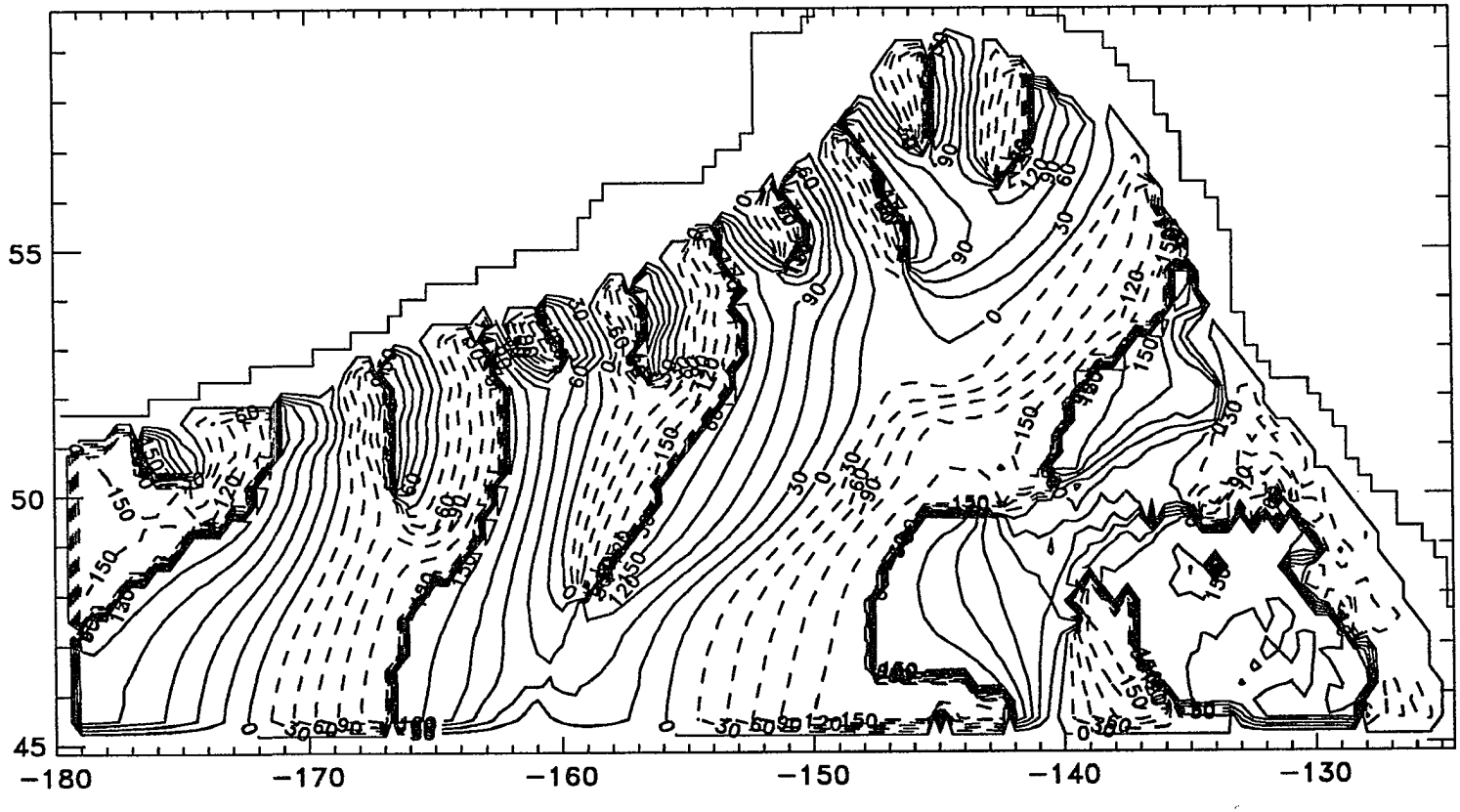

Figure 4.13 Phase (in degrees) of 80–day period signal relative to 54° N, 158° W.

amplitude than in the Alaska Stream (Figure 4.12). The wavelength, which can be estimated from the distance between a packing of contour lines where the phase change occurs from 180 to –180, is again 200–300 km.

To examine a role of the instability as a generating mechanism of eddies, an analysis of energy is done. Of the causes responsible for eddies in the ocean, barotropic and baroclinic instabilities are most frequently quoted as primary sources. Barotropic instability occurs due to the horizontal shear in the mean flow and extracts energy from the kinetic energy of the mean flow while baroclinic instability depends on the vertical shear and extracts energy from the mean potential energy. Since papers by Charney (1947) and Eady (1949), the baroclinic instability has been the subject of great interest both in the study of atmosphere and ocean. Orlansky and Cox (1973) show that the Gulf Stream can be baroclinically unstable, and that the meanders observed in this current are probably a manifestation of unstable baroclinic waves.

A simple test to determine if a baroclinic instability is possible is to check if the rotational Froude number (or inverse Burger number), $F = \frac{f^2 L^2}{gH\Delta\rho/\rho}$ where $\Delta\rho$ is the characteristic density change in vertical direction, is less than 1 (Hart 1979). Under this circumstance, energy can be released from available potential energy to eddies. With f=1.18 $\times$ 10^{-4} sec^{-1}, $\Delta\rho/\rho$=10^{-3} and H=1200 m, perturbations with a length scale of L > 30 km satisfy the condition. So, a baroclinic instability can be expected although other factors also affect the baroclinic instability such as β–effect, friction, and horizontal shear of the basic flow. Since analytical solutions are not easily constructed when these effects are included into the continuously stratified model, two-layer model is often used to simplify the analysis while retaining the essential physics.

A necessary condition which can be derived from the two-layer model for a zonal mean flow is the change of sign of the meridional gradient of the mean potential vorticity in some places of the domain. However, this condition is applied only for the zonal flow. For an

Reproduced with permission of the copyright owner. Further reproduction prohibited without permission.

arbitrary flow the condition becomes

$$\frac{dQ}{dP} < 0 \tag{4.15}$$

where Q is mean potential vorticity and P is stream function (McWilliams 1977). Instead of using this condition, however, energy transfer terms between various energy forms are directly estimated.

In order to understand the dynamics of the eddies and their interaction with the time-mean circulation, the energy transfers are examined following Semtner and Mintz (1977). It is convenient to introduce the following notations:

$$\begin{aligned}
\langle c \rangle &= \frac{1}{V} \iiint c dv \\
\bar{c} &= \frac{1}{T} \int c dt \\
\tilde{c} &= \frac{1}{S} \iint c ds \\
c' &= c - \bar{c} \\
c^* &= c - \tilde{c}
\end{aligned} \tag{4.16}$$

where V is the volume, S the horizontal surface, T the integration time, and c the dummy variable.

Using these notations, mean kinetic energy and eddy kinetic energy are defined by

$$\begin{aligned}
\bar{K} &= \rho_0 \left\langle \frac{\vec{\bar{u}} \cdot \vec{\bar{u}}}{2} \right\rangle \\
K' &= \rho_0 \left\langle \overline{\frac{\vec{u}' \cdot \vec{u}'}{2}} \right\rangle
\end{aligned} \tag{4.17}$$

and mean available potential energy and eddy available potential energy are defined as in Han (1975).

$$\begin{aligned}
\bar{P} &= -\frac{1}{2} g \left\langle (\bar{\rho}^*)^2 \left(\frac{\partial \bar{\tilde{\rho}}}{\partial z} \right)^{-1} \right\rangle \\
P' &= -\frac{1}{2} g \left\langle \overline{(\rho'^*)^2} \left(\frac{\partial \bar{\tilde{\rho}}}{\partial z} \right)^{-1} \right\rangle
\end{aligned} \tag{4.18}$$

Reproduced with permission of the copyright owner. Further reproduction prohibited without permission.

By standard manipulations of the governing equations, one can show that the time-rates-of-change of the various energies are

$$\frac{\partial \bar{K}}{\partial t} = -\{\bar{K} : K'\} - \{\bar{K} : \bar{P}\} + \{\vec{\bar{\tau}}_w : \bar{K}\} - \{\bar{K} : \kappa\} - \{\bar{K} : A_M\} \tag{4.19}$$

$$\frac{\partial K'}{\partial t} = \{\bar{K} : K'\} + \{P' : K'\} - \{K' : \kappa\} - \{K' : A_M\} \tag{4.20}$$

$$\frac{\partial \bar{P}}{\partial t} = -\{\bar{P} : P'\} + \{\bar{K} : \bar{P}\} + other\ terms \tag{4.21}$$

$$\frac{\partial P'}{\partial t} = \{\bar{P} : P'\} - \{P' : K'\} + other\ terms \tag{4.22}$$

In the derivation, no normal velocities at all boundaries including the bottom and southern boundary are assumed. In other words, the linear zone implemented near the southern boundary is not taken into the consideration and the bottom is assumed flat. Also, all terms not directly related with the energy transfer between energy types are included in '*other terms*' of the mean potential and eddy potential energy equations. Exchanges between two energy types occur through the following terms

$$\begin{aligned}
\{\bar{K} : K'\} &= \left\langle \rho_0 \vec{\bar{u}} \cdot \left(\nabla \cdot \overline{\vec{u}'\vec{u}'} + \frac{\partial}{\partial z} \overline{w'\vec{u}'} \right) \right\rangle \\
\{\bar{P} : P'\} &= -\left\langle g\tilde{\rho}^* \left(\frac{\partial \tilde{\bar{\rho}}}{\partial z} \right)^{-1} \nabla \cdot \overline{\rho'^* \vec{u}'} \right\rangle \\
\{P' : K'\} &= -\langle \overline{\rho' g w'} \rangle \\
\{\bar{K} : \bar{P}\} &= \langle \bar{\rho} g \bar{w} \rangle
\end{aligned} \tag{4.23}$$

where ∇ is the horizontal gradient operator. The effects of wind driving and horizontal and vertical friction on the kinetic energy are

$$\{\vec{\bar{\tau}}_w : \bar{K}\} = \iint \vec{\bar{u}} \cdot \vec{\tau}_w ds$$

Reproduced with permission of the copyright owner. Further reproduction prohibited without permission.

$$\{\bar{K}:\kappa\} = \left\langle \rho_0 \kappa \vec{\bar{u}} \cdot \frac{\partial^2 \vec{\bar{u}}}{\partial z^2} \right\rangle - \{\vec{\bar{\tau}}_w : \bar{K}\}$$
$$\{\bar{K}:A_M\} = \left\langle \vec{\bar{u}} \cdot \vec{\bar{F}} \right\rangle$$
$$\{K':\kappa\} = \left\langle \rho_0 \kappa \vec{u}' \cdot \frac{\partial^2 \vec{u}'}{\partial z^2} \right\rangle$$
$$\{K':A_M\} = \left\langle \vec{u}' \cdot \vec{F}' \right\rangle \qquad (4.24)$$

where $\vec{F}$ represents the horizontal friction.

The analysis is done for two-year-long data of year 10–12. An estimate of four energy transfer terms and two dissipation terms of EKE which are averaged over the whole domain (Table 4.3) shows that baroclinic generation term $\{P':K'\}$ provides more energy to the eddies than the barotropic generation term $\{\bar{K}:K'\}$. Dissipation of EKE is equally divided by horizontal and bottom friction (a detailed analysis shows that the bottom friction constitutes almost all of the vertical friction term $\{K':\kappa\}$). Further insights into the energetics can be gained by looking at the horizontal variations in the energy transfer rates after making only a vertical integration. All terms show large values in the Alaska Stream so that they are again averaged over 3 degrees meridionally from the northern boundary (Figure 4.14). Large values in all terms are found 142°–150° W where the Alaska Stream is strong and eddy kinetic and eddy potential energies are also large. The baroclinic generation term is seen to be dominant along the Alaska Stream although the barotropic generation term becomes comparable to the baroclinic generation term in some places. One interesting thing in the barotropic generation term is that there are some locations where the eddy kinetic energy feeds the mean current indicated by the negative value.

Table 4.3 Basin-averaged values of the energy transfer and dissipation terms.

	$\{\bar{P}:P'\}$	$\{P':K'\}$	$\{\bar{K}:K'\}$	$\{\bar{K}:\bar{P}\}$	$\{K':A_M\}$	$\{K':\kappa\}$
10^{-6} ergs/cm^2/sec	1.12	0.22	0.03	2.37	-0.12	-0.13

Reproduced with permission of the copyright owner. Further reproduction prohibited without permission.

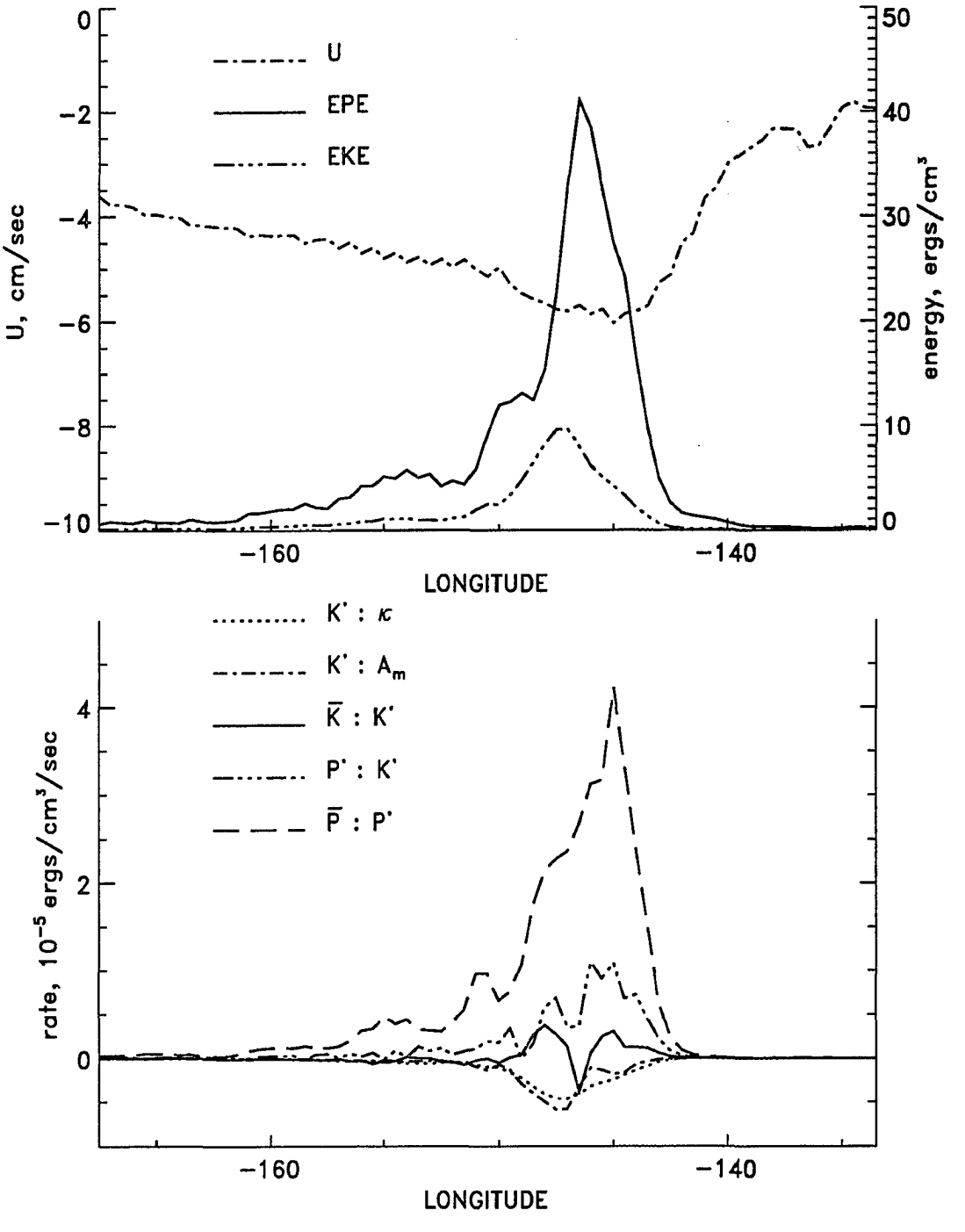

Figure 4.14 Zonal distributions of the meridionally-averaged 2nd layer zonal velocity (U), EPE, EKE, the energy transfer terms, and dissipation terms. The averaging is done over 3 degrees from the northern boundary.

Reproduced with permission of the copyright owner. Further reproduction prohibited without permission.

There is one more piece of evidence that these eddies are due to baroclinic instability. In Figure 4.15 meridional velocities at the center of the eddy activity are contoured in time-depth space to show the phase change in depth. The surface eddy signals lag behind about a week (30°) those at the bottom so that the lines of constant phase slope eastward with height from the bottom. This slope is leaning against the vertical velocity profile of the mean current which is sloping westward with height and this is exactly the necessary condition for baroclinic instability (Pedlosky 1982).

Reproduced with permission of the copyright owner. Further reproduction prohibited without permission.

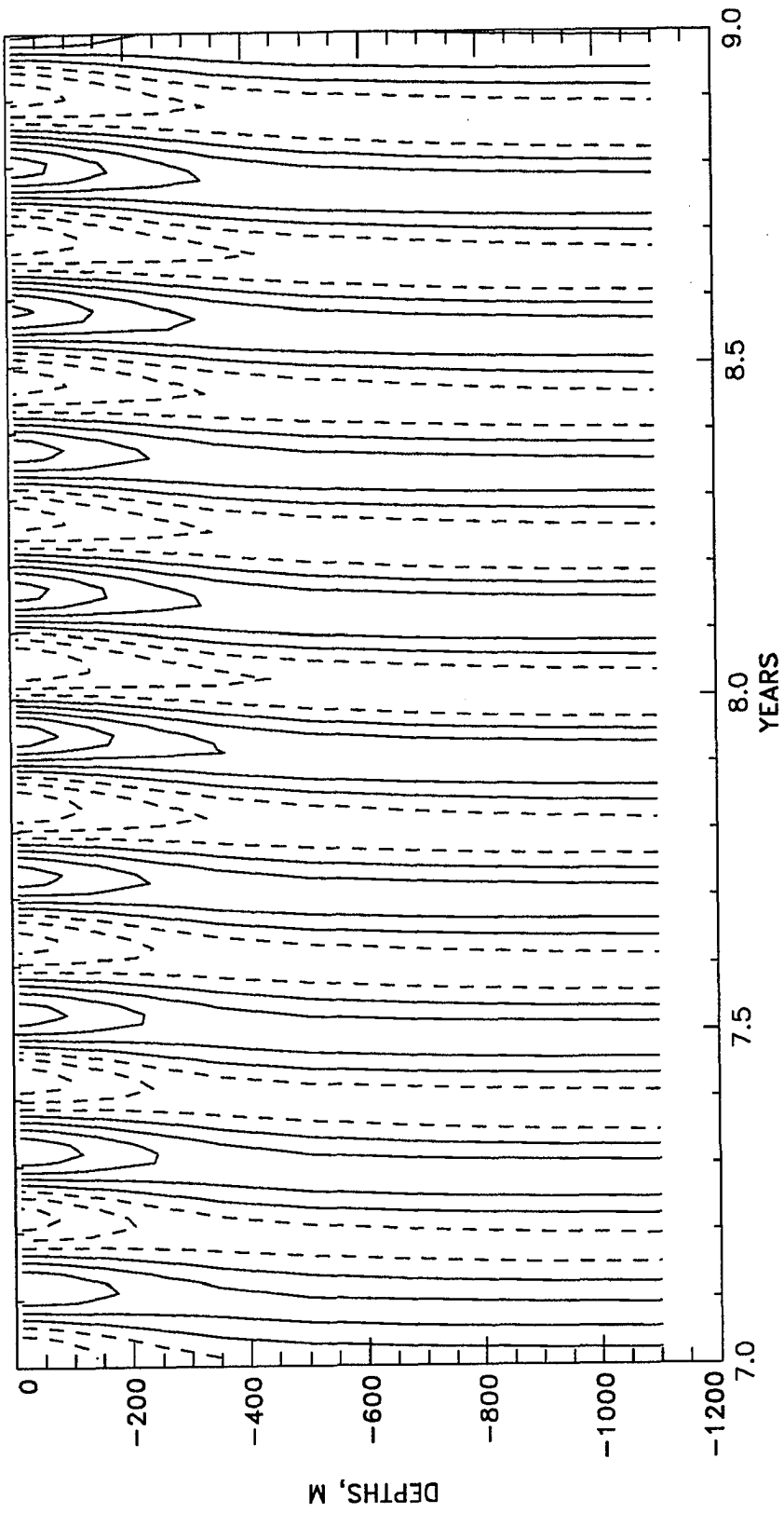

Figure 4.15 Time-depth plot of perturbation meridional velocity at 54° N, 156° 45′ W. Contour interval is 1 cm/sec.

Reproduced with permission of the copyright owner. Further reproduction prohibited without permission.

Section 4.4 Topography Case

Bottom topography is now included in the model and the number of vertical layers is increased to 20. The spin-up processes, thermohaline forcing and the boundary conditions are applied in the same way as in the flat–bottom case. The Laplacian friction coefficient in the sponge layer is 6×10^7 cm^2/sec for both momentum and diffusion. Two runs with an identical configuration are tried, differing only in the biharmonic coefficients. The volume mean kinetic energy of the first run, with an biharmonic eddy viscosity of -8×10^{18} cm^4/sec and biharmonic diffusivity -2.4×10^{19} cm^4/sec, has an increasing trend in time and is about to blow up after 19 years of integration. In the second run, the biharmonic eddy coefficients are increased to -1×10^{19} and -6×10^{19} cm^4/sec for momentum and diffusion, respectively and the model is integrated for another 18 years starting from the end state of year 10 of the first run. The eddy viscosity of the second experiment is the same as in the flat-bottom model, but the eddy diffusivity is twice of that of the flat-bottom case. Although the kinetic energy increases again over this period from about 0.93 to 1.25 $ergs/cm^3$ (Figure 4.16), it shows some interesting features that can be compared to observations in the gulf.

The mean kinetic energy density is quite low compared to the flat-bottom case (about 2.5 $ergs/cm^3$) and is due the difference in the volume of the domain. In fact, the kinetic energy density in the upper 1200 m is larger in this case than the flat-bottom case. There are low-frequency fluctuations with periods longer than 1 year superimposed on the long-term increasing trend in the kinetic energy (Figure 4.16). It is quite surprising that no shorter period motions of less than 1 year including the 75–day fluctuations seen in flat-bottom case, are present.

The time series of the stream function at monitoring points reveal the spatial variabilities of the low-frequency fluctuations in the gulf (Figure 4.17). At VI and PP, the fluctuations are

Reproduced with permission of the copyright owner. Further reproduction prohibited without permission.

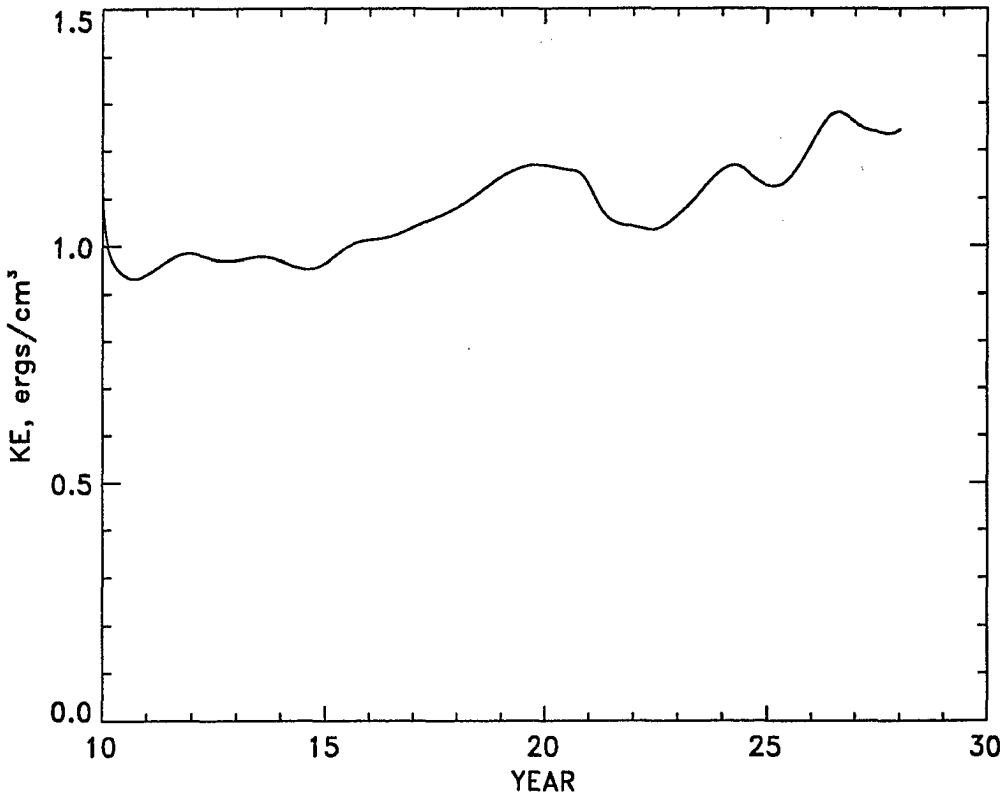

Figure 4.16 Time series of the basin-averaged kinetic energy (*ergs/cm³*).

regular in time and have a period of about 4 years. The range of the fluctuations is small at both locations and is less than 1 Sv.

At SE, CI and CK, the fluctuations are associated with the passages of eddies and can be better understood by contour plots of the perturbation stream function (Figure 4.18). A most prominent feature is a high around 57° N, 140° W in year 20. Before year 20, this anticyclonic eddy is not strong enough to be easily distinguished from other highs or lows. It propagates westward to near Kodiak Island and from there propagates southwestward along the shelf with the Alaska Stream. The eddy begins to weaken from year 22 and eventually becomes nondistinguishable from other eddies. Its passage is detected as peaks in the time series of the

Reproduced with permission of the copyright owner. Further reproduction prohibited without permission.

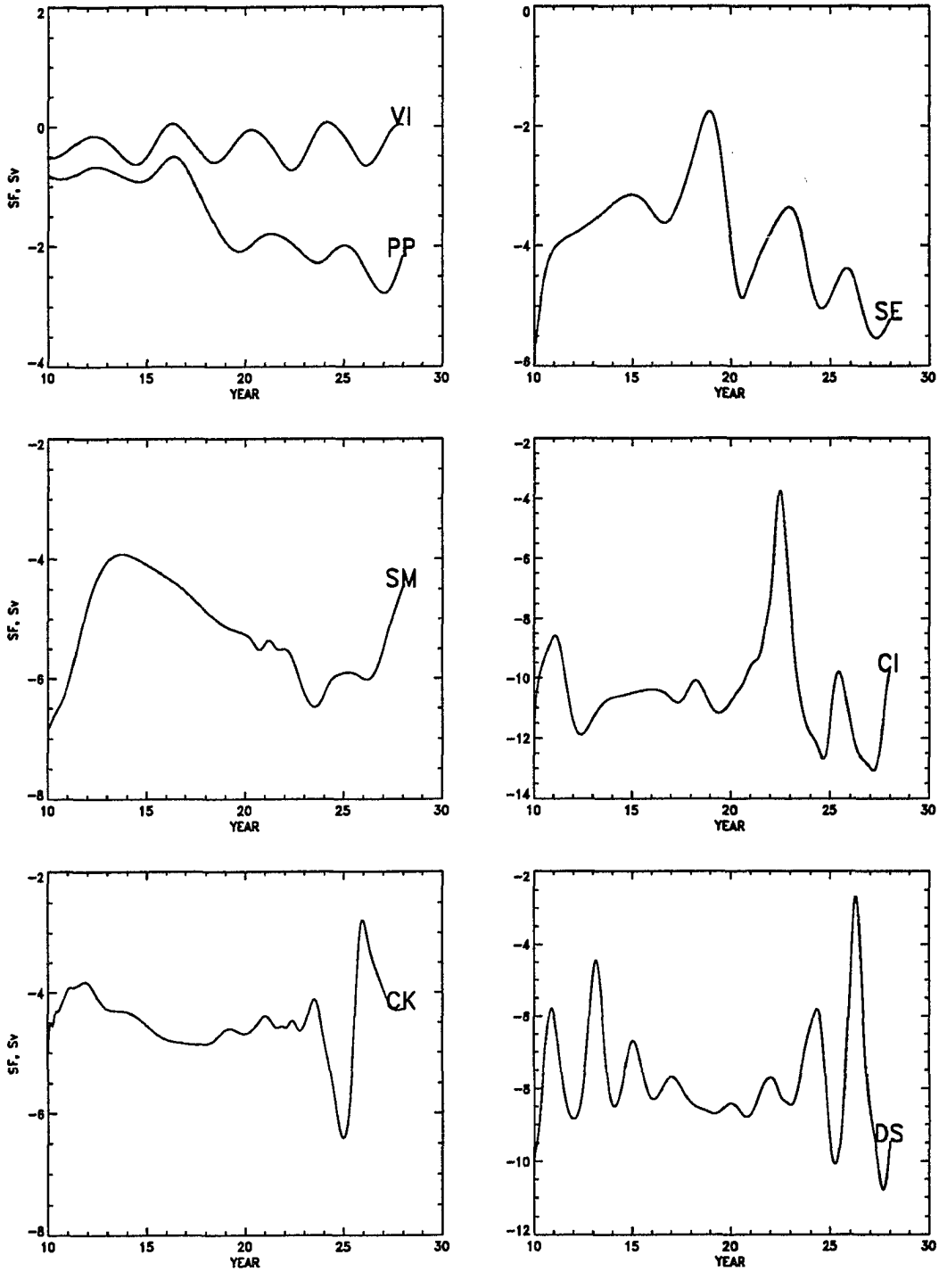

Figure 4.17 Time series of stream function at seven monitoring points (see Figure 3.3 for the locations).

Reproduced with permission of the copyright owner. Further reproduction prohibited without permission.

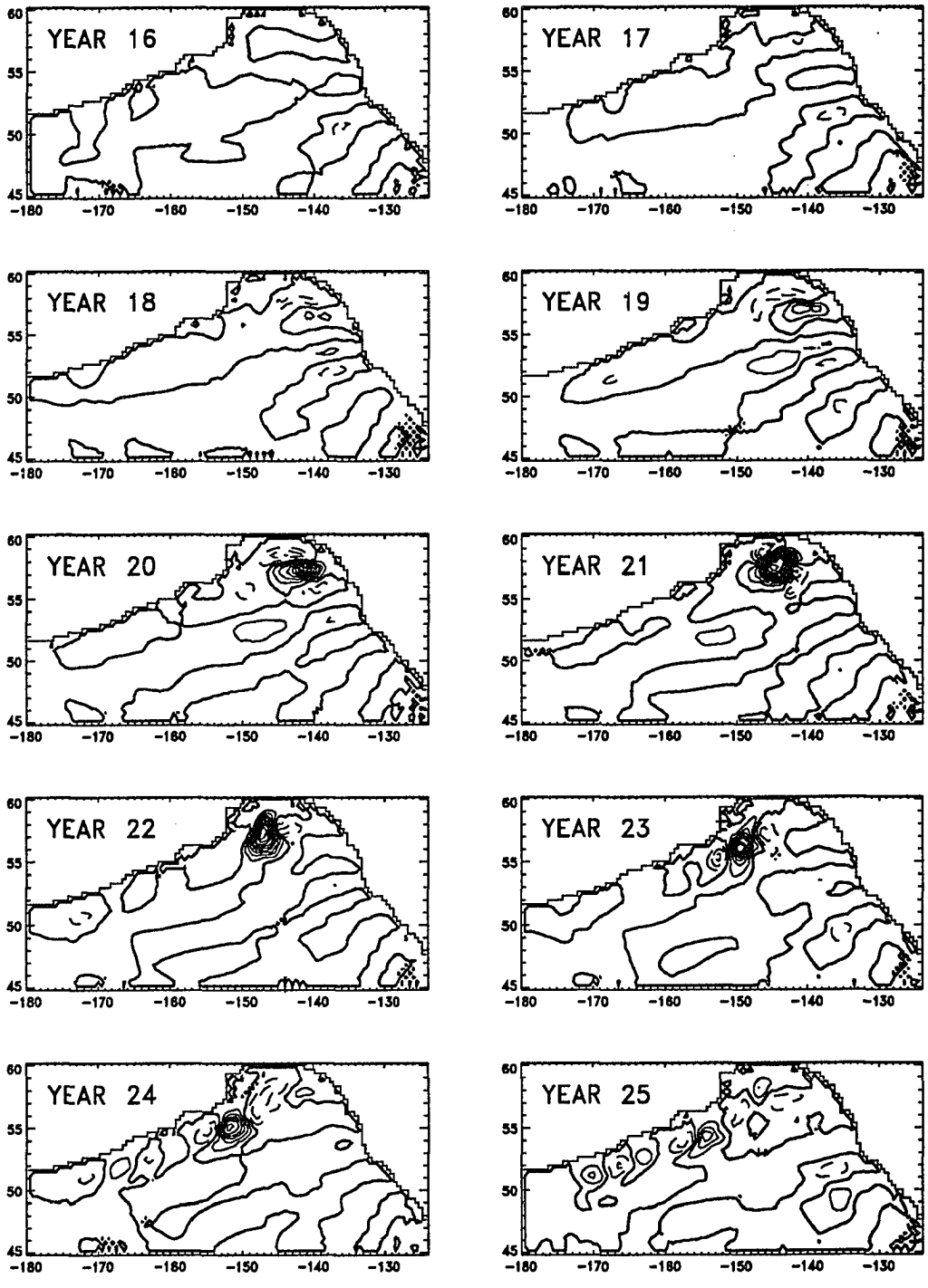

Figure 4.18 Demeaned and detrended stream function for year 16–25. Contour interval is 1 Sv and negative contour lines are denoted by dashed line.

Reproduced with permission of the copyright owner. Further reproduction prohibited without permission.

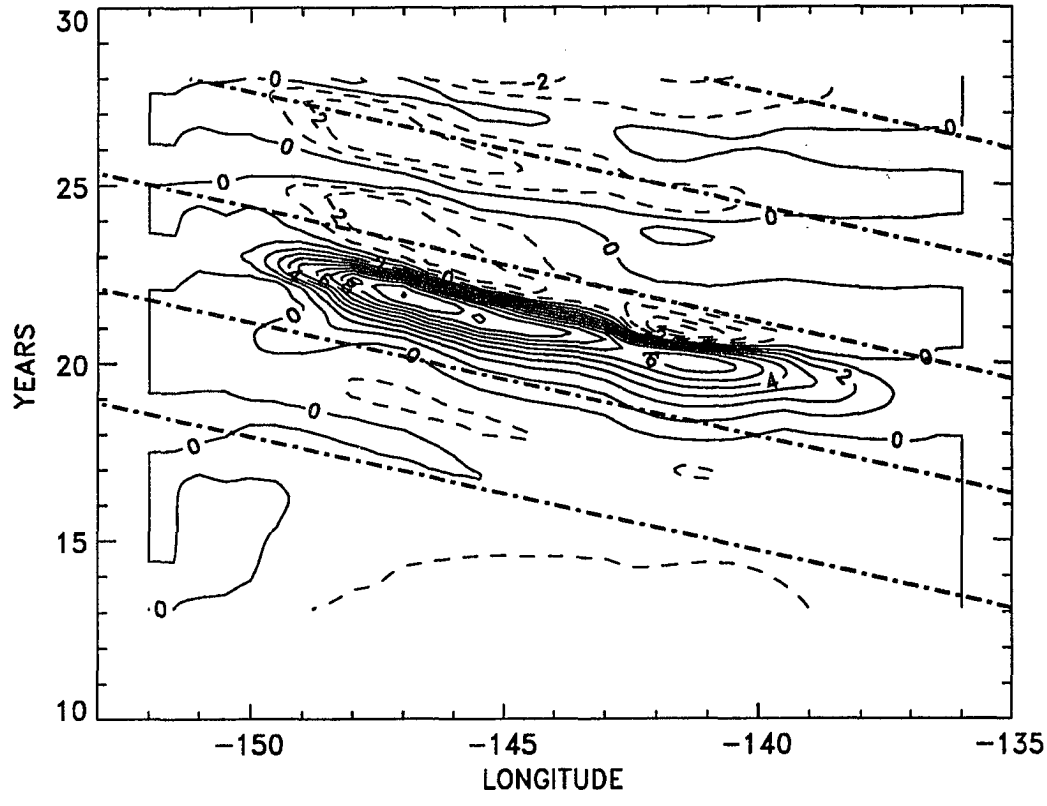

Figure 4.19 Contour plot of the detrended stream function in time-longitude space along 57° 10′ N. Superimposed are lines of constant speed of 0.6 *cm/sec.*

stream function at monitoring points (Figure 4.17). The first peak in year 19 at SE and a peak in year 22 at CI are caused by the passage of this anticyclonic eddy. It reaches CK in year 26 but the integration was not long enough to detect it at DS. There are two more peaks with ever decreasing amplitudes at SE. They occur in years 23 and 26 and propagate to CI to be recorded as peaks in year 25 and 28, respectively.

The period of the occurrence of these anticyclonic eddies at SE is 3–4 years and the propagation time to CI is 2–4 years. This can be summarized by a time-longitude plot along 57° 10′ N (Figure 4.19) which is close to the latitude where both points (SE and CI) are located. From this figure, one can estimate the westward propagation speed of these eddies as about 0.6

Reproduced with permission of the copyright owner. Further reproduction prohibited without permission.

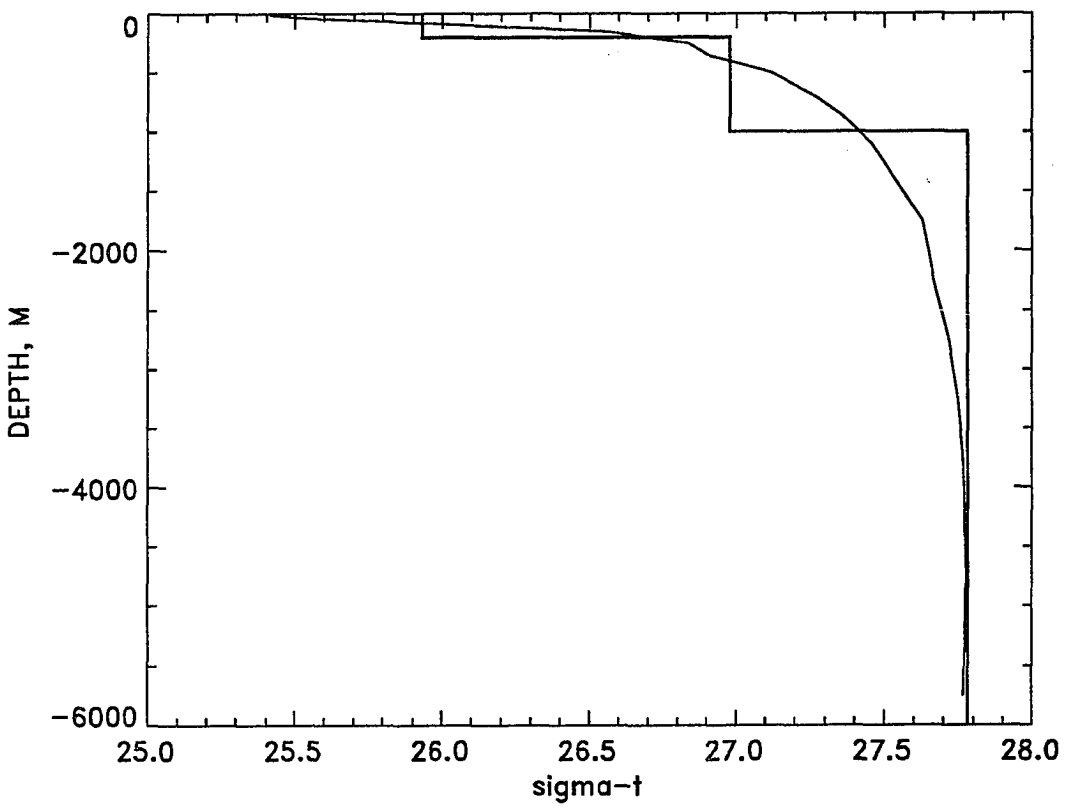

Figure 4.20 Vertical profile of the mean σ_t in topography case and the σ_t of 3–layer case.

cm/sec. The estimate of the zonal wavelength is 550–750 km from the period of 3–4 years and the phase speed of 0.6 *cm/sec*. The propagation speed is on the order of those of the baroclinic Rossby waves (Lighthill 1969) whose maximum westward propagation speed was shown to be given by equation (4.3). An effective depth of 0.73 *m* at 57° N is obtained from the westward propagation speed of 0.6 *cm/sec* by equation (4.3) and agrees well with the effective depth of 0.67 *m* which was estimated in the 3–layer case. Comparison of the mean σ_t profile of the present case and the σ_t used in the 3–layer case show that the 3–layer approximation is a good approximation of the continuous density profile (Figure 4.20). Therefore, these eddies can be interpreted as the first baroclinic Rossby waves.

Reproduced with permission of the copyright owner. Further reproduction prohibited without permission.

The anticyclonic eddies which propagate from SE to near Kodiak Island can be identified as the Sitka eddies. Tabata (1982) estimates the westward propagation speed of Sitka eddy to be more than 1.7 *cm/sec* and the transport associated with it 5–8 Sv. The estimate of the size of Sitka eddy (Tabata 1982) is 200–300 km and agrees well with the size of the anticyclonic eddies in the model (the size of an eddy is half its wavelength, 550–750 km in this case). Gower (1989) also reports the observation of eddies in the eastern gulf in Geosat altimetry data from November 1986 to June 1988 and concludes that the propagation is primarily to the west at a speed of about 1.3 *cm/sec*. There is a discrepancy between the observations and the model results; the propagation speed is only about half of the observation value. There are two possible explanations for this discrepancy; 1) the model effective depth is about half of that of the Gulf of Alaska when the observations were made, 2) the propagation speed is a sum of advection by mean current and the intrinsic speed (4.7) and the speed of the model mean current is smaller than that of the Gulf of Alaska. The effect of the gradient of the relative vorticity can be ignored because the propagation of eddies to near Kodiak Island occurs outside of the Alaska Stream unlike in the flat-bottom case where the eddies propagate within the Alaska Stream. However, it is not possible to determine the exact cause of the discrepancy without the observation data to estimate the effective depth and the mean current speed.

The propagation of anticyclonic eddies from near the coast of North America to the Alaska Stream provides an interesting possibility to interpret the abnormal shift of the Alaska gyre (Royer and Emery 1987). Royer and Emery (1987) and Reed (1984) report the disappearance of the Alaska Stream in the Cook Inlet line in summer 1981. As a possible cause of the shift, Reed (1984) suggests the change in the wind stress and Royer and Emery (1987) suggest the interaction of North Pacific Current with seamounts. Musgrave *et al.* (1990) observed a meander of the Alaska Stream in May 1988 and identify it as being caused by the arrival of an eddy originated from near Yakutat in January 1987 which was detected by Gower (1989).

Reproduced with permission of the copyright owner. Further reproduction prohibited without permission.

Musgrave *et al.* (1990) suggest the passage of anticyclonic eddies as an explanation of abnormal shift of the Alaska gyre. It has been shown in this thesis that the passage of anticyclonic eddies causes large decreases in the monitored transport of the Alaska Stream at fixed points (Figure 4.17). The model results agree with Musgrave *et al.* (1990) that there is no abnormal shift of Alaska gyre. Also, the disappearance of the Alaska Stream over the Cook Inlet line in summer 1981 could have been the result of the passage of anticyclonic eddy.

A series of oceanic lows and highs are elongated southwestward from the coast of North America (Figure 4.18). They propagate not only westward but also northward as can be seen more clearly in a time-longitude plot along 50° N and a time-latitude plot along 140° W (Figure 4.21). The fluctuations in the region of 48° N–51° N and 130° W–140° W are regular in time and their period is about 4 years. This period was also seen in the time series of the stream function at VI and PP (Figure 4.17). The region from the coast of North America to 145° W and south of 51° N can be delineated as the region with regular fluctuations with a period of 4 years. The propagation speed of the eddies in this region estimated from Figure 4.21 is about 0.6 *cm/sec* in both westward and northward directions. The northward propagation speed slows down to only about 0.3 *cm/sec* in the region north of 55° N (upper panel of Figure 4.21) and becomes zero near 58° N as the eddies approach closer to the land. The eddies then propagate westward (Figure 4.19).

Although the fluctuations farther north (>55° N) are not as regular as those in the southern region, one can estimate that the period is 3–4 years from the time series of stream function at SE (Figure 4.17) which is located only a couple of degrees to the east of the longitude along which Figure 4.21 is constructed. The most prominent anticyclonic eddy described above by the time series of stream function (Figure 4.17) and the time sequence of perturbation stream function (Figure 4.18) is also seen around 56°–58° N in year 20 (upper panel of Figure 4.21). In this figure, one can also see that this eddy and two more succeeding eddies are actually the

Reproduced with permission of the copyright owner. Further reproduction prohibited without permission.

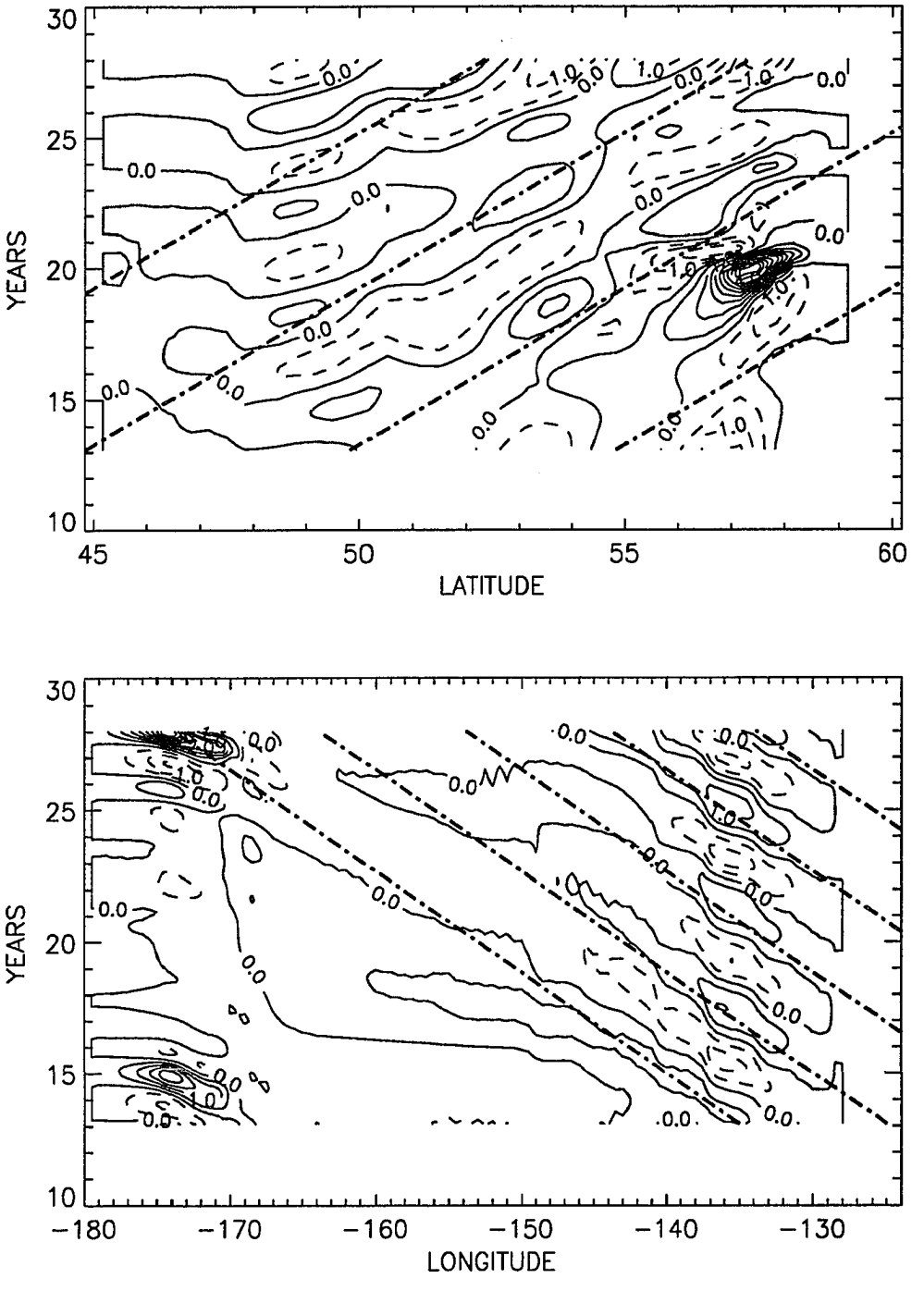

Figure 4.21 Contour plots of the detrended stream functions in time-longitude space along 50° N and in time-latitude space along 140° W. Superimposed are lines of constant speed; 0.3 *cm/sec* for time-latitude plot and 0.6 *cm/sec* for time-longitude plot.

Reproduced with permission of the copyright owner. Further reproduction prohibited without permission.

continuation of eddies formed farther south. Therefore, the Sitka eddy observed frequently near 57° N, 138° W (Tabata 1982) is not locally formed but it is formed farther to the south and has propagated to this latitude. It agrees with Cummins and Mysak (1988) that Sitka eddy is due to the instability of the Alaska Current.

EOF analysis is also performed for the stream function data sampled at every month from year 13 to 27. The first 11 modes explain 95 % of variance and the first eight modes are listed in Table 4.4. No mode displays significantly different characteristics from the other modes either in time or space except for the first mode which displays the long-term trend in time and meridionally banded structure (Figure 4.22) in space. On the other hand, all other modes have the alternating highs and lows in the eastern gulf and along the Alaska Stream and are probably manifestations of different phases of one phenomenon.

Table 4.4 Percentages explained by the first eight EOF modes of stream function from year 13 to 27.

Mode	1	2	3	4	5	6	7	8
Variance Explained(%)	23.1	17.0	13.6	10.6	7.1	6.6	5.6	4.4
Cumulative %	23.1	40.2	53.7	64.3	71.4	78.0	83.6	88.1

The eddies in this case are very low-frequency motions and there are only few cycles over the whole integration so that the energy and spectrum analyses used in the flat-bottom case have little meaning. Instead, spatial distributions of the linear trends in the zonal velocity and temperature are used to show that these eddies are due to baroclinic instability. The linear trend is computed by the least squares fit method and it has the dimension of acceleration (cm/sec^2) if velocity is used. Positive and negative linear trends indicate eastward and westward

Reproduced with permission of the copyright owner. Further reproduction prohibited without permission.

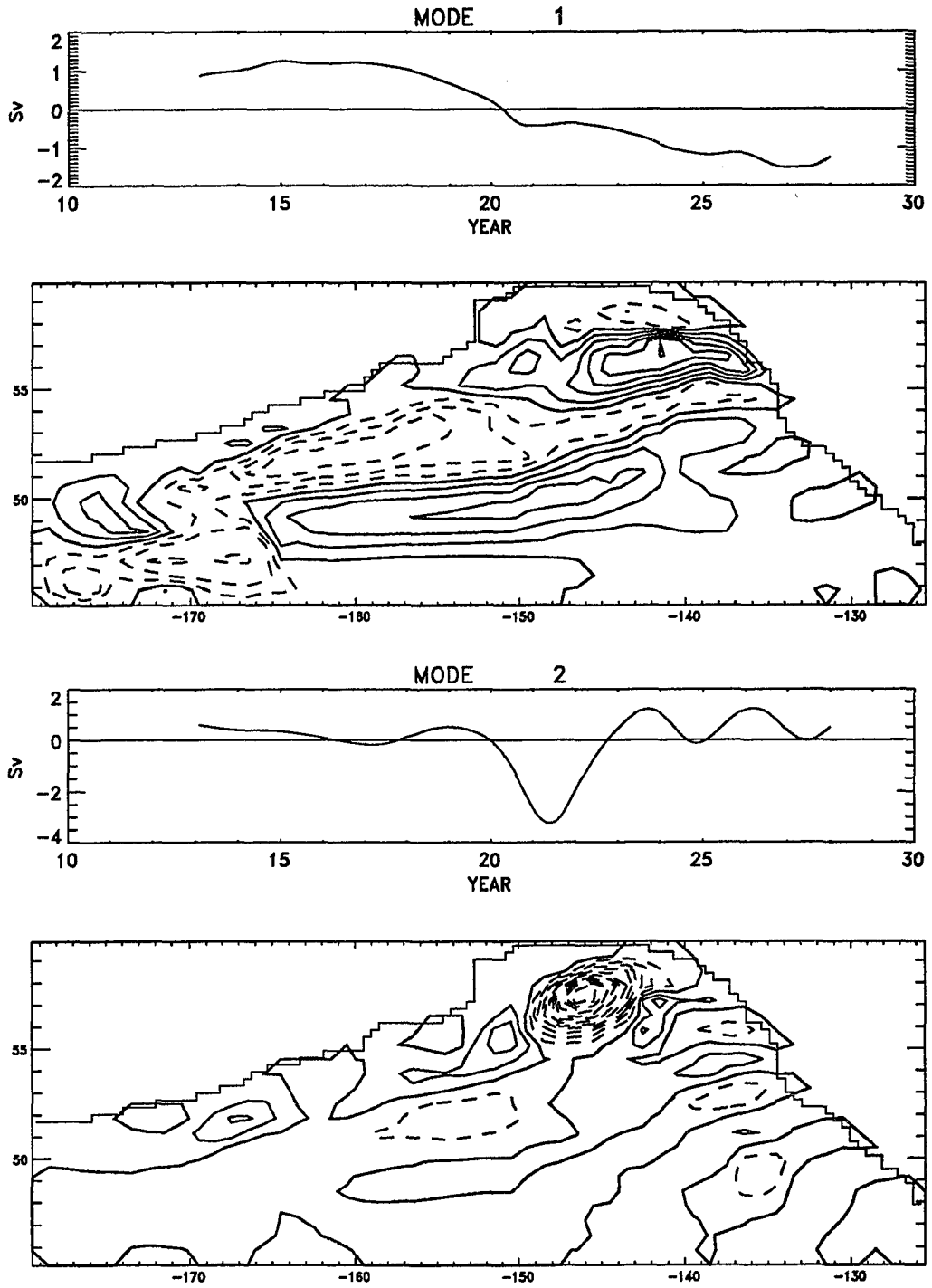

Figure 4.22 Time coefficients and eigenvectors of the first two EOF modes. Contour interval is 0.2.

Reproduced with permission of the copyright owner. Further reproduction prohibited without permission.

accelerations, respectively. An anticyclonic eddy consists of the positive (eastward) northern half and the negative (westward) southern half. This is based on the assumption that the eddy grows at the same position without propagation. This is possible since an eddy with a speed of 0.6 cm/sec travels about 200 km over one year which is only about 1/3 of its size. In Figure 4.23, one can see that the eddies at depth are ahead of the shallower ones all along the boundaries from the southeastern corner to the western end of the sloping boundary. Since the Alaska gyre flows in a counterclockwise sense, the eddies are aligned in the vertical direction in such a way that the mean potential energy is released into the eddy energy (Pedlosky 1982).

Comparison of the velocity tendencies with those in temperature provides a support on the usage of the tendency as a diagnostic tool. The center of the positive trend in temperature (Figure 4.23) corresponds to the center of the anticyclonic eddy (Figure 4.24. The boundary between the positive and negative accelerations in velocity is the center of the anticyclonic eddy). Since the anticyclonic eddy has a downwelling at its center and the positive tendency (increase) in temperature also indicates the downwelling, the trends in the velocity and temperature are consistent with the eddy dynamics.

Reproduced with permission of the copyright owner. Further reproduction prohibited without permission.

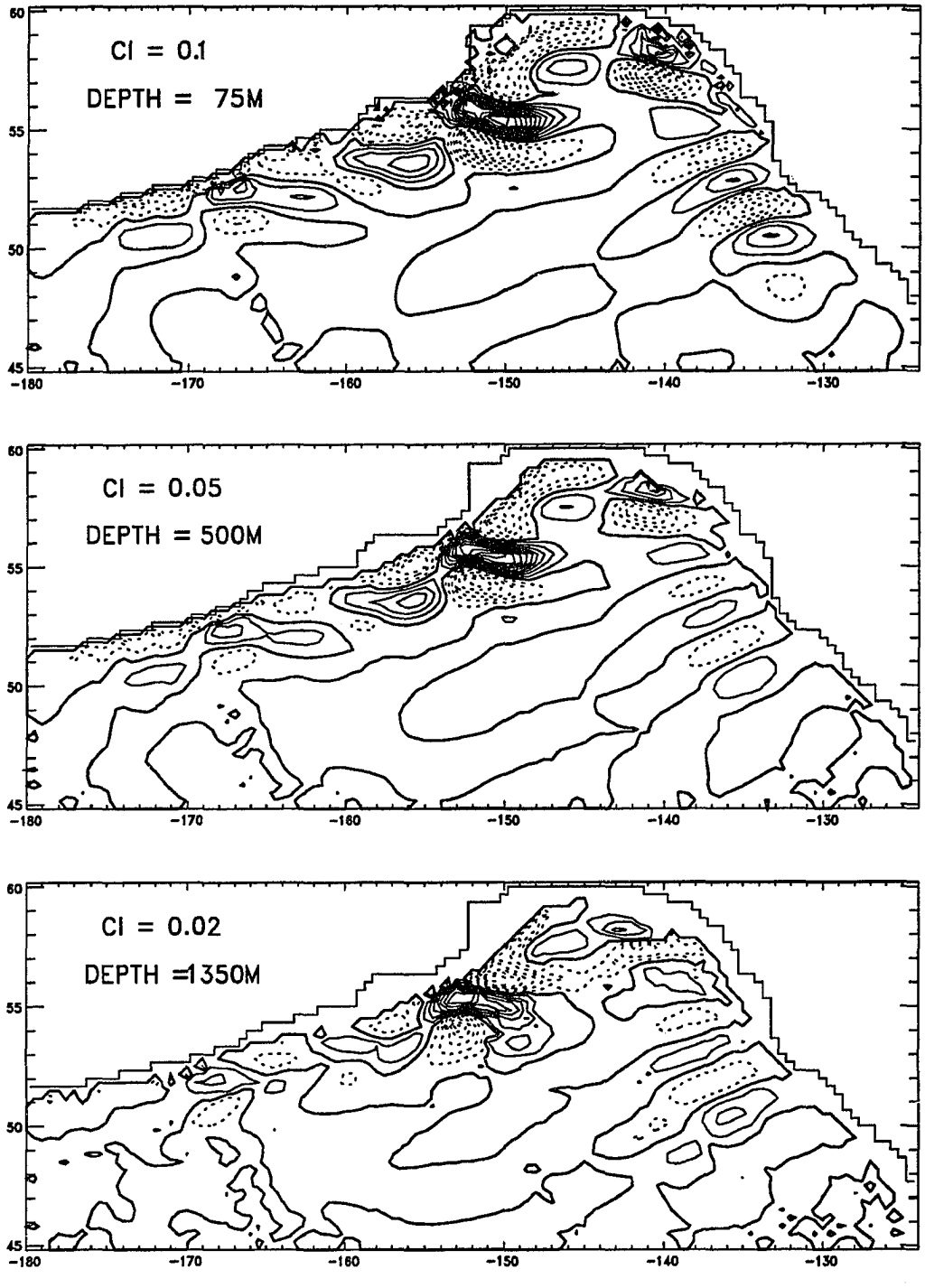

Figure 4.23 Distributions of linear trend in zonal velocities over 1 year in year 23–24 at three depths. Contour intervals (CI) and depths are indicated in the upper left corner of each figure. Solid lines represent positive trends.

Reproduced with permission of the copyright owner. Further reproduction prohibited without permission.

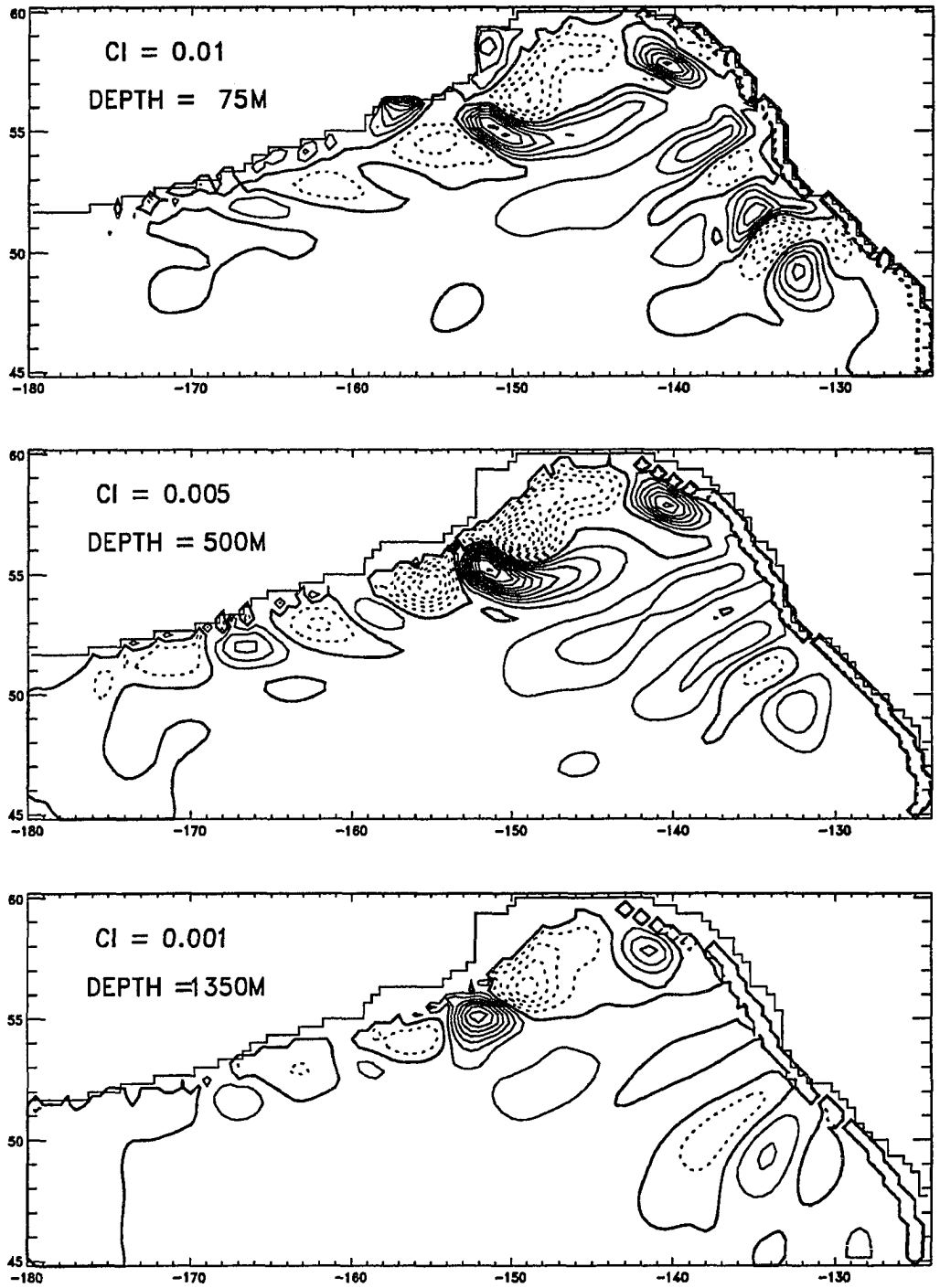

Figure 4.24 Distributions of trend in temperatures over 1 year in year 23–24 at three depths. Contour intervals (CI) and depths are indicated in the upper left corner of each figure. Solid lines represent positive trends.

Reproduced with permission of the copyright owner. Further reproduction prohibited without permission.

Section 4.5 Discussion and Conclusions

In this chapter, three numerical experiments were carried out which differed in their vertical resolution and forcing. The first experiment has flat bottom and is forced by wind stress only. It shows no signs of eddy activity but can be used for a study of the spin-up process. The spin-up time of about 10 years is consistent with time scales estimated from the propagation time of baroclinic Rossby waves. The baroclinic Rossby wave is excited from the density difference between the second and third layer of the model and has a phase speed of about 0.8 *cm/sec.*

An increase of vertical resolution and the addition of thermohaline forcing in the second experiment enables the generation of eddies. The eddies have a period of about 75 days and zonal wavelength of 250 km. These characteristics do not perfectly satisfy the dispersion relation of the zonally propagating barotropic Rossby waves. However, this discrepancy could be explained by including the effects of the advection by the mean current and of the meridional gradient of the relative vorticity. Baroclinic instabilities are the major generating mechanisms for these eddies according to the direct estimate of the energy transfer terms between various energy forms. A phase change of eddies with depth confirms this conclusion.

In the final experiment, the effects of bottom topography are revealed. The high-frequency eddies in the second experiment are not seen and low-frequency eddies appear as the dominant transient response. The period of these eddies are 3–4 years and is about an order of magnitude larger than the period 75 days of the flat-bottom case. An estimate of the zonal wavelength is 550–750 km from the period of 3–4 years and the westward propagation speed of about 0.6 *cm/sec.* These characteristics indicate that they are first baroclinic Rossby waves. Baroclinic instabilities are shown to be responsible for their growth by the phase change of the linear trends in temperature and velocity with depth.

Reproduced with permission of the copyright owner. Further reproduction prohibited without permission.

These eddies first appear in the Alaska Current region. The anticyclonic eddies which grow to the recognizable strength around Sitka are interpreted as the Sitka eddy. They keep growing while travelling westward to Cook Inlet where they reach their maximum strength. Subsequently, they weaken as they propagate to the west with the Alaska Stream. To explain the recurrence of the Sitka eddy, several theories are proposed. Willmot and Mysak (1980) seek the possibility of the reflection of the very low frequency waves (6 years) against the sloping boundary as an generating mechanism. Cummins and Mysak (1988) propose the baroclinic instability. Tabata (1982) suggests that the topography should play some role because the Sitka eddy reappears at the same location. 1 agree with Cummins and Mysak (1988) that the baroclinic instability of the Alaska Current is the generating mechanism of the Sitka eddy. However, there could be some local features near Sitka, for example topography or forcing (wind and horizontal density gradient), which reinforce the eddies.

I agree with Musgrave *et al.* (1990) on the cause of the abnormal shift of the Alaska gyre. A disappearance of the Alaska Stream is not due to an abnormal shift of the Alaska gyre but rather an abnormal shift of the Alaska Stream. Probably, the eddy was not detected in the hydrographic sections of Reed (1984) and Royer and Emery (1987) because of the poor sampling in space, especially in the alongstream direction. The anticyclonic eddy, however, was clearly seen in the drifter tracks of Musgrave *et al.* (1990). Cummins (1989) agrees with Reed (1984) that the abnormal shift of the Alaska gyre is due to the change in the wind stress by noting a seasonal migration of the Alaska gyre in east-west direction in his numerical model. In next chapter, a seasonal circulation in the Gulf of Alaska is also simulated and the abnormal shift of the Alaska gyre will be further discussed based on the model results.

Reproduced with permission of the copyright owner. Further reproduction prohibited without permission.

Chapter 5 SEASONAL BAROCLINIC MODEL

In Chapter 2 and 3, it is shown that the seasonal variability in the gulf, especially in the Alaska Stream, is only about 2 Sv and the role of topography is discussed in the light of the theory of Anderson and Corry (1985a) that the response of the ocean at high latitudes to the seasonal forcing is mainly barotropic which is strongly controlled by topography. In Chapter 4, annual mean wind and thermohaline forcings were used to simulate mean circulation and eddies in the Gulf of Alaska with and without bottom topography and the effect of topography on the mesoscale variability was revealed. Finally, the ocean response to the seasonal forcing is simulated in this chapter as a natural extension of the previous experiment.

Two cases follow the annual mean case of the previous chapter with the only difference being in the forcing. A 10–layer case is started using the end state after year 3 of the annual mean case and the topographic case is started after year 10 of the topography case. Seasonal forcings are applied in the same way as in the seasonal barotropic case, i.e., wind stress, surface temperature and salinity are first decomposed into harmonics and then reconstructed at every time step during the integration from the mean and amplitudes and phases of the annual and semi-annual harmonics. The robust-diagnostic method with 30 days of restoring time scale is also used for the thermohaline forcing.

Reproduced with permission of the copyright owner. Further reproduction prohibited without permission.

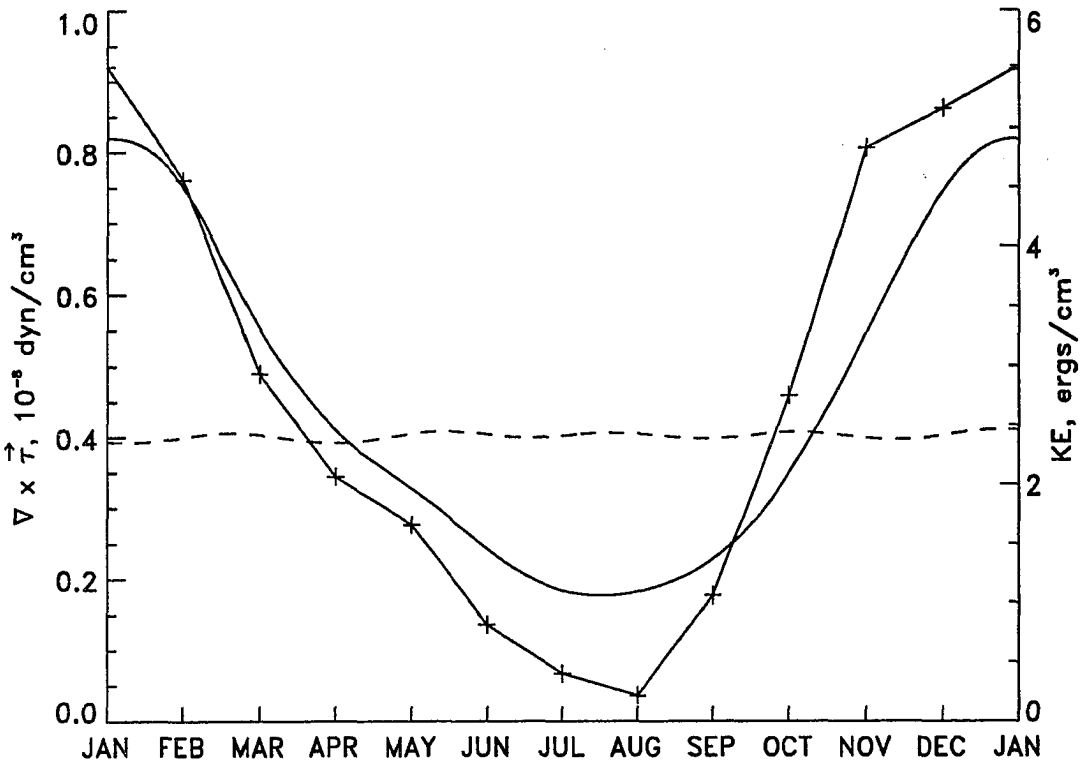

Figure 5.1 Basin-averaged kinetic energies (*ergs/cm³*) of 10–layer seasonal case (solid) and 10–layer annual mean case (dashed) from year 9–10 and monthly mean wind stress curl (+).

Section 5.1 10-layer Case

The basin-averaged kinetic energy (Figure 5.1) shows strong annual cycle with maximum in January (about 5 *ergs/cm³*) and minimum in July (about 1 *erg/cm³*). A most striking feature is the amplitude of the seasonal cycle (about 2 *ergs/cm³*) which is comparable in strength to the annual mean circulation (dashed line in Figure 5.1 and is about 2.5 *ergs/cm³*). Noting that the wind stress curl (solid line with + mark) also seasonally fluctuates with an amplitude (about 0.45×10^{-8} *dyn/cm³*) comparable to the annual mean wind stress curl, it is clear that the strong seasonal forcing also produces a strong response in a flat-bottom ocean.

Reproduced with permission of the copyright owner. Further reproduction prohibited without permission.

A detailed consideration of the energetics is used to explain the seasonal cycle in the kinetic energy. The kinetic energy equations of the total velocity, external mode (defined by the vertical average of the total velocity), and internal mode are derived following Holland (1975).

$$\frac{\partial E}{\partial t} = \iint_{\Sigma} (e+p)V_n d\sigma - \langle \rho g w \rangle + \iint_s \vec{u}\cdot\vec{\tau}_w d\sigma - \iint_b \vec{u}\cdot\vec{\tau}_b d\sigma + \left\langle \vec{u}\cdot\vec{F} \right\rangle - \left\langle \rho_0 \kappa \left(\frac{\partial \vec{u}}{\partial z}\right)^2 \right\rangle$$
$$= A + G + B + W + D, \tag{5.1}$$

$$\frac{\partial \bar{E}}{\partial t} = -\left\langle \rho_0 \vec{\bar{u}}\cdot\left(\overline{\vec{u}\cdot\nabla\vec{u} + w\frac{\partial \vec{u}}{\partial z}}\right)\right\rangle - \langle \vec{\bar{u}}\cdot\overline{\nabla p}\rangle + \iint_s \vec{\bar{u}}\cdot\vec{\tau}_w d\sigma - \iint_b \vec{\bar{u}}\cdot\vec{\tau}_b d\sigma + \left\langle \vec{\bar{u}}\cdot\vec{\bar{F}}\right\rangle$$
$$= N_e + B_e + W_e + D_e, \tag{5.2}$$

$$\frac{\partial E'}{\partial t} = N_i + B_i + W_i + D_i, \tag{5.3}$$

where

$$\langle\,\rangle \equiv \iiint \cdot dV$$
$$\overline{(\,)} \equiv \frac{1}{H}\int_{-H}^{0} \cdot dz$$
$$E = \frac{\rho_0}{2}\langle \vec{u}\cdot\vec{u}\rangle$$
$$\bar{E} = \frac{\rho_0}{2}\langle \vec{\bar{u}}\cdot\vec{\bar{u}}\rangle$$
$$E' = \frac{\rho_0}{2}\langle \vec{u}'\cdot\vec{u}'\rangle.$$

Σ is the surrounding surfaces of the integration domain including the ocean surface s and the ocean bottom b. V_n is the inward positive normal velocity on the surface and σ is the surface element. In (5.1), the first surface integral on the RHS represents the flux of the total kinetic energy (A) and the pressure work (G) through the boundaries. Wind effect is denoted by W and dissipations (the last three terms) by bottom friction, horizontal friction ($\vec{F}$ represents the horizontal friction), and vertical friction are collectively termed as D. N represents the effect by

Reproduced with permission of the copyright owner. Further reproduction prohibited without permission.

the nonlinear advection term. Finally, the subscripts e and i respectively represent the external and internal modes and it is straightforward to show that

$$N_i = A - N_e$$

$$B_i = G + B - B_e$$

$$W_i = W - W_e$$

$$D_i = D - D_e \tag{5.4}$$

A and G become zero in a closed domain but represent the exchange of kinetic energy with the outside domain if integration is done in a limited domain. B is the energy conversion term between the kinetic energy and the potential energy. The energy flows from kinetic energy to potential energy when B is negative, i.e., when the vertical velocity w is positive. There are two routes of energy exchange between the external and internal modes; direct exchange through the nonlinear term N and indirect exchange via the energy conversion terms B_e and B_i.

In Figure 5.2, wind forcing (W), work done by pressure gradient force (G+B), dissipation (D), and time rate of change of total kinetic energy ($T \equiv \partial E/\partial t$) are plotted over 2 years of period (year 9–11). Wind is the main source of the kinetic energy throughout the most of the year and is balanced by the work done by pressure gradient force (B+G) and the dissipation (D). The small net value resulting from the imbalance between them actually determines the time variation of the total kinetic energy. The wind forcing is always positive but the kinetic energy increases only when the wind forcing increases (July-January) according to Figure 5.2. Most of the energy from the wind forcing is used to increase the potential energy of the ocean.

A close look reveals that the contribution by the external mode is dominant in the time rate of change of the total kinetic energy (Figure 5.2). Since the external mode can be termed also as the barotropic mode, the dominance of the barotropic mode in the time variation demonstrates

Reproduced with permission of the copyright owner. Further reproduction prohibited without permission.

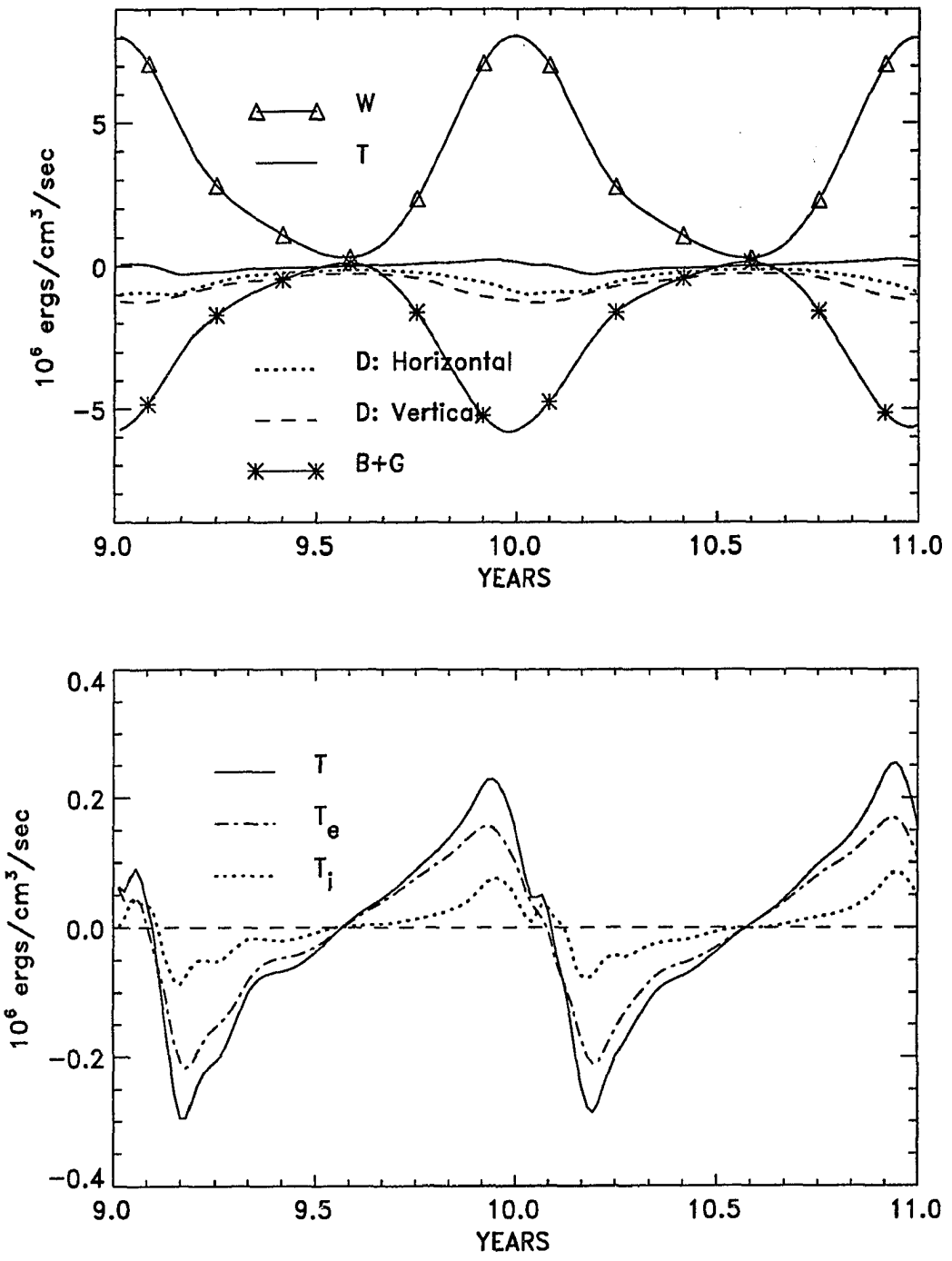

Figure 5.2 The energy balance of the total kinetic energy (upper: see text for details) and decomposition of T into the external ($T_e \equiv \partial \tilde{E}/\partial t$) and internal ($T_i \equiv \partial E'/\partial t$) modes (lower).

Reproduced with permission of the copyright owner. Further reproduction prohibited without permission.

that the transient ocean response in the absence of the topography is mainly barotropic. It may then explain why the seasonal fluctuation in a flat-bottom ocean is large. The fast propagation speed of the barotropic Rossby wave and consequently the short spin-up time, which is only one month at most, makes the ocean response almost in phase with the forcing. Also, the amplitude of the response is large, especially in this flat-bottom case because there is no dissipation or scattering of the barotropic mode by topography. However, this would not be the case near the equator where the propagation speed of the baroclinic Rossby wave is comparable to the barotropic Rossby wave. This result is also consistent with the theory that the ocean response to the seasonal forcing at middle and high latitudes is mainly barotropic (Anderson and Corry 1985a).

More detailed energy balances of the internal and external modes (Figure 5.3) show that the major components maintaining the external mode are the wind (W_e) and the dissipation (D_e) while the wind (W_i) and the energy conversion term (B_i) are the major terms in the balance of the internal mode. Of the dissipation of the external mode, the bottom friction is the dominant component. About two thirds of the wind energy enters the ocean through the internal mode and most of the dissipation is done through the external mode. The nonlinear term shows an energy flow from the internal mode to the external mode.

Seasonal circulation (Figure 5.4) shows a large seasonal variability as in the seasonal barotropic model (Figure 3.4). The cyclonic gyre covers the entire gulf in fall (December) and winter (March) but retreats to west and north in other seasons. The zero stream function lines in spring (June) and summer (September) are also more or less at the same position as the zero wind stress curl lines (Figure 1.9). This confirms that the barotropic mode is the main response of the flat-bottom ocean. Eddies are also seen in the westward flowing boundary current from 140° W to at least 160° W (Figure 5.4).

An EOF analysis is done for the 2–year stream function data of year 9–11 (Figure 5.5)

Reproduced with permission of the copyright owner. Further reproduction prohibited without permission.

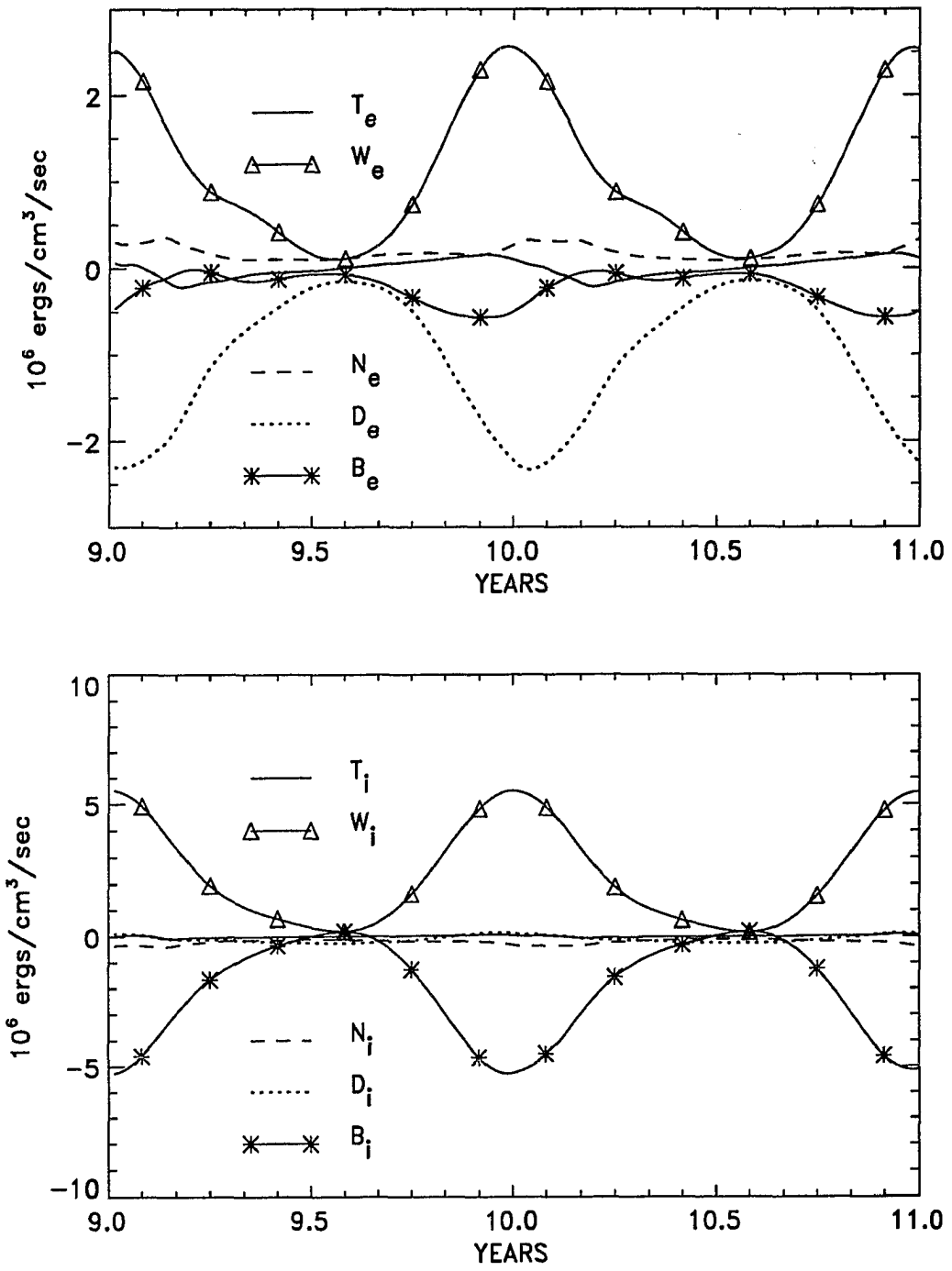

Figure 5.3 The energy balance of the external (upper) and internal (lower) modes.

Reproduced with permission of the copyright owner. Further reproduction prohibited without permission.

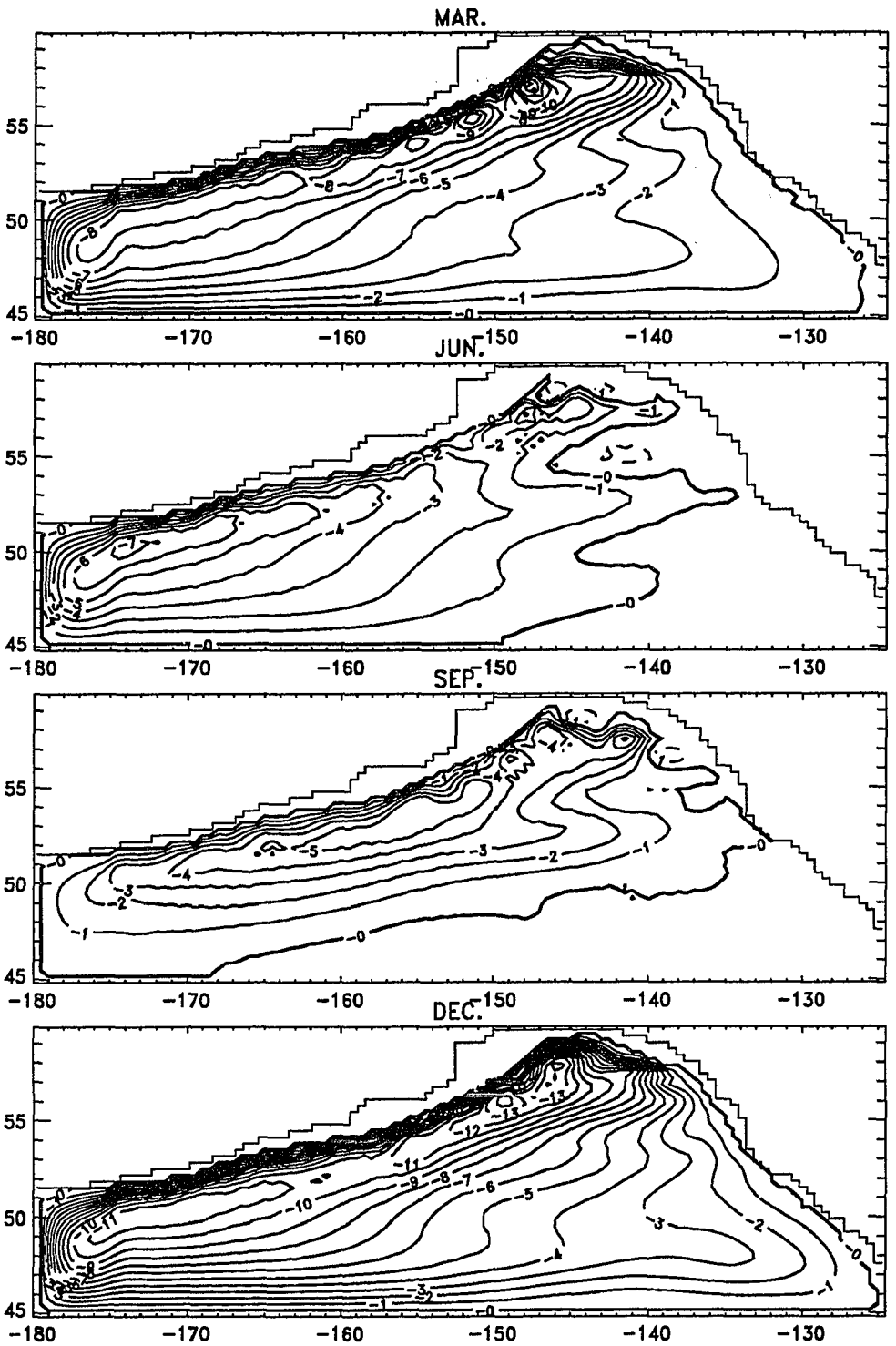

Figure 5.4 Contour plots of stream function in March, June, September, and December from year 9.

Reproduced with permission of the copyright owner. Further reproduction prohibited without permission.

and it shows that the seasonal forcing generates most of the fluctuations. The first mode which fluctuates at annual frequency and explains 86.3 % of all variances is characterized by a quick rise and slow fall of the time function. The spatial pattern of the eigenvector resembles the mean cyclonic gyre and represents the cycle of intensification and weakening of cyclonic circulation through the year. The maximum amplitude of variation associated with the first mode is about 7 Sv (the contribution of each mode to the original data is time function × eigenvector, i.e., 80 from time function × 0.09 from eigenvector of the first mode) at the center of gyre. The time function of the second mode fluctuates at semi-annual frequency and explains only 8 % of the total variance. This mode displays a bimodal structure in space with a cyclonic gyre in the northeast half and an anticyclonic gyre in the southwest half and shows a westward shift of the gyre during the spring and summer.

Table 5.1 Percentages explained by the first three EOF modes of stream function from year 9 to 11.

Mode	1	2	3
Variance Explained(%)	86.3	8.0	3.6
Cumulative %	86.3	94.3	97.9

Another EOF analysis is done after annual and semi-annual frequencies are taken out by FFT method to focus on the eddy motion. The first and second modes of this second EOF analysis each contain nearly equal amounts of variance (31 and 30 %) and their time functions also display the same pattern with about 90° phase difference (Table 5.2 and Figure 5.6). The time function displays the larger eddy activity of a period 70–80 days in oceanic winter and spring (November-March) than other seasons. Next two modes (8.2 and 7 %) also can be grouped together to represent one phenomenon. This group also shows increased eddy activity

Reproduced with permission of the copyright owner. Further reproduction prohibited without permission.

in winter and spring and the period is about 95 days (Figure 5.7). The eigenvector of this group shows uniformly distributed eddies along the sloping boundary and can be compared to the first and second modes which have the eddy activity concentrated in the upstream region.

It is interesting to note that the period of the dominant eddy activity (1st and 2nd modes) is 70–80 days which was also the dominant period in the annual mean case. This coincidence of the period indicates that the change in the forcing does not affect the intrinsic instability and is consistent with the theory that the forcing sets up the basic state and the instability does not depend on how the basic state is formed or by what process (Pedlosky 1982). However, the eddies almost disappear in the summer and fall. The attenuation of the eddy activity during these seasons may be due to the conversion of the potential energy to the kinetic energy (Figure 5.2) which would greatly reduce the energy flow to the eddies by baroclinic instability.

Table 5.2 Percentages explained by the first eight EOF modes of the filtered stream function from year 9 to 11.

Mode	1	2	3	4	5	6	7	8
Variance Explained(%)	31.2	29.8	8.2	7.0	4.6	4.5	2.9	2.2
Cumulative %	31.2	61.0	69.2	76.2	80.8	85.3	88.2	90.4

Reproduced with permission of the copyright owner. Further reproduction prohibited without permission.

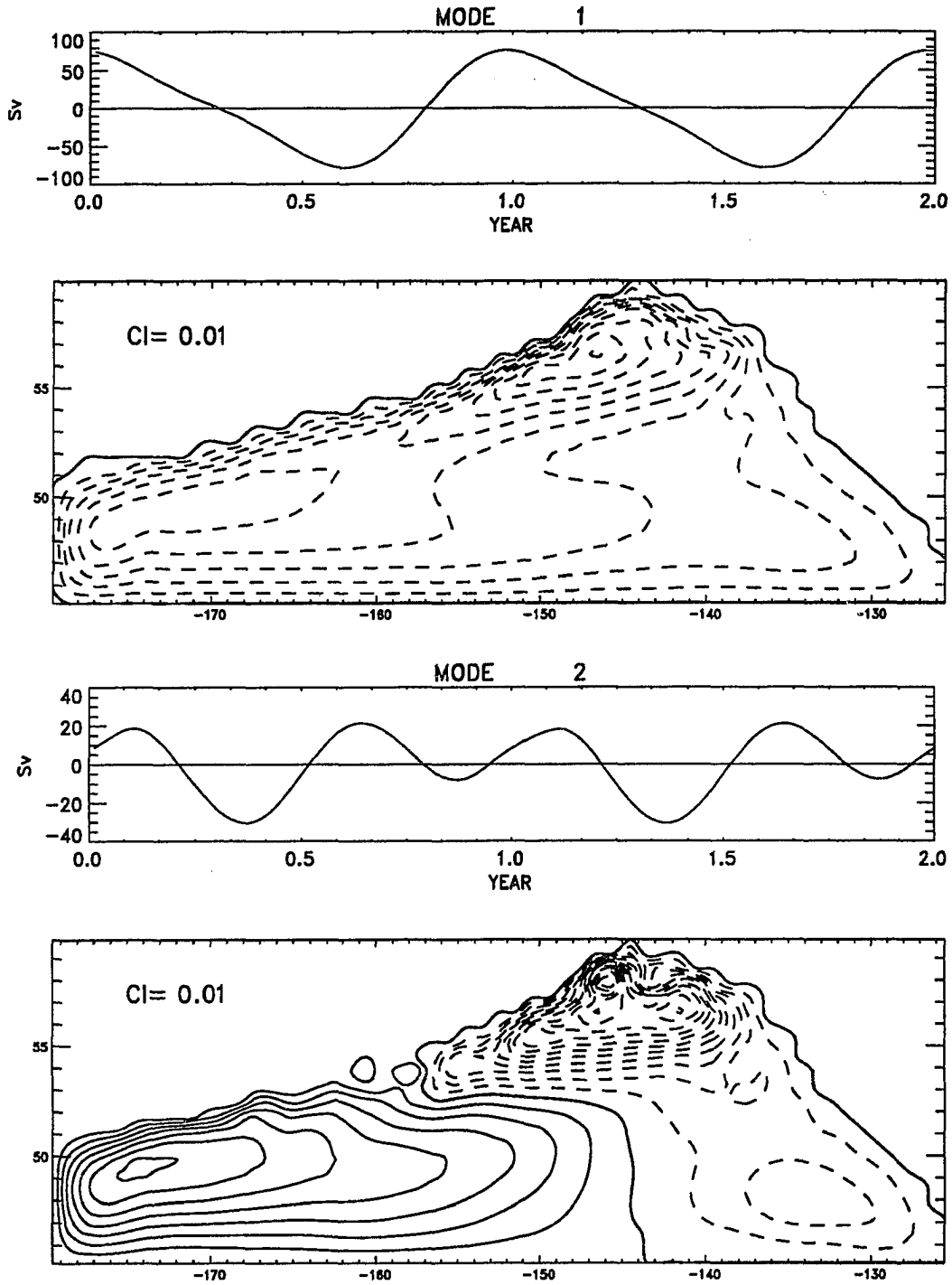

Figure 5.5 Time functions and eigenvectors of the first two EOF modes of year 9–11 before removal of the annual and semi-annual signals.

Reproduced with permission of the copyright owner. Further reproduction prohibited without permission.

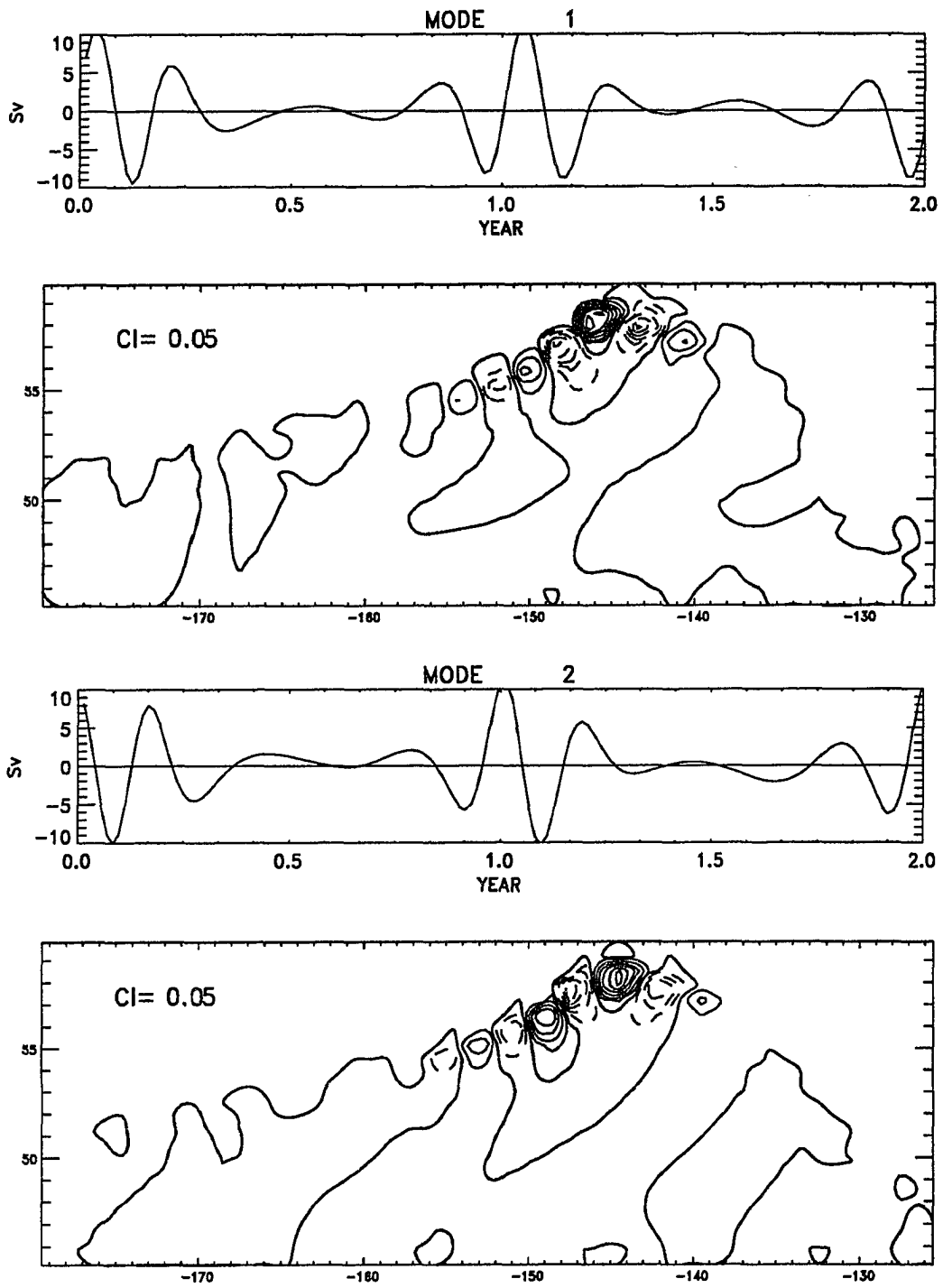

Figure 5.6 Time functions and eigenvectors of the first two EOF modes of year 9–11 after removal of the annual and semi-annual signals.

Reproduced with permission of the copyright owner. Further reproduction prohibited without permission.

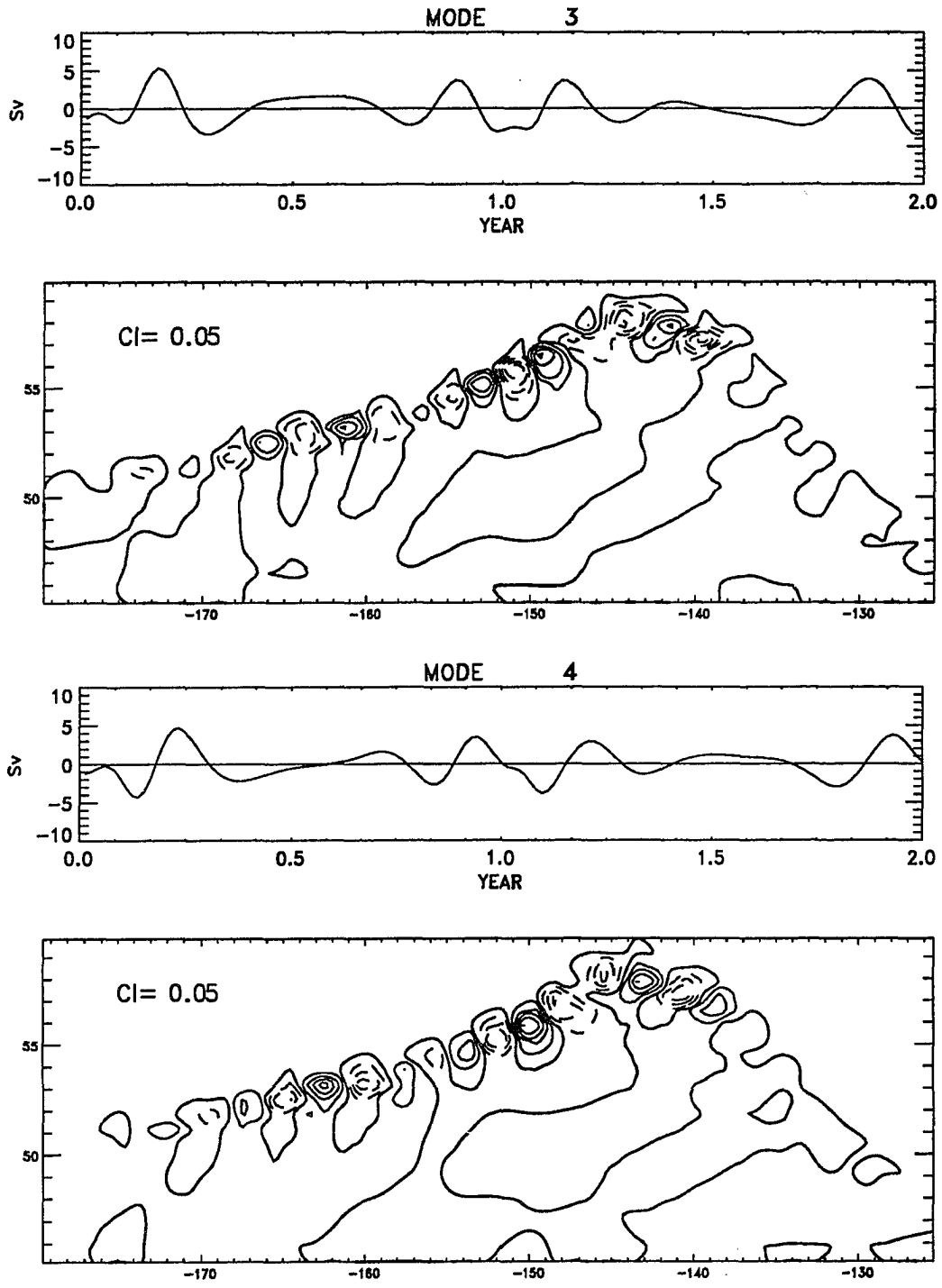

Figure 5.7 Time functions and eigenvectors of the next two (3rd and 4th) EOF modes of year 9–11 after removal of the annual and semi-annual signals.

Reproduced with permission of the copyright owner. Further reproduction prohibited without permission.

Section 5.2 Topography Case

The introduction of the topography into the model radically changes the ocean response to the seasonal forcing. The seasonal fluctuation of the kinetic energy is greatly reduced compared to the flat-bottom case (Figure 5.8and 5.1). The seasonal range, about 0.5 $ergs/cm^3$, is almost an order of magnitude smaller than the seasonal range of the flat-bottom case. However, a direct comparison of two cases by the basin-averaged kinetic energy can be misleading because of the contribution of the deep layers with a weak circulation and large volume. It was also shown in the annual mean case that the kinetic energy of the upper 1200 *m* of the topography case is comparable to or larger than the kinetic energy of the flat-bottom case. The kinetic energy averaged over the same volume (regions shallower than 1200 *m* are not included) as the flat-bottom case from the monthly data of year 18–19 confirms this (Figure 5.9). A comparison of two cases by the kinetic energy in the upper 1200 *m* is supported by the fact that the seasonal fluctuation occurs primarily in the upper 1000 *m* or so. The seasonal range of the kinetic energy decreases almost exponentially from the surface to about 1000 *m* by more than two orders of magnitude (not shown).

The amplitude of the seasonal fluctuation of the kinetic energy in the upper 1200 *m* is then about 0.5 $ergs/cm^3$, which is only about a quarter of the seasonal amplitude of the flat-bottom case (Figure 5.9). More importantly, the seasonal amplitude relative to the annual mean is about 17 % (Figure 5.9), which is considerably smaller than the about 80 % of the flat-bottom case. This small response clearly shows the effect of the topography. The seasonal amplitude 17 % of the kinetic energy implies that the seasonal amplitude of the transport is less than 10 % (the kinetic energy is the square of the transport). It is less than the estimate 13 % of the seasonal amplitude of the Alaska Stream transport by Royer (1981).

Reproduced with permission of the copyright owner. Further reproduction prohibited without permission.

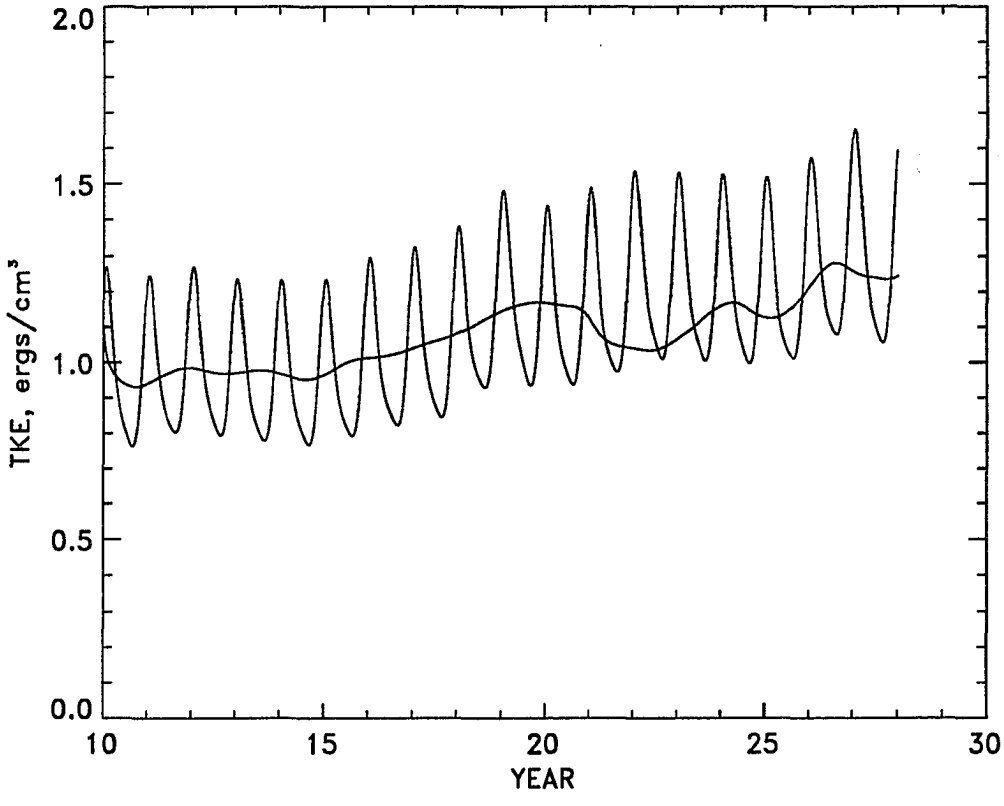

Figure 5.8 Basin-averaged kinetic energy (*ergs/cm*^{3}) of seasonal topography case. Kinetic energy of annual mean case is also shown for comparison.

Decomposition of the total velocity into the external and internal modes is done to investigate the roles of each mode in the seasonal response (Figure 5.10). The results show that both modes contribute more or less equally to the time variation of the total kinetic energy (T) unlike in the flat-bottom case where the external mode was dominant. The amplitude of T of the present case is only a quarter of that of the flat-bottom case and the reduction from the values of the flat-bottom case is more severe in the external mode (T_e) than the internal mode (T_i). The external mode is reduced almost an order of magnitude (85 %) while the internal mode is reduced by about 45 %. If the upper 1200 m is considered (not shown), the seasonal amplitude of the internal mode stays almost same as in the flat-bottom case and most of the

Reproduced with permission of the copyright owner. Further reproduction prohibited without permission.

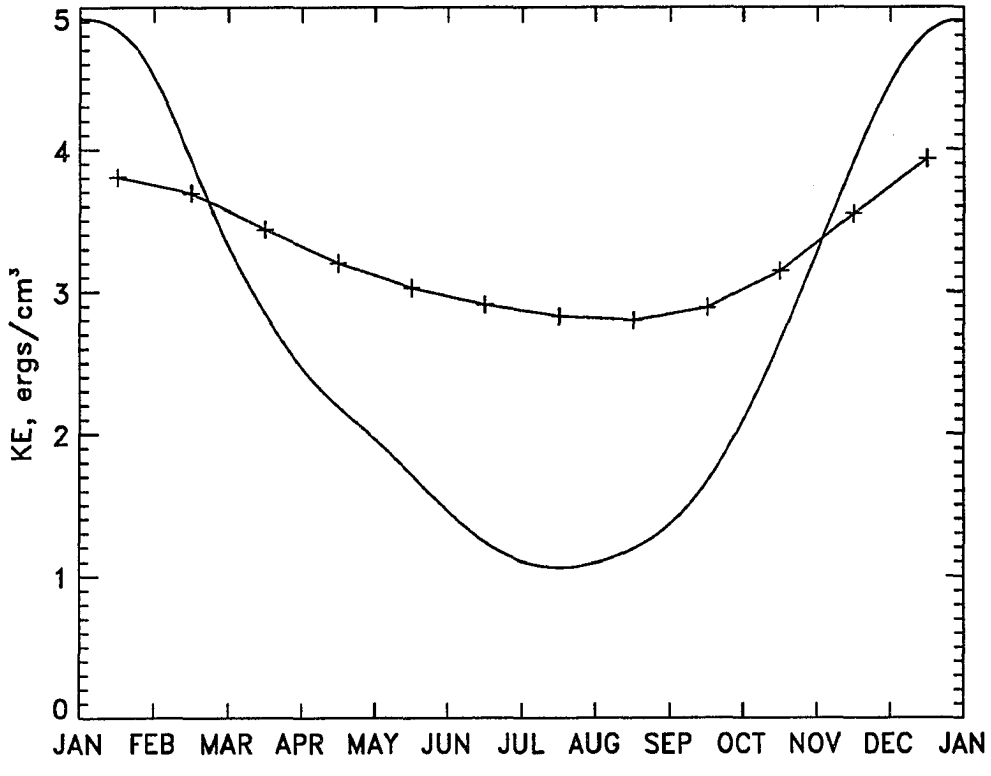

Figure 5.9 Kinetic energy (*ergs/cm³*) of the upper 1200 *m* of year 18–19 (+). Basin-averaged kinetic energy of the flat-bottom case is also shown for comparison (solid).

reduction is in the external mode (in this case, the external mode is the vertical average over 1200 m). Therefore, the presence of the topography has major impact on the external mode and the reduced role of the external mode in the topography case results in the small seasonal variability.

As in the flat-bottom case, most of the wind energy input to the ocean occurs through the internal mode (Figure 5.11) and is mainly balanced by the work by pressure force (B_i). In the external mode, however, the pressure work (B_e) plays an important role as well as the wind energy input and the dissipation which were two major terms in the balance of the external

Reproduced with permission of the copyright owner. Further reproduction prohibited without permission.

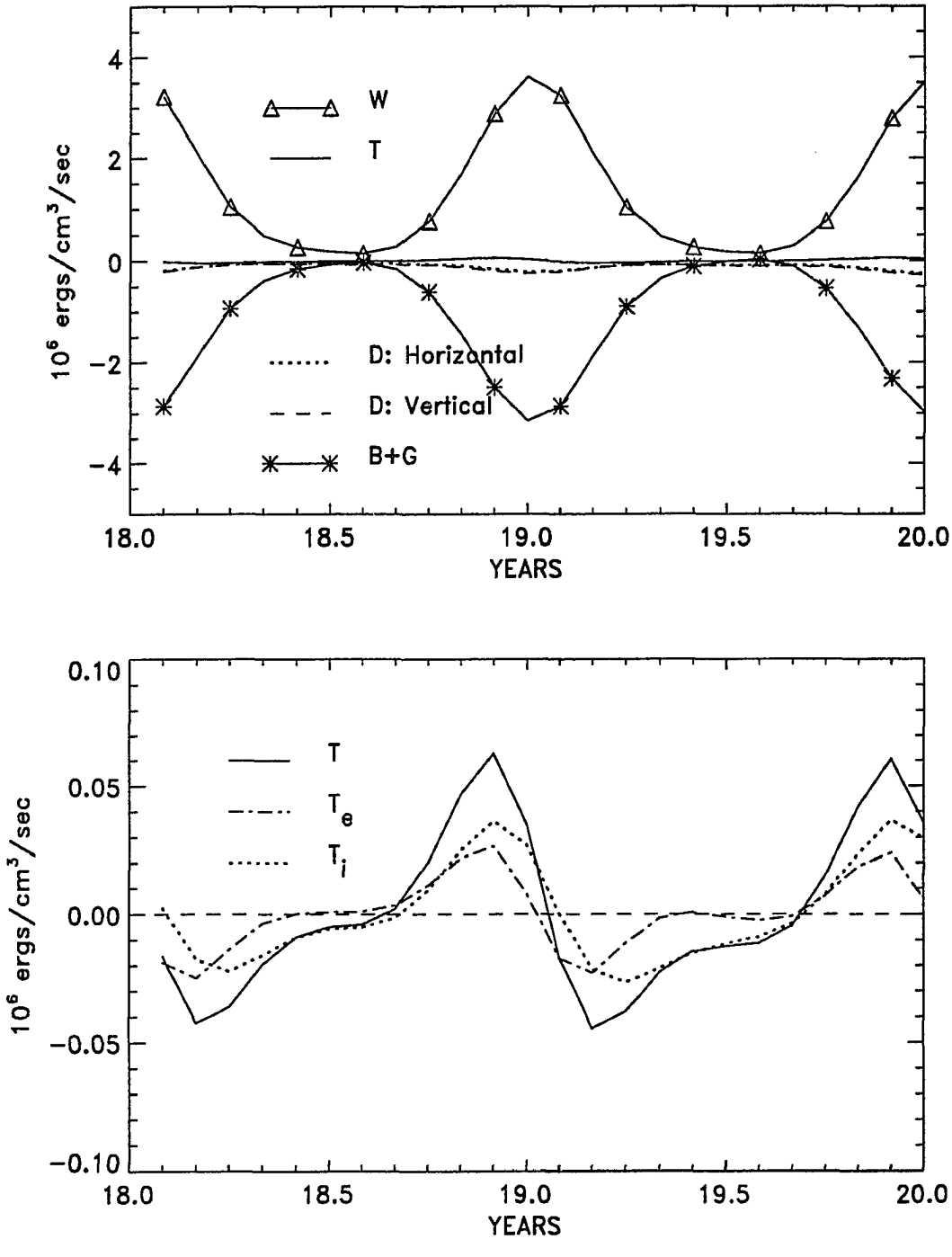

Figure 5.10 The energy balance of the total kinetic energy (upper) and decomposition of the time rate of change (T) into the external (T_e) and internal (T_i) modes (lower).

Reproduced with permission of the copyright owner. Further reproduction prohibited without permission.

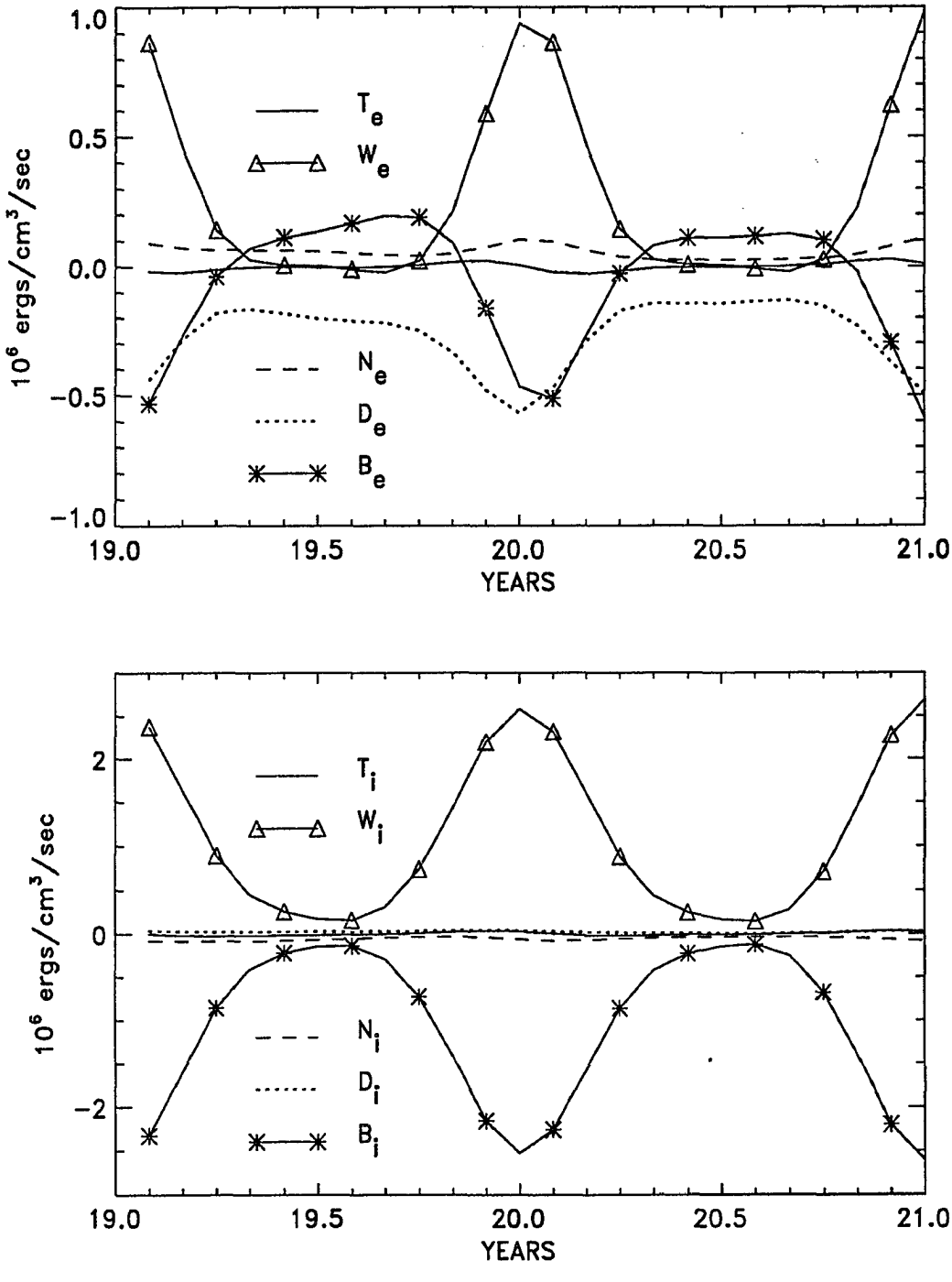

Figure 5.11 The energy balance of the external (upper) and internal (lower) modes.

Reproduced with permission of the copyright owner. Further reproduction prohibited without permission.

mode of the flat-bottom case. In this topography case, the rates of the wind energy input and the dissipation through the external mode are about 50 % and 25 % of the corresponding rates of the flat-bottom case, respectively. During the period of small wind energy input, a balance is achieved between B_e and D_e while they together balance W_e when the wind energy input is large. Therefore, the external mode is driven by wind forcing from November through March and by pressure work (or energy release from potential energy) during the rest of the year. In a numerical model of Indian Ocean (Cox 1970), Holland (1975) also finds that the external mode is maintained by B_e during the winter months when the wind forcing is weak there.

Seasonal variation of the transport is estimated by the range of the monthly stream function over one year of year 18–19 (Figure 5.12). This year is chosen because it is about the middle of the whole integration and the seasonal fluctuation remains almost constant year to year (Figure 5.8). The seasonal range is again defined by the difference of maximum and minimum values of stream function after a linear trend is subtracted. The spatial distribution of the seasonal range resembles closely that of the seasonal barotropic model (Figure 3.2) and no major differences in the pattern are found between these two figures except for their magnitudes. In general, the seasonal ranges of the baroclinic model are larger than those of the barotropic model but the differences are mainly found in those regions with large values.

The fact that the spatial pattern of the seasonal range of the baroclinic model is almost identical to that of the barotropic model suggests that the seasonal variation is mainly barotropic. One may argue that the stream function used for the determination of the seasonal range is a barotropic variable. But considering that a change in the density field would also cause changes in the stream function, the close similarity between the baroclinic model and barotropic model strongly indicates that there is little seasonal change in the density field. This in turn means that the seasonal variability in the Gulf of Alaska is mainly barotropic.

Signals not directly associated with forcing frequencies are sorted out by the same FFT

Reproduced with permission of the copyright owner. Further reproduction prohibited without permission.

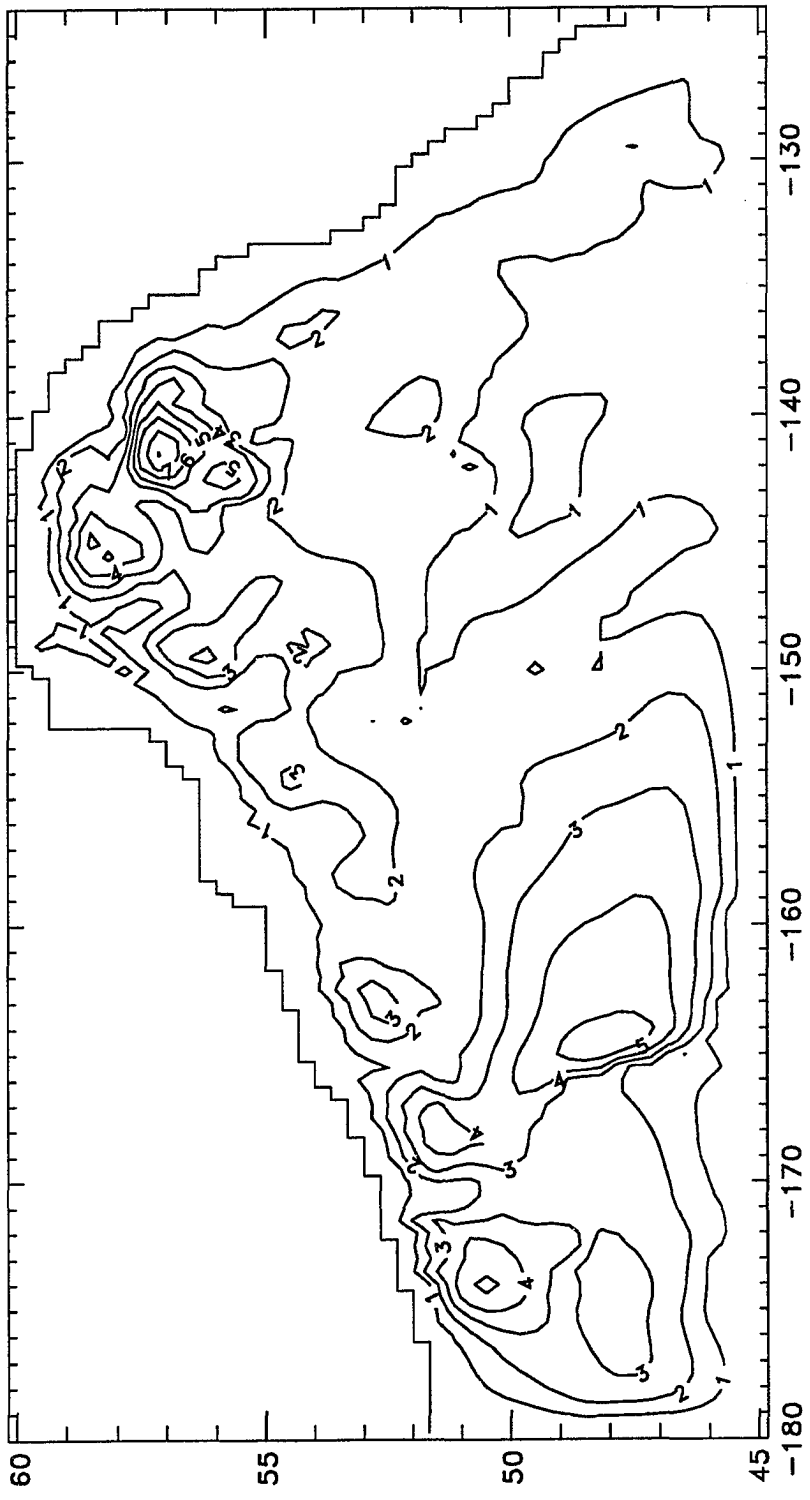

Figure 5.12 The seasonal range of stream function from year 18–19.

Reproduced with permission of the copyright owner. Further reproduction prohibited without permission.

filtering as in the previous section for the time series of stream function at monitoring points (Figure 5.13). The filtered time series are remarkably similar to those of the annual mean case (Figure 4.17) indicating that the mesoscale variability or eddies are not affected by the seasonal forcing. The similarity of the time series of the annual mean case and the seasonal case is better than the flat-bottom case where a seasonal attenuation of eddy activity was noted (Figure 5.6). It suggests that the basic state, upon which the instability depends, does not change significantly by the seasonal forcing while the basic state of the flat-bottom case changes over the season. Therefore, the seasonal fluctuation in the forcing has little effect on the mean state of the Gulf of Alaska and the eddies are due to intrinsic instability of the mean state.

No clear seasonal variations are found in the seasonal circulation pattern (Figure 5.14) except for an appearance of the anticyclonic circulations within a couple degrees of the southern boundary and the coast of North America south of 55° N in spring and summer. These results are consistent with the above conclusion that the mean state changes little over the seasons. This is in contrast to Cummins (1989) where seasonal westward shift of the gyre is observed in his QG model. Based on this shift, Cummins (1989) further suggested that the abnormal shift of the Alaska gyre (Royer and Emery 1987) is the amplified version of the seasonal shift. However, the absence of the seasonal westward shift of the gyre in the seasonal baroclinic model as well as in the diagnostic model (Figure 2.2) suggests that the abnormal shift of the gyre is not due to the amplification of the seasonal phenomenon but due to the passage of the anticyclonic eddies originated from the Alaska Current region (Musgrave *et al.* 1990). Furthermore, a seasonal shift of the Alaska gyre is not likely to occur in nature considering that the estimate of the seasonal variations in the transport of the Alaska Stream is none to only 13 % at most (Reed *et al.* 1980; Royer 1981).

Reproduced with permission of the copyright owner. Further reproduction prohibited without permission.

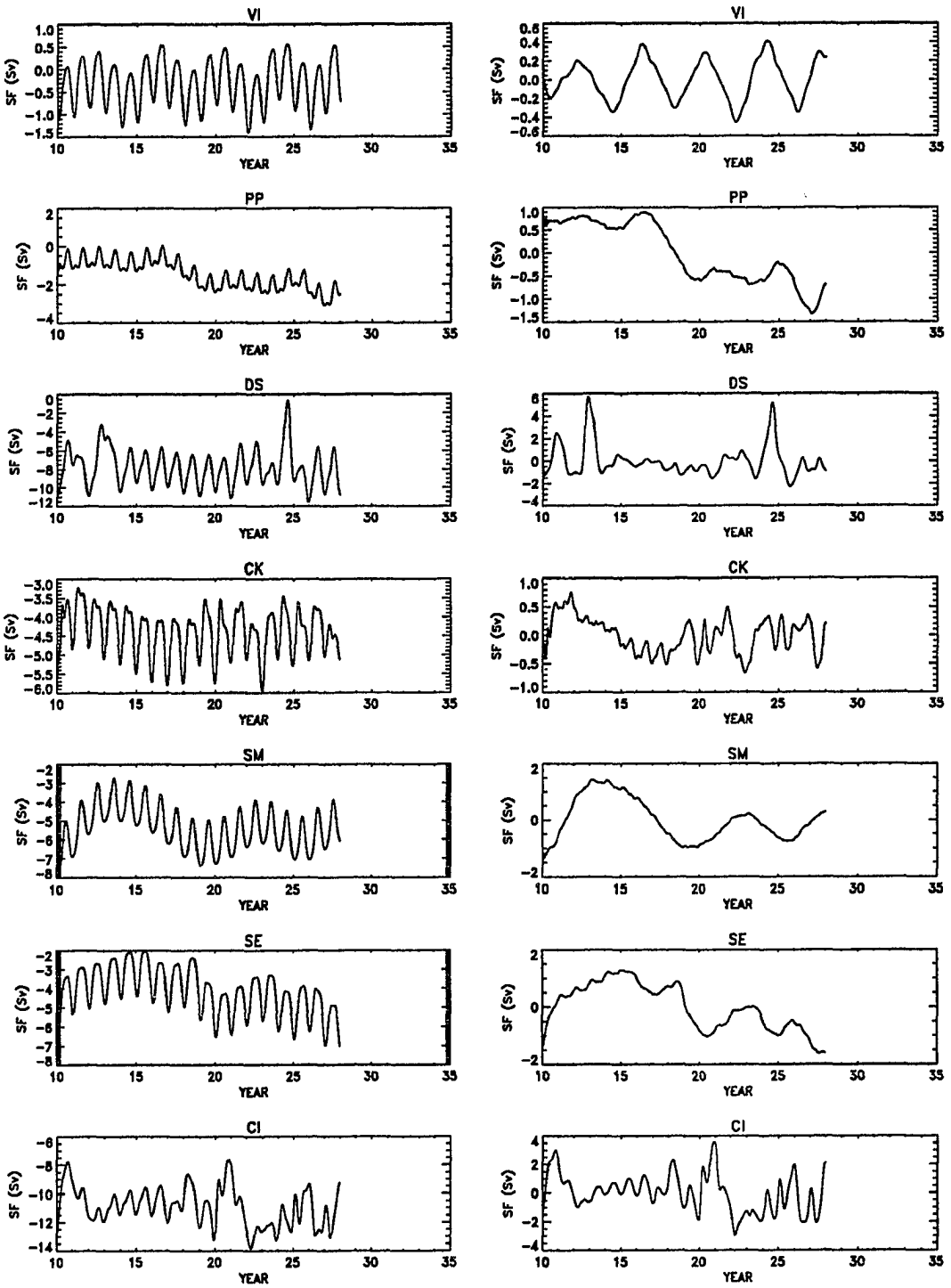

Figure 5.13 Time series of raw stream function (left) and FFT-filtered (right) at monitoring points.

Reproduced with permission of the copyright owner. Further reproduction prohibited without permission.

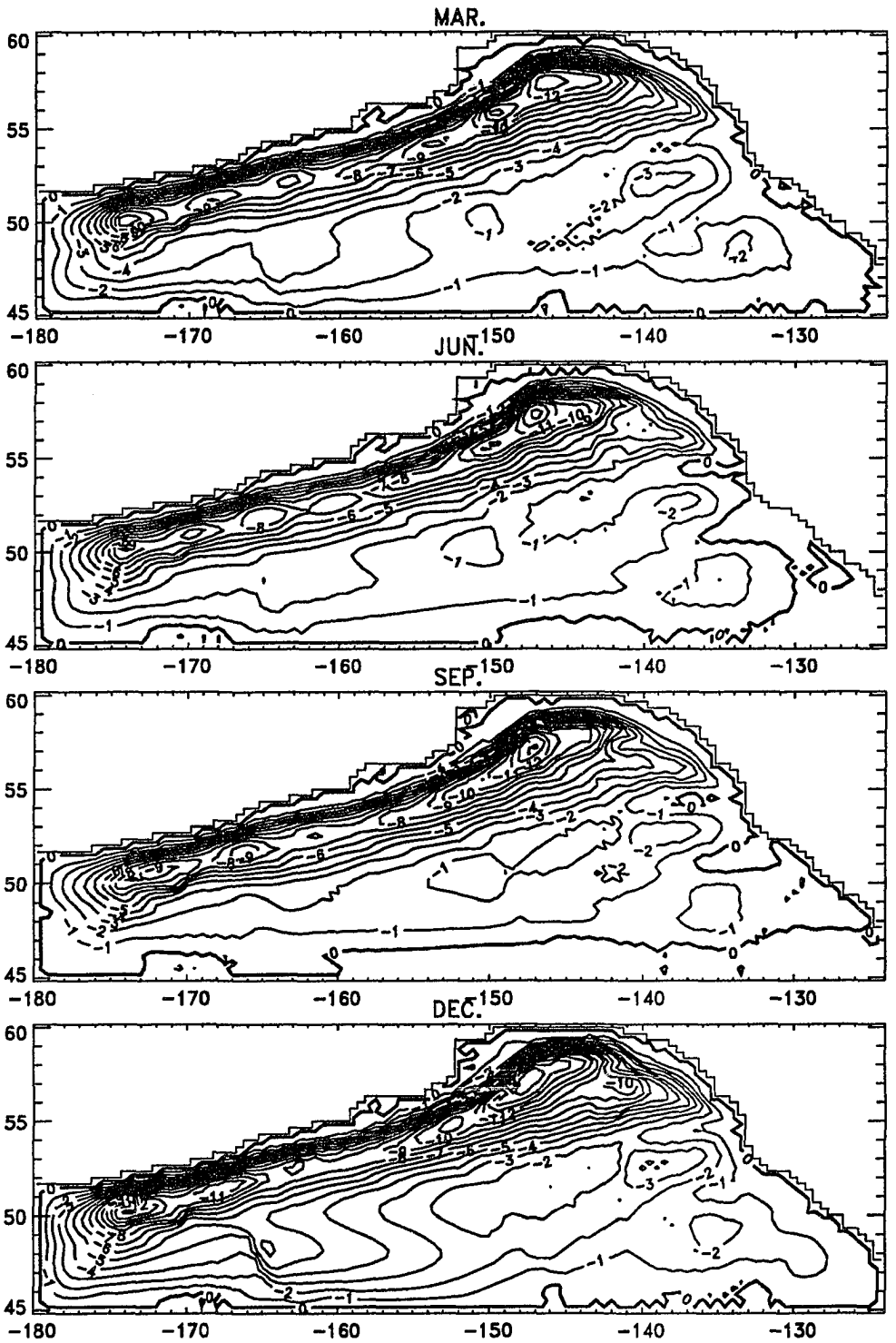

Figure 5.14 Contour plots of stream function in March, June, September, and December from year 18.

Reproduced with permission of the copyright owner. Further reproduction prohibited without permission.

Chapter 6 DISCUSSION AND CONCLUSIONS

In this thesis, a series of numerical experiments have been carried out to simulate the ocean circulation in the Gulf of Alaska. A number of barotropic and baroclinic models have been developed starting from simple ones and gradually adding new features to make them more and more realistic. A focus of this work is on the explanation of the seasonal variability of the Alaska Stream, mesoscale variability, and abnormal shift of the Alaska gyre. The experiments began with a diagnostic model. A yearly average and seasonal circulation have been produced from observed density field. The derived picture agrees well (especially in the surface layer) with observations and measurements. An interesting result of this diagnostic model is the existence of permanent eddies south of the Alaska Stream.

The second experiment is a seasonal barotropic model with bottom topography which is forced by the time-varying wind stress. The resulting circulation is surprisingly weak due to the scattering effect of the bottom topography. This model is helpful in understanding the seasonal response of the seasonal baroclinic model because there are similarities in the spatial patterns of the seasonal range between the seasonal barotropic model and the seasonal baroclinic model. It suggests that the seasonal response of the seasonal baroclinic model is mainly barotropic. Furthermore, the diagnostic model also shows a similar spatial pattern except for the noise due to the mismatch between the density field and the bottom topography. Therefore, it is certain that the seasonal variability in the Gulf of Alaska is mainly barotropic and there is little seasonal variability in the density field.

The first baroclinic computation was a three-layer, flat-bottom model, forced by wind stress only. In this experiment, first baroclinic Rossby waves were identified as being responsible for the spin-up which took a decade in the Gulf of Alaska. Eddies were excited in the flat-bottom model with 10 layers and in the model with bottom topography. In these models, thermohaline

Reproduced with permission of the copyright owner. Further reproduction prohibited without permission.

forcing was also included. Eddies are the major contributor to the mesoscale variabilities in the gulf and they were interpreted as Rossby waves. Barotropic and baroclinic Rossby waves are dominant in the flat-bottom case and topography case, respectively. There is also a shift in the observed period of eddies from 70–80 days in flat-bottom case to 3–4 years in topography case. The horizontal scale of the eddies also changes from about 250 km to 550–750 km. Although the eddy diffusivity of the topography case is twice larger than the value used in the flat-bottom case, it is not likely to be the major factor of the shift in the frequency of the dominant eddies because same values of horizontal eddy viscosity and bottom friction coefficient are used in both cases. Instead, it could be due to the stabilizing effect of bottom slope of the continental slope (Orlanski and Cox 1973).

Another possible explanation of this shift in dominant eddies comes from geostrophic turbulence theory. Böning (1989) compares two numerical experiments with and without bottom topography. The distribution of bottom topography in his experiment is random and represents small scale topographic irregularity in the open ocean. Böning (1989) finds that there is a shift of dominant mesoscale activities to low frequencies by the introduction of bottom topography and attributes this stabilization to the cessation of the barotropization (Rhines 1977; Treguier and Hua 1988) which precedes the radiation of energy by wave processes in a flat-bottom ocean. The tendency of the downward energy transfer to create vertically coherent structures by nonlinearity is effectively interrupted by the topographic scattering.

Satellite infrared images (not shown) sometimes show mesoscale eddies in the Alaska Stream. They appear as a series of crests and troughs along the Alaska Stream as in the flat-bottom case (lower panel of Figure 4.6). One big difference between eddies from the model and the satellite images is in the length scale. The length scale of eddies in the satellite images (only about 50–100 km from crest to crest) is smaller than that (200–250 km) in the flat-bottom case. Although a strict comparison is not possible between them without more information (for

Reproduced with permission of the copyright owner. Further reproduction prohibited without permission.

example, period or propagation speed) on the satellite imaged eddies, one possible cause for the discrepancy in the length scale is the model grid size (about 37 km) which is not capable of resolving motions smaller than about 74 km (2 Δx). A higher resolution model will be needed to clarify this point.

There exists also a series of cyclonic and anticyclonic eddies along the Alaska Stream in the topography case but their length scale is even larger (550–750 km) than those in the flat-bottom case. These eddies first appear in the Alaska Current region and propagate northwestward. The anticyclonic eddies that gain the strength around 57° N, 140° W are interpreted as the Sitka eddy (Tabata 1982) and appear every 3–4 years. They propagate westward at a speed about 0.6 *cm/sec* and cause meanders in the Alaska Stream near Kodiak Island as also identified by Musgrave *et al.* (1990). These anticyclonic eddies are also believed to cause the shifts of the Alaska Stream and the accompanying eastward currents observed at other locations (Favorite *et al.* 1976).

As a final experiment, seasonal variability is included in the forcing. It was found that bottom topography greatly affects the ocean's response to the seasonal forcing. The seasonal circulation response in the flat-bottom case directly responds to the change in the wind stress curl while the seasonal variation in the topography case is not as well pronounced. Seasonal transport variations occur through both the external and internal modes in the topography case while the external mode is the major contributor in the flat-bottom case. This difference determines the ocean response to the seasonal forcing because of the differences in the propagation speed and the spin-up time of these two modes. The dominance of the fast propagating barotropic mode (barotropic Rossby waves) accompanied by the absence of a scattering effect of bottom topography enables the flat-bottom ocean to achieve a large seasonal fluctuation. This is in contrast to the reduced role of the barotropic mode and the scattering by bottom topography which makes the seasonal fluctuations small in a ocean with topography.

Reproduced with permission of the copyright owner. Further reproduction prohibited without permission.

The non-topographic Sverdrup circulation is established in a flat-bottom ocean whether its stratification is barotropic or baroclinic. A major difference between the barotropic and baroclinic oceans is in the spin-up time for the establishment of the Sverdrup circulation. The barotropic Rossby waves which are solely responsible for the spin-up of the barotropic ocean propagate at a speed of on the order of 1 *m/sec* and the ocean reaches an equilibrium on the time scale of one month. On the other hand, first baroclinic Rossby waves are dominant in a baroclinic ocean and equilibrium is achieved only after their propagation to the western boundary, which takes a decade at a speed of on the order of 1 *cm/sec* at high latitudes.

When bottom topography is introduced into the model, the circulation differs significantly from the flat-bottom case. Bottom topography alters the circulation considerably in the barotropic ocean because the barotropic Rossby waves are now generated by $curl_z(\tau/H)$ where τ is the wind stress and H is the ocean depth (Anderson and Corry 1985b). So, the effect of bottom topography directly influences the barotropic ocean. In a baroclinic ocean, however, the effect of topography is alleviated by the baroclinicity. The ocean forced by a constant wind forcing achieves the non-topographic Sverdrup circulation after the propagation of the baroclinic Rossby waves that compensate the effect of topography.

The situation is similar in the case with time-dependent forcing, or more specifically, seasonal forcing as with the constant forcing. Fast barotropic Rossby waves easily catch up with the time changes in the forcing and are fully represented in the ocean circulation. On the other hand, the baroclinic Rossby waves propagate only a small distance before the forcing changes in time. Consequently, the compensation of the topography is not complete over the entire ocean but is limited only near their generation regions. Therefore, non-topographic Sverdrup circulation is not established. This was also the conclusion of Anderson and Corry (1985a) that the ocean response to the seasonal forcing is mainly barotropic at middle and high latitudes. Therefore, the response of the ocean with bottom topography to the seasonal forcing

Reproduced with permission of the copyright owner. Further reproduction prohibited without permission.

can be considered as the sum of barotropic response and the localized baroclinic response.

According to the diagnostic model, seasonal barotropic model and seasonal baroclinic model, the seasonal variation of the total transport in the Alaska Stream region is only 2 Sv. Since it is based on the stream function which represents the vertically integrated transport, an estimate of the seasonal variation in the upper 1500 *m* is also made and is about 1 Sv. This value can be compared to the quantitative estimate by Royer (1981) which is based on 21 geostrophic current observations relative to 1500 *db* between 148° W and 165° W. Royer (1981) estimated 13 % as the seasonal amplitude relative to the mean transport of 9.2 Sv. Using these values, one can estimate the lower limit of the seasonal range as 2.4 Sv assuming no contribution from the deep layers (note that the seasonal range is twice the amplitude). Therefore, the estimate of 1 Sv as the seasonal range in the upper 1500 *m* lies between the estimate 2.4 Sv of Royer (1981) and no seasonal variability of Reed *et al.* (1980).

The small seasonal variability in the transport, along with no appreciable seasonal variation in the circulation pattern, can be compared to the results of Cummins (1989) and Hsieh (1987). In Hsieh (1987), the seasonal fluctuation of the Alaska gyre looks more like those in a flat-bottom model and a use of small number of vertical levels causes this unrealistic circulation. This was pointed out by Cummins (1989). However, a seasonal east-west shift of the Alaska gyre is also observed in Cummins (1989) which is not seen in the diagnostic and seasonal baroclinic models of this thesis.

Many of my conclusions are similar to those derived by the quasi-geostrophic model of Cummins and Mysak (1988) and Cummins (1989): 1) topography shifts the dominant frequency of mesoscale eddies to lower frequencies, 2) the mesoscale eddies are caused by the baroclinic instability, and 3) topography also decreases the amplitude of the seasonal response. Differences from Cummins and Mysak (1988) and Cummins (1989) are noted in the characteristics of the dominant eddies both in the flat-bottom and topographic cases. A major difference is in the

Reproduced with permission of the copyright owner. Further reproduction prohibited without permission.

conclusion about the abnormal shift of the Alaska gyre based on the absence of the seasonal shift in the model results of this thesis. I agree with Musgrave *et al.* (1990) that the apparent shift of gyre is due to the passage of a mesoscale eddy and is not due to an amplification of the seasonal shift of the Alaska gyre observed in Cummins (1989). Possible causes of the seasonal shift of gyre found by Cummins (1989) are 1) the difference in the wind data and 2) the absence of thermohaline forcing in their model. Cummins (1989) reports that the seasonal shift of his model gyre is the result of variations in the integrated strength of the wind stress curl over the gulf. However, it is surprising that the Alaska gyre in Cummins (1989) shifts westward in July when the positive wind stress curl is still present near the coast of North America. Royer (1981) suggested that the freshwater flux from the land during oceanic summer, maximum in October (Royer 1982), can set up the pressure gradient that can enhance the wind-driven cyclonic gyre in the Gulf of Alaska. If this is true, it may partly explains why Cummins (1989) has a seasonal shift of the Alaska gyre because the thermohaline forcing is absent in his QG model. Consequently, the wind forcing dictates the seasonal variation in QG model of Cummins (1989).

For the density determination from the temperature and salinity, $\rho(s,t,0)$ was used instead of the in-situ density because dynamically important variable is the density difference rather than the density itself. The resulting circulation looks reasonable with one exception. The circulation is weak (less transport) compared to the circulation by the in-situ density. Considering that it is common to use one variable (temperature is used in Semtner and Mintz (1977) and potential density in Cox (1985)) for the equation of state in some models, the use of $\rho(s,t,0)$ is acceptable. The reason that the in-situ density is not used in this thesis was the numerical instability. The model could have been made stable with a higher friction coefficient although the mesoscale eddies then would not have been excited. An increase in the horizontal resolution is one solution for this problem.

The need of a large number of vertical levels for a proper resolution of topography makes

Reproduced with permission of the copyright owner. Further reproduction prohibited without permission.

the primitive equation model expensive in terms of computer and human resources. The required resources are also increased by the number of predictive variables involved (velocity, density, and stream function). However, the completeness of dynamics, i.e., no approximation other than the hydrostatic, Boussinesq, and rigid-lid approximations, makes the primitive equation model good for general modeling efforts. On the contrary, the quasi-geostrophic model should be understood within the limitations of the quasi-geostrophic approximations. For example, Böning (1989) notes a strong nonlinearity in his primitive equation model that cannot be handled by QG dynamics.

The eddies in the flat-bottom case are quite regular both in space and time in that they are more like waves. Whereas in the topography case, the anticyclonic eddy which was identified as the Sitka eddy looks like an isolated ring (or solitary Rossby wave) and keeps its identity for a long time (about 5–6 years) indicating an importance of the nonlinearity. Böning (1989) also finds that the vortices keep their identity for a much longer duration in the topography case than in the flat-bottom case where they are quickly destroyed by wave radiation. Another interesting fact about the Sitka eddy is its rotation. Although local bottom topography could select the anticyclonic eddies preferentially, there is also a possibility that it is due to the asymmetry between anticyclonic and cyclonic vortices. Cushman-Roisin and Tang (1990) find that anticyclonic eddies are more robust than cyclonic eddies when a generalized geostrophic equation (the amplitude of the perturbation is not restricted to be small as in QG equation and can be as large as the water depth) is used. Their single-eddy numerical experiments show that anticyclonic eddy keeps its identity for a while whereas cyclonic eddy breaks up quickly. This adds to the ability of the anticyclonic eddy to persist

This asymmetry, however, is not possible in QG dynamics because of the assumption of weak vertical displacements. Therefore, studies with nonlinearities included will be needed to investigate its importance in the Gulf of Alaska. A primitive equation model with a higher spatial

Reproduced with permission of the copyright owner. Further reproduction prohibited without permission.

resolution than used in this thesis would be helpful for this purpose. The increased resolution of the model through faster computers would reduce the problems which were encountered during this study. The attempt of this thesis to simulate the circulation in the Gulf of Alaska is extensive but not complete. The work load required to accomplish these goals has been enormous but worthwhile in helping to better understand this part of the ocean.

Reproduced with permission of the copyright owner. Further reproduction prohibited without permission.

Bibliography

Anderson, D.L.T., and R.A. Corry, 1985a: Ocean response to low frequency wind forcing with application to the seasonal variation in the Florida Straits-Gulf Stream transport. *Prog. Oceanog.*, **14**, 7-40.

_____, and _____, 1985b: Seasonal Transport Variations in the Florida Straits: A Model Study. *J. Phys. Oceanogr.*, **15**, 773-786.

_____, and A.E. Gill, 1975: Spin-up of a stratified ocean, with applications to upwelling. *Deep Sea Res.*, **22**, 583-596.

_____, and P.D. Killworth, 1977: Spin-up of a stratified ocean, with topography. *Deep Sea Res.*, **24**, 709-732.

Böning, C.W., 1989: Influences of a rough bottom topography on flow kinematics in an eddy-resolving circulation model. *J. Phys. Oceanogr.*, **19**, 77–97.

Bryan, K., 1969: A numerical method for the study of the ocean circulation. *J. Comput. Phys.*, 4, 347–376.

Bryan, K., and M.D. Cox, 1972: An approximate equation of state for numerical models of ocean circulation. *J. Phys. Oceanogr.*, **2**, 510–514.

Camerlengo, A.L. and J.J. O'Brien, 1985: Open boundary conditions in rotating fluids. *J. Comput. Physics*, **35**, 12–35.

Chapman, D.C., 1985: On the numerical treatment of cross-shelf open boundaries in a barotropic coastal ocean model. *J. Phys. Oceanogr.*, **15**, 1060–1075.

Charney, J.G., 1947: The dynamics of long waves in a baroclinic westerly current. *J. Meteor.*, 4, 135–163.

Cheney, W., and D. Kincaid, 1985: *Numerical mathematics and computing.* 2nd ed. Brooks/Cole Publishing Company.

Reproduced with permission of the copyright owner. Further reproduction prohibited without permission.

Cox, M.D., 1984: A primitive equation, 3-dimensional model of the ocean. GFDL Ocean Group Tech. Rep. No. 1.

_____, 1985: An eddy resolving numerical model of the ventilated thermocline. *J. Phys. Oceanogr.*, **15**, 1312–1324.

Cummins, P.F., 1989: A quasi-geostrophic circulation model of the Northeast Pacific. Part II: Effects of topography and seasonal forcing. *J. Phys. Oceanogr.*, **19**, 1649–1668.

_____, and L.A. Mysak, 1988: A quasi-geostrophic circulation model of the Northeast Pacific. Part I: A preliminary numerical experiment. *J. Phys. Oceanogr.*, **18**, 1261–1286.

Cushman-Roisin, B., and B. Tang, 1990: Geostrophic turbulence and emergence of eddies beyond the radius of deformation. *J. Phys. Oceanogr.*, **20**, 97–113.

Eady, E.T., 1949: Long waves and cyclone waves. *Tellus*, **1**, 33–52.

Favorite, F., A.J. Dodimead, and K. Nasu, 1976: Oceanography of the subarctic Pacific region, 1960–1971. *International North Pacific Fisheries Commission Bulletin*, **33**.

Fofonoff, N.P., 1962: Physical properties of sea water. *The Sea*, Vol. 1, New York, Interscience.

Friedrich, H. and S. Levitus, 1972: An approximation to the equation of state for sea water, suitable for numerical ocean models. *J. Phys. Oceanogr.*, **2**, 514–517.

Garratt, J.R., 1977: Review of drag coefficients over oceans and continents. *Mon. Wea. Rev.*, **105**, 915–929.

Greatbatch, R.J., and A. Goulding, 1989: Seasonal Variations in a Linear Barotropic Model of the North Pacific Driven by Hellerman and Rosenstein Wind Stress Field. *J. Geophy. Res.*, **94**, 12645-12665.

Gower, J.F.L., 1989: Geosat altimeter observations of the distribution and movement of sea-surface height anomalies in the north-east Pacific. In *Oceans 89. Navigation, Remote Sensing, Underwater Vehicles/Explotation*, **3**, 977–981.

Reproduced with permission of the copyright owner. Further reproduction prohibited without permission.

Han, Y.-J., 1975: Numerical simulation of mesoscale ocean eddies. Ph.D. thesis, UCLA.

Hart, J.E., 1979: Finite amplitude baroclinic instability. *Ann. Rev. Fluid Mech.*, **11**, 147–172.

Holland, W.R., 1973: Baroclinic and topographic influences on the transport in western boundary currents. *Geophy. Fluid Dyn..*, **4**, 187–210.

_____, 1975: Energetics of baroclinic oceans. *Numerical models of ocean circulation.*, National Academy of Sciences, 168–177.

_____, and A.D. Hirschman, 1972: A numerical calculation of the circulation in the North Atlantic ocean. *J. Phys. Oceanogr.*, **2**, 336–354.

Hsieh, W.W., 1987: A numerical study of the seasonal cycle and its perturbations in the northeast Pacific Ocean. *Atmos. Ocean*, **25**, 375–386.

Huang, J.C.K., 1978: Numerical simulation studies of oceanic anomalies in the North Pacific Basin: The ocean model and the long-term mean state. *J. Phys. Oceanogr.*, **8**, 755–778.

_____, 1979: Numerical simulation studies of oceanic anomalies in the North Pacific Basin. Part II: Seasonally varying motions and structures. *J. Phys. Oceanogr.*, **9**, 37–56.

Killworth, P.D., 1987: Topographic instabilities in level model OGCMs. Ocean Modelling (unpublished manuscript) No. 75, 9–12.

Kirwan, A.D., Jr., G.J. McNally, E. Reyna and W.J. Merrell, Jr., 1978: The near-surface circulation of the eastern North Pacific. *J. Phys. Oceanogr.*, **8**, 937–945.

Leblond, P.H., and L.A. Mysak, 1978: *Waves in the ocean.* Elsevier Scientific Publishing Company.

Levitus, S., 1982: Climatological atlas of the world ocean. NOAA Prof. Paper 13.

Lighthill, M.J., 1969: Dynamic Response of the Indian Ocean to Onset of the Southwest Monsoon. *Philosophical Transactions of the Royal Society of London*, **A270**, 371-390.

Reproduced with permission of the copyright owner. Further reproduction prohibited without permission.

Luick, J.L., T.C. Royer, and W.R. Johnson, 1987: Coastal atmospheric forcing in the northern Gulf of Alaska. *J. Geophy. Res..*, **92**, 3841–3848.

McWilliams, J.C., 1977: On a class of stable, slightly geostrophic mean gyres. *Dyn. Atmos. Oceans*, **2**, 19–28.

Musgrave. D.L., T.J. Weingartner, and T.C. Royer, 1990: Circulation and hydrography in the northwestern Gulf of Alaska. submitted to *Deep Sea Res.*

North, G.R., T.L. Bell, R.F. Callahan, and F.T. Moeng, 1982: Sampling errors in the estimation of empirical orthogonal functions. *Mon. Wea. Rev.*, **110**, 699–706.

Orlanski, I., and M.D. Cox, 1973: Baroclinic instability in ocean currents. *Geophys. Fluid. Dyn.*, **4**, 297–332.

Pedlosky, J., 1982: *Geophysical Fluid Dynamics.* Springer-Verlag.

Pond, S., and G.L. Pickard, 1983: *Introductory Dynamical Oceanography*. Pergamon Press.

Ramming, H.G., and Z. Kowalik, 1980: *Numerical Modelling of Marine Hydrodynamics.* Elsevier.

Reed, R.K., 1968: Transport of the Alaska Stream. *Nature*, **220**, 681–682.

_____, 1980: Direct measurement of recirculation in the Alaska Stream. *J. Phys. Oceanogr.*, **10**, 976–978.

_____, 1984: Flow of the Alaskan Stream and its variations. *Deep Sea Res.*, **31**, 369–386.

_____, R.D. Muench, and J.D. Schumacher, 1980: On baroclinic transport of the Alaskan Stream near Kodiak Island. *Deep Sea Res.*, **27A**, 509–523.

Reid, J.L., and R.S. Arthur, 1975: Interpretation of maps of geopotential anomaly for the deep Pacific ocean. *J. Mar. Res., Supplement*, **33**, 37–52.

_____, and A.W. Mantyla, 1976: The effect of geostrophic flow upon coastal sea elevations in the northern North Pacific ocean. *J. Geophy. Res.*, **81**, 3100–3110.

Reproduced with permission of the copyright owner. Further reproduction prohibited without permission.

Rhines, P.B., 1977: The dynamics of unsteady currents. *The Sea*, Vol. 6, Wiley Interscience, 189–318.

Robinson, A.R., 1983: Overview and summary of eddy science. *Eddies in Marine Science*, A.R. Robinson, Ed., Springer-Verlag, 3–15.

Roden, G.I., 1969: Winter circulation in the Gulf of Alaska. *J. Geophy. Res.*, 74, 4523–4534.

Royer, T.C., 1981: Baroclinic transport in the Gulf of Alaska. Part I. Seasonal variations of the Alaska Current. *J. Mar. Res.*, 39, 239–250.

_____, 1982: Coastal fresh water discharge in the northeast Pacific. *J. Geophy. Res.*, 87, 2017–2021.

_____, and W.J. Emery, 1987: Circulation in the Gulf of Alaska, 1981. *Deep Sea Res.*, 34, 1361–1377.

Sarmiento, J.L., and K. Bryan, 1982: An ocean transport model for the North Atlantic. *J. Geophy. Res.*, 87, 394–408.

Sarkisyan, A.S., 1966: *Theory and Computation of Ocean Currents*, Moscow, Gidrometeoizdat. (English translation IPST Press, Jerusalem 1969).

_____, and V.F. Ivanov, 1971: Joint effect of baroclinicity and bottom relief as an important factor in the dynamics of sea currents. *Ivz. Akad. Nauk SSSR, Fiz. Atmos. Okeana*, 7, 173 (Engl. transl., p. 116).

_____, and A.F. Pastukhov, 1970: The density field as the main indicator of steady sea currents. *Ivz. Akad. Nauk SSSR, Fiz. Atmos. Okeana*, 6, 64 (Engl. transl., p. 34).

Semtner, A.J., 1974: An oceanic general circulation model with bottom topography. Numerical Simulation of Weather and Climate, Tech. Rep. No. 9, Dept. Meteor. UCLA, 99p.

_____, and R.M. Chervin, 1988: A simulation of the global ocean circulation with resolved eddies. *J. Geophy. Res.*, 93, 15502–15522.

Reproduced with permission of the copyright owner. Further reproduction prohibited without permission.

_____, and Y. Mintz, 1977: Numerical simulations of the Gulf Stream and mid-ocean eddies. *J. Phys. Oceanogr.*, **7**, 208–230.

Shapiro, R., 1970: Smoothing, filtering, and boundary effects. *Rev. Geophys. Space Phys.*, **8**, 359–387.

Spall, M.A., and A.R. Robinson, 1990: Regional primitive equation studies of the Gulf Stream meander and ring formation region. *J. Phys. Oceanogr.*, **20**, 985–1016.

Stommel, H., and F. Schott, 1977: The beta spiral and the determination of the absolute velocity field from hydrographic station data. *Deep Sea Res.*, **24**, 325–329.

Tabata, S., 1982: The anticyclonic, baroclinic eddy off Sitka, Alaska, in the northeast Pacific Ocean. *J. Phys. Oceanogr.*, **12**, 1260–1282.

Thomson, R.E., 1972: On the Alaska Stream. *J. Phys. Oceanogr.*, **2**, 363–371.

Treguier, AM., and B.L. Hua, 1988: Influence of bottom topography on stratified quasi-geostrophic turbulence in the ocean. *Geophys. Astrophys. Fluid Dyn.*, **43**, 265–305.

Veronis, G., and H. Stommel, 1956: The action of variable wind stresses on a stratified ocean. *J. Mar. Res.*, **15**, 43-75.

Warren, B.A., and W.B. Owens, 1988: Deep currents in the central Subarctic Pacific Ocean. *J. Phys. Oceanogr.*, **18**, 529–551.

White, W.B., 1982: Travelling wavelike mesoscale perturbations in the North Pacific Current. *J. Phys. Oceanogr.*, **12**, 231–243.

_____, and S. Tabata, 1987: Interannual westward-propagating baroclinic long-wave activity on Line P in the eastern midlatitude North Pacific. *J. Phys. Oceanogr.*, **17**, 385–396.

Willebrand, J., 1978: Temporal and spatial scales of the wind field over North Pacific and North Atlantic. *J. Phys. Oceanogr.*, **8**, 1080–1094.

Reproduced with permission of the copyright owner. Further reproduction prohibited without permission.

Willmott, A.J., and L.A. Mysak, 1980: Atmospherically forced eddies in the Northeast Pacific. *J. Phys. Oceanogr.*, **10**, 1769–1791.

Wunsch, C., 1978: The North Atlantic general circulation west of 50° N determined by inverse methods. *Rev. Geophys. Space Phys..*, **16**, 583–620.

Reproduced with permission of the copyright owner. Further reproduction prohibited without permission.